PERSONALIZED DOSIMETRY PROTOCOL FOR THE OPTIMIZATION OF LUTETIUM-177 DOTATATE RADIONUCLIDE THERAPY

by

Wei Zhao

B.Eng., University of Science and Technology of China, 2014

A THESIS SUBMITTED IN PARTIAL FULFILLMENT OF

THE REQUIREMENTS FOR THE DEGREE OF

DOCTOR OF PHILOSOPHY

in

THE FACULTY OF GRADUATE AND POSTDOCTORAL STUDIES

(Physics)

THE UNIVERSITY OF BRITISH COLUMBIA

(Vancouver)

July 2019

The following individuals certify that they have read, and recommend to the Faculty of Graduate and Postdoctoral Studies for acceptance, the dissertation entitled:

Personalized Dosimetry Protocol for the Optimization of Lutetium-177 DOTATATE Radionuclide Therapy

submitted by Wei Zhao in partial fulfillment of the requirements for

the degree of Doctor of Philosophy

in Physics

Examining Committee:

Anna Celler, Radiology
Supervisor

François Bénard, Radiology
Supervisory Committee Member

Cheryl Duzenli, Department Head, Medical Physics, BC Cancer Agency
Supervisory Committee Member

Alex MacKay, Physics
University Examiner

Chris Orvig, Chemistry
University Examiner

Additional Supervisory Committee Members:

Stefan Reinsberg, Physics
Supervisory Committee Member

Supervisory Committee Member

Abstract

Targeted radionuclide therapy has been shown to be one of the most effective treatment options for metastatic neuroendocrine tumours (NETs). In particular, peptide receptor radionuclide therapy (PRRT) with Lutetium-177 (^{177}Lu) labeled DOTATATE results in significantly improved tumour control, while only low to moderate normal tissue toxicity. There is growing evidence that the efficacy of this treatment can be further improved by performing personalized administration of radiopharmaceutical. However, since the dosimetry for PRRT is usually considered challenging, traditionally NET patients are treated with same or very similar amounts of ^{177}Lu DOTATATE. The objective of this thesis was to propose a simple, yet accurate dosimetry protocol, which could be easily implemented in clinics for the optimization of radionuclide therapy. To achieve this aim, the following questions, related to the image-based dose calculation, were investigated:

The performance of the camera calibration method, using simple planar scans, was compared to that obtained from tomographic acquisitions. To assess the quantitative accuracy of commercial SPECT reconstruction software (Siemens Flash3D), a number of phantom experiments with different photon attenuation conditions were performed. The influence of camera dead-time correction on the estimated dose was investigated. The kidney doses obtained from four time-activity curve creation methods, obtained using three data points, were compared. In order to simplify the dosimetry, the accuracy of dose estimated based on two data points, or even potentially one data point, was evaluated.

Our results show that the gamma camera can be accurately calibrated with planar scan of a point-like source. When Siemens Flash3D reconstruction was used, the errors of ^{177}Lu activity quantification in objects with large volumes (>100mL) was about 5%. Dead-time correction was found to have no impact on the estimated dose. Kidney doses estimated based on single data point measured at 48-72 hours produced small errors (<10%) for the majority of patients, thus could be recommended for clinical use. This single data point method can also be applied to other organs/therapies, as long as the organs' bio-kinetics can be described by a monoexponential function and the statistical behavior of the population effective half-lives for these organs have been estimated.

Lay Summary

Recently cancer treatment with radiation emitting isotopes, also known as radionuclide therapy, has become increasingly popular. Particularly, the isotope lutetium-177 (^{177}Lu) has been reported to produce promising results in treating many types of cancers. The measurement of radiation dose absorbed by the patients is usually considered too tedious to be performed in routine clinical practice. As a result, every patient is injected with similar amount of ^{177}Lu. This leads to large inter-patient variability in therapy response. The goal of this thesis is to develop a practical and accurate radiation dose estimation method for personalized radionuclide therapy. The work presented in this thesis demonstrates the feasibility of performing radiation dose measurement in busy clinics, which is very important to understand and improve the radionuclide therapy.

Preface

A version of Chapter 3 has been published as a journal article: Wei Zhao, Pedro L. Esquinas, Xinchi Hou, Carlos F. Uribe, Marjorie Gonzalez, Jean-Mathieu Beauregard, Yuni K. Dewaraja, and Anna Celler, "Determination of gamma camera calibration factors for quantitation of therapeutic radioisotopes", EJNMMI Physics, 5.1 (2018): 8. I performed the phantom experiments, Monte Carlo simulations, data analysis and wrote the manuscript with the help of Dr. Anna Celler. The project was conducted under the guidance of Dr. Anna Celler. Dr. Pedro L. Esquinas helped with Monte Carlo simulations. All the co-authors assisted with the experimental data acquisitions and the manuscript revision. The preliminary results from this project were also submitted as an abstract, at the Annual Congress of the European Association of Nuclear Medicine (EANM) in October 2017, Austria, Vienna. The abstract was selected as the oral presentation at e-Poster Walk session.

The study presented in Chapter 4 was primarily designed and performed by me. Dr. Anna Celler helped with the design of the phantom experiments. Dr. Marjorie Gonzalez and Dr. Pedro L. Esquinas assissted with the phantom data acquisition. Dr. Jean-Mathieu Beauregard assisted with the patient data acquisition.

The material presented in Chapter 5 has been accepted for publication as part of the journal article: Xinchi Hou, Wei Zhao, Jean-Mathieu Beauregard, Anna Celler, "Personalized kidney dosimetry in ^{177}Lu-octreotate treatment of neuroendocrine tumours: A comparison of kidney dosimetry estimates based on a whole organ and small volume segmentations", Physics in Medicine and Biology. I was responsible for the data analysis of the whole kidney dose, involved

in the discussion and contributed to the manuscript writing. I was one of the two co-first authors in this paper. Dr. Xinchi Hou performed small volume dose calculation and wrote the manuscript. Dr. Jean-Mathieu Beauregard assisted with the patient data acquisition. Dr. Anna Celler supervised this project. All the co-authors were involved in the discussion and the manuscript revision.

The work presented in Chapter 6 has been accepted for publication as a journal article: Wei Zhao, Pedro L Esquinas, Andrea Frezza, Xinchi Hou, Jean-Mathieu Beauregard and Anna Celler, "Accuracy of kidney dosimetry performed using simplified time activity curve modelling methods: a ^{177}Lu-DOTATATE patient study", Physics in Medicine and Biology. I designed the study, analyzed the patient data and drafted the manuscript with the help of Dr. Anna Celler. Dr. Jean-Mathieu Beauregard and Andrea Frezza assisted with the patient data acquisition and transferring. All the co-authors helped with the manuscript revision.

The ^{177}Lu DOTATATE patient study presented in Chapter 5 and Chapter 6 is part of the collaboration with Nuclear Medicine department of CHU de Québec—Université Laval. Dr. Jean-Mathieu Beauregard was the principal investigator who conducted the clinical trial P-PRRT (registration number: NCT02754297). The Ethics Committee of CHU de Québec—Université Laval approved the patient scans. Informed consent was obtained from all the participants. The retrospective analysis of the patient SPECT/CT images acquired in this clinical trial was approved by UBC Office of Research Ethics, certificate number H08-01642.

Table of Contents

List of Tables

List of Figures

List of Abbreviations

2D	Two-dimensional
3D	Three-dimensional
AC	Attenuation correction
CB	Cold-background
CDR	Collimator detector response
CF	Calibration factor
CT	Computed Tomography
CV	Coefficient of variation
D0	Day 0
D1	Day 1
D3	Day 3
DOTATATE	[DOTA,Tyr3]-octreotate
DOTATOC	[DOTA0, Tyr3]-octreotide
FOV	Field of view
GATE	Geant4 applications for tomographic emission
HC	Hot-cylinder
HS	Hot-sources
IAT	Iterative adaptive thresholding
LSW	Lower scatter window
MELP	Medium energy low penetration collimator

MIRD	Medical Internal Radiation Dose
MIRG	Medical Imaging Research Group
MLEM	Maximum Likelihood Expectation Maximization
NET	Neuroendocrine tumour
NM	Nuclear medicine
NS	Narrow scatter window
OSEM	Ordered Subset Expectation Maximization
OW	Other window
PET	Positron Emission Tomography
PP	Primary photons
PRRT	Peptide receptor radionuclide therapy
PS	Point source
PVE	Partial volume effect
PW	Photopeak window
RC	Recovery coefficients
ROI	Region of interest
RR	Resolution recovery
SBR	Source to background ratio
SC	Scatter correction
SPECT	Single Photon Emission Computed Tomography
SSTR	Somatostatin receptors
TAC	Time activity curve

TEW	Triple energy window
TRT	Targeted radionuclide therapies,
USW	Upper scatter window
VOI	Volume of interest
WB	Warm-background
WS	Wide scatter window

Acknowledgements

After years of hard work, I finally completed the project and defended my doctoral dissertation. There are many people who generously contributed to the work presented in this dissertation. It is a great pleasure for me to say thanks to each one of you.

First of all, I would like to express my heartfelt thanks to my supervisor Dr. Anna Celler, for her inspired mentoring, insightful suggestions, great patience and constant support throughout my Ph.D. study at UBC. Thank you for believing in me and accepting me as your Ph.D. student. Thank you for your enthusiasm, ideas and contributions, which made my Ph.D. experience productive and enjoyable. The profound knowledge and research skills I learned from you will benefit me a lot in my future life and career.

I also would like to express sincere thanks to my committee member: Dr. Cheryl Duzenli, Dr. François Bénard and Dr. Stefan Reinsberg, for your time and helpful guidance. Thank you for the valuable discussions and positive feedback which definitely improved the quality of my research.

Dr. Jean-Mathieu Beauregard, Andrea Frezza and our collaborators in Nuclear Medicine department of CHU de Québec—Université Laval, thank you very much for providing us the ^{177}Lu DOTATATE patient data. Without your contributions, this dissertation would never be finished. Special thanks to Dr. Jean-Mathieu Beauregard for your time, discussions and good advice from a medical perspective.

My thanks also go to the Medical Imaging Research Group members: Pedro, Xinchi, Laurel, Cassandra, Hillgan and Carlos, for the help, stimulating discussions and great times we had. Thank you all for being not only my colleagues but also my friends. Thank you for making

our office a pleasant and welcoming workspace. Thank you to all the group members who contributed to the development of our in-house quantitative reconstruction algorithm. Without your work, I cannot finish my Ph.D. project.

I want to thank all the staffs in Nuclear Medicine department of Vancouver General Hospital. Thank you for being kind and helpful during the experiments. In particular, thank you Dr. Marjorie Gonzalez for always making the clinical camera accessible. Thank you for staying with us even at late nights for the experiments.

Thank you Dr. Curtis Caldwell and our collaborators in Toronto for providing us the dead-time planar imaging data presented in Chapter 5.

I greatly acknowledge the financial support received during my Ph.D. study, from University of British Columbia (UBC), Canadian Institutes of Health Research (CIHR) and Natural Sciences and Engineering Research Council of Canada (NSERC).

Thank you to all my teachers, classmates and friends who helped shape me into the person I am today. Special thanks to my physics and mathematics teachers in high school (junior and senior) and universities. Thank you for being my great mentors.

Last but not least, thank you to my beloved family in China. Thank you for your care throughout the years of my education. Special mention to my maternal grandparents. Thank you for your love and kindness, which makes my childhood full of happy and unforgettable memories. I am deeply thankful to my mom Xiuyun and my dad Wenxing, for your endless love, encouragement and sacrifices. Thank you for supporting me in all my pursuits. Thank you for your hard work and everything you offered to me. I would not have made it so far without you. Thank you my little brother Qi. You are smart and bring me so much joy. I am truly blessed to have you in my life.

To my mom, dad and little brother

Chapter 1: Statement of the research questions, aim and outline of the thesis

In recent years, targeted radionuclide therapy has gained a lot of attention in cancer research communities. Particularly, the peptide receptor radionuclide therapy (PRRT) using ^{177}Lu DOTATATE has been reported to produce encouraging results in the treatment of somatostatin receptor positive neuroendocrine tumours (NETs). Ideally, the PRRT treatment protocol should be customized for every patient like it is done in external beam radiation therapy, where for each patient a personalized treatment plan, based on individualized dose estimation, is generated. Unfortunately, this is not being routinely done in ^{177}Lu DOTATATE PRRT. Currently, the treatment protocol developed by the Erasmus Medical Center is widely applied in clinical practice. This protocol uses a 'one-size-fits-all' approach, in which the total activity of 27.8 to 29.6 GBq ^{177}Lu DOTATATE is administered, usually in four cycles, with intervals of 6 to 10 weeks [1]. However, the activity injected in this scheme was determined based on a planar dosimetry study of only 6 patients [2]. Subsequently, almost all NET patients are treated in a similar way: an empirical, fixed amount of ^{177}Lu DOTATATE is injected and no patient dosimetry is performed during the course of PRRT.

Examples of therapies performed using this approach include Wehrmann et al. from the Bad Berka group [3]. They studied 61 patients with metastasized NETs who received one to four cycles of ^{177}Lu DOTATATE (mean injected activity per cycle 5,534 MBq, range 2,500–7,400 MBq). The amount of administered activity was based on the general status of the patient (e.g. kidney function, previous treatment responses and so on). Similarly, Ezziddin et al. used four

cycles of ^{177}Lu DOTATATE (mean activity per cycle 8,000 MBq) in the PRRT of 68 patients with pancreatic NETs [4]. The rationale for the choice of the activity injected to each patient was not mentioned.

This standard ‘same-dose-fits-all’ approach is easy to implement and should result in relatively low adverse effects in the whole population treated. However, from the perspective of an individual patient, the ‘same-dose-fits-all’ protocol seems inefficient, sometimes harmful. High inter-patient variability in absorbed radiation doses to both the tumours and organs at risk per unit administered activity was reported [3,5–7]. Indeed, doses delivered to the kidneys per unit injected activity can differ by up to a factor of 7 and doses to the tumours by a factor of 10 [7,8]. This fact stimulates the need for a personalized therapy planning, rather than implementing a fixed therapeutic regimen approach. That is, tailoring the administered activity in the later cycles, based on the dose estimates obtained from earlier cycle(s), to maximize the tumour radiation dose while keeping the organs at risk dose below certain safety threshold.

The estimation of radiation dose in ^{177}Lu radionuclide therapy should be based on multiple post administration tomographic acquisitions using Single Photon Emission Computed Tomography (SPECT), which aim to accurately determine: 1) the radiopharmaceutical concentration in the tumours and other organs, especially the critical organs (bio-distribution), 2) the radiopharmaceutical bio-kinetics in each of these regions. The main motivation of this thesis was to simplify these two steps so that they could be performed using clinically available resources and conditions.

1.1 Aim

The aim of the thesis was to develop an accurate, SPECT image-based dosimetry protocol to be implemented for the optimization of the clinical radionuclide therapy. In order to accomplish this goal, three specific objectives have been identified:

1) Development of a simple yet accurate camera calibration method, which is necessary to translate quantitative measurements of radiotracer uptake (based on SPECT imaging) into absolute activity values (i.e. in the unit of Bq or MBq).
2) Evaluation of the quantitative accuracy of the commercial reconstructions (such as the Flash3D offered in Siemens SPECT/CT camera). Image reconstruction algorithms play a central role in quantitative measurements of ^{177}Lu DOTATATE. As the patient scans are reconstructed using camera manufacture's software, the quantitative performance of this software needs to be assessed.
3) Optimization of image-based dose calculation protocol for the critical organs, such as kidney. The number of SPECT/CT scans needs to be minimized and the timing of each acquisition needs to be carefully selected, while keeping the estimated radiotracer bio-kinetics within acceptable accuracy. This is to make the radiopharmaceutical bio-kinetics measurement less resource demanding.

In addition, other factors that could influence the radiation dose estimate for patients undergoing ^{177}Lu DOTATATE radionuclide therapy, such as the camera dead-time compensation and the kidney segmentation method, are investigated.

1.2 Outline

The thesis is organized as follows.

In Chapter 2, the NET is introduced, and its currently available diagnostic and therapeutic options are presented. The physics related topics, such as the quantitative SPECT imaging and image-based dosimetry, are also discussed. The content of these two sections represents the background knowledge, necessary to understand the dosimetry for NET patients undergoing ^{177}Lu DOTATATE radionuclide therapy.

Chapter 3 investigates the camera calibration for quantitative SPECT imaging of the radioisotopes that are widely used for therapy. Based on the experimental phantom data, the calibration factors obtained from different methods are compared. In parallel, Monte Carlo simulations (GATE) with configurations similar to those used in experiments are performed to explain the differences observed in calibration factors determined by different methods. Lastly, a practical calibration method is proposed.

The quantitative accuracy of ^{177}Lu SPECT images reconstructed with the clinical software is evaluated in Chapter 4. The phantom experiments with different attenuation and scatter configurations are performed. The acquired projection data is reconstruction with both the clinical software and the in-house developed software. The activity recovery coefficients calculated from both reconstructed images are compared.

Chapter 5 focuses on accurate kidney (the critical organ) dosimetry using multiple SPECT images of NET patients undergoing ^{177}Lu DOTATATE radionuclide therapy. The results of Chapter 3 and Chapter 4 are applied to achieve quantitative measurements of organ activities at several time points. In addition, other factors that could influence the organ activity

quantification, such as the camera dead-time correction and the organ segmentation, are discussed. The values of time integrated activity, determined based on different time-activity curve creation methods, are compared. The organ doses are evaluated.

In Chapter 6, to make image-based dosimetry less demanding, the performance of simplified dosimetry methods that require a smaller number of SPECT/CT acquisitions is investigated. Using 39 patients' datasets, the accuracy of the critical organ doses obtained from these simplified methods is assessed, using dosimetry results obtained in Chapter 5 as the reference.

Finally, Chapter 7 summarizes the main thesis conclusions and provides the suggestions for the directions of future work that might further benefit the patients undergoing radionuclide therapy.

Chapter 2: Introduction

2.1 Clinical background: Neuroendocrine tumours

Neuroendocrine tumours (NETs) are a group of heterogeneous cancer cells that arise from the endocrine and nervous systems. They are rare (incidence: 3-8 per 100,000), slow growing tumours that usually originate from the gastrointestinal tract, but can also stem from other organs including lungs and pancreas [9–13]. Recent studies show that the incidence of NETs has increased significantly over the last few decades, potentially due to the improvement of diagnosis [11,12,14–16]. Because of the indolent nature and heterogeneity of clinical symptoms, NETs remain a poorly understood disease and a unified pathologic classification system is still missing [17]. As a result, patients usually experience delayed diagnosis, with a median of 36 months [18,19]. In contrast to the increased incidence, the 5-year overall survival for NET patients remains unchanged over the past few decades [13,15]. Despite undergoing treatments, NET severely influences patients' quality of life. Karppinen et al. conducted a questionnaire survey of 134 patients with small intestine NETs and severely impaired health-related quality of life was reported, such as diarrhea, depression etc [20]. Based on these studies, NET deserves more attention in cancer research in order to improve the management and survival of patients.

2.1.1 NETs diagnosis

Proper diagnosis and staging of NETs requires assessment of clinical symptoms, histological review, identification of the biomarkers and knowledge of the disease extent [9,15,19,21,22].

2.1.1.1 Clinical symptoms

The clinical presentation of NETs varies with the location of primary tumour and the type of the secreted neuropeptide hormone [15]. Most gastrointestinal tract/pancreas originated NETs are presented as non-functional tumours, i.e. the secreted peptides and neuroamines do not cause any clinical symptoms, thus are usually diagnosed by accident [9,15,22]. Typical syndrome among the patients with functional NETs are cutaneous flushing and gut hypermotility with diarrhea, occurring in a rate up to 75% of the cases [19,23]. For patients with non-functional NETs, symptoms are usually abdominal pain, anemia or nutritional deficiencies, all of which can be caused by both local tumours and hepatic metastases [21]. A comprehensive functional survey should be included for all patients during the initial diagnosis and the entire disease course, in order to interpret clinical symptoms potentially related to secretory.

2.1.1.2 Histological review

Histology evaluation plays a core role in the diagnosis and staging of NETs originated from all sites [9,24]. Core biopsies, usually through endoscopic procedures or surgery, should be performed whenever possible in order to optimize available tissue and obtain related histological information [9,21,22]. As the histological information related to tumour diagnosis may change

during the course of the disease, multiple biopsies of both primary tumours and metastases are recommended [22].

2.1.1.3 Biomarkers

Biomarkers, which can be found in both body fluids and tumour tissues, can provide clinically useful information for the diagnosis, prognosis as well as the prediction of tumour response and recurrence [11,15,25]. Some biomarkers are common to all types of NETs while others correspond to specific subtype of NETs [11,15,26,27]. Currently chromogranin A (CgA) is one of the most widely used general biomarkers thanks to its high sensitivity and specificity for the detection of many types of NETs [28–30]. The proliferation marker KI-67 is also used to determine NET grade and prognosis. New biomarkers such as blood tumour transcripts are reported to have superior results compared with CgA, thus are likely to play a role in clinics [31–33].

2.1.1.4 Disease extent

The knowledge of NETs extent is also needed as the management options differ by the locations of primary tumours and metastases. Conventional anatomical imaging modalities, such as computed tomography (CT) , magnetic resonance imaging (MRI) and transabdominal/endoscopic ultrasound, are widely used to evaluate the locations of NETs and assess the treatment response [34–36]. In order to achieve high detection rate, the imaging protocol usually needs to be tailored based on the specific situation and the type of NETs [37,38]. For example, multiphase imaging is required for the successful imaging of NET with CT and the timing of each phase should be properly adjusted [39–41].

Somatostatin is a peptide hormone that is widely distributed in the human central nervous system and the peripheral tissues. It affects neurotransmission and cell proliferation, and inhibits release of many secondary hormones including growth hormone, thyroid-stimulating hormone etc [42]. Since most NETs overexpress all five somatostatin receptors (SSTR) [43], particularly the subtype-2 SSTR [37,44,45], nuclear medicine imaging with radioisotope labeled somatostatin analogues plays an important role in the staging and localization of NETs. Compared with anatomical imaging modalities, functional images can provide additional biological and prognostic information. Somatostatin receptor scintigraphy and single photon emission computed tomography (SPECT) with ^{111}In-DTPA-Octreotide have been used for the diagnosis and management of patients with NETs [24,46]. Meanwhile other ^{99m}Tc labeled SSTR agents, such as ^{99m}Tc-HYNIC-TOC/TATE, are also used in somatostatin receptor scintigraphy. Compared with ^{111}In labelled octreotide, they are less expensive, have better availability while maintaining comparable sensitivities [37,47]. SSTR positron emission tomography (PET) with ^{68}Ga labelled somatostatin analogues has also been proposed for NETs imaging. Benefiting the high spatial resolution, high tumour detection sensitivity and the absolute tracer quantification ability (based on standard uptake value) of PET machine, it has become preferred imaging modality for the initial diagnosis and localization of NETs [48–51]. Moreover, high quality images can be acquired within one hour after ^{68}Ga somatostatin analogues injection and the effective radiation dose is less than half of that observed in ^{111}In-DTPA-Octreotide [52]. Three ^{68}Ga labelled tracers, namely DOTA-TATE, DOTA-TOC and DOTA-NOC, have been investigated and they are usually considered equally efficient [37].

Due to the heterogeneity of NETs, no imaging technique is 100% sensitive. Usually the combination of multiple imaging modalities might be needed in order to get accurate knowledge of the disease extent [15,37].

2.1.2 NETs treatment

Ideally, the aim of the therapy for NETs is to cure the disease but it can also be useful to decrease the symptoms for some cases. Individualized treatment planning should be considered in order to produce optimal response [15,22]. Recognized as a cancer with relatively long overall survival, management of the NETs usually needs multiple sequential therapies although the best sequence for each particular patient might be hard to define. Currently, many general guidelines for NETs management have been published but there is no well-established metric to predict the NETs response for certain types of therapy [24,53,54].

2.1.2.1 Surgery, liver guided therapies, somatostatin analogues, biotherapy and chemotherapy

Surgery remains the main curative option for patients with localized disease and should be considered for the cases where it is technically feasible [55–58]. Resection of distant metastases is also recommended as it may be helpful to control the symptoms and offer survival benefit [59–61]. The role of surgery for the patients who have an unresectable metastatic disease is unclear and randomised trials with large sample sizes are needed [62]. Since the most common location of NET metastases is in the liver [63], liver guided therapies have been proposed such as hepatic arterial embolization and ^{90}Y microspheres radioembolization [64–67]. Somatostatin analogues (for example the octreotide) have been used to reduce hormonal syndromes, inhibit

proliferation of NETs and prolong the time to progression, but rarely resulting in an objective tumour response [68–70]. Biotherapy with interferon alfa has been reported but in this case the objective tumour response is generally low, within 4% to 10% [71]. Chemotherapy has also been applied for patients with unresectable NETs but its efficacy depends on the primary tumour location and the tumour grade [1,57,71].

2.1.2.2 Peptide receptor radionuclide therapy

For many years, peptide receptor radionuclide therapy (PRRT) has been used to treat patients with inoperable NETs. Radiolabelled somatostatin analogues, which have high binding affinity to SSTR expressed on most NETs, are injected to cause radiation induced tumour cell death in PRRT. Usually a ^{68}Ga PET/CT scan is performed to evaluate patient's eligibility for PRRT. Different radioisotope labelled somatostatin analogues have been proposed over the past few decades. The application of PRRT in the management of advanced NETs began with the usage of high dose ^{111}In-DTPA-Octreotide, which was initially introduced as a diagnostic agent. However, the results from many clinical studies using this therapy strategy showed that the number of patients with complete or partial response was low [72,73], probably because ^{111}In is not a beta emitter and only Auger and conversion electrons are available to deliver dose.

In the following years, the introduction of high binding affinity somatostatin analogues (octreotide or octreotate) and stable chelators such as DOTA enabled the stable labelling of high energy beta emitter ^{90}Y and medium energy beta emitter ^{177}Lu. As these radioisotopes provide more electrons for dose delivery to the tumour, latest generation of PRRT for the treatment of SSTR positive NETs employs either ^{90}Y-[DOTA0, Tyr3]-octreotide (DOTATOC) or ^{177}Lu-[DOTA,Tyr3]-octreotate (DOTATATE). Many phase 1 or 2 clinical studies have been

performed, with more encouraging results reported when compared with historical treatment data [74–79]. Particularly, PRRT with ^{177}Lu DOTATATE produced objective tumour response up to 60.3% [4]. A 40-72 months' survival benefit and significantly improved quality of life have been reported. In addition, PRRT with ^{177}Lu DOTATATE was well tolerated and only low to moderate toxicity was found in most individuals [80,81]. A recently published systematic literature review shows that the bone marrow toxicity is rare (1.4%) among the PRRT patients treated with ^{177}Lu DOTATATE over the past decade [82]. The results of the first randomized, controlled phase 3 trial of ^{177}Lu DOTATATE therapy for patients with advanced midgut NETs (NETTER-1) have been reported [83]. Compared with high dose octreotide long-acting repeatable (LAR), ^{177}Lu DOTATATE PRRT results in markedly higher rate of progression free survival at month 20 (65.2% vs 10.8% in the control group) and significantly higher tumour response rate (18% vs 3% in the control group). Based on these studies, ^{177}Lu DOTATATE PRRT, which is the focus of this thesis, has been recognized as one of the most promising treatment options for NET patients [84].

2.2 Physics background: Nuclear medicine

Nuclear medicine (NM) is a medical discipline involving the application of unsealed radioactive compounds (radiopharmaceuticals or radiotracers) in the diagnosis and/or treatment of diseases. Although NM procedures are usually performed for diagnosis purpose, the NM

procedures aimed at treatment of disease (also known as radionuclide therapy) have become more and more popular over the past few decades [85–89].

2.2.1 NM application in diagnosis and therapy

In a diagnostic NM study, radioisotopes, which emit γ photons or positrons are used to provide functional information about the disease. The radiopharmaceuticals are usually administered by intravenous injection or swallowing. These γ emitting radioisotopes are selected so that large number of their emissions can exit the patient body without interacting (through scatter or attenuation). Scintillation camera detects photons coming from the patient at one or many angular views (projections). The acquired data are processed to produce the distribution of the radioisotope (thus the diagnostic radiotracer) in either two-dimensional (2D) image (whole body planar study, only one view) or three-dimensional (3D) image (tomographic study, through image reconstruction from multiple views). There are two types of NM imaging devices. A single photon emission computed tomography (SPECT) camera detects photons over a wide energy range, therefore can be used to image many γ emitting radiotracers. Whereas the positron emission tomography (PET) camera is designed to detect the coincidence of photons that comes from the positron annihilation, thus is specifically used to image the positron emitting radiotracers. Malfunction of the organ is usually indicated by an abnormal pattern of radiotracer uptake (cold or hot spot) within that organ. For some disease, dynamic NM study could be useful where a series of images are acquired over a period of time. ^{99m}Tc is the most commonly used γ emitting isotope in NM [90], with a wide range of applications such as the diagnosis of coronary artery disease [91] and bone metastases [92]. ^{18}F is the most popular positron emitting isotope in NM and has been extensively used to diagnose various types of cancer and to assess their

recurrence [93,94]. Other isotopes used in NM diagnostic studies are: ^{123}I [95], ^{201}Tl [96],^{111}In [97], ^{67}Ga [98] and ^{68}Ga [99]. These isotopes usually have relatively short half-life and the typical amount of activity used in diagnostic procedures is small. Therefore, the radiation dose introduced by NM diagnostic imaging is considered medically inconsequential. NM imaging has been recognized as a powerful diagnostic tool due to its non-invasive nature and the ability of providing useful functional information underlying the disease.

While the NM scans are mostly performed for the diagnosis of disease, the use of radionuclides in therapy is growing rapidly, especially for the treatments of cancers with metastatic disease [100,101]. Radiopharmaceuticals suited for therapeutic purpose are composed of radioisotope labelled molecules that have high tumour binding affinity. Many different biological agents have been developed as the delivery vehicles, such as antibodies and peptides. Once administered to the patient, these radiotracers will mainly accumulate in the locations of the malignant cancer cell and its metastases. Unlike those used for NM diagnostic studies, the radioactive isotopes used for therapy are either β or α emitters. Thanks to the short tissue range (~10mm or less) of the emitted particles, radiopharmaceuticals labelled with these isotopes are able to deliver radiation dose locally to the targeted tumour locations, while sparing the surrounding healthy organs. Since many of the therapeutic isotopes also have γ or positron emissions, SPECT and PET imaging techniques can be helpful to monitor the delivery of the radiopharmaceuticals. Some examples of the isotopes used for radionuclide therapies are: ^{90}Y [102], ^{131}I [103], ^{177}Lu [104,105] and ^{223}Ra [106,107]. They are widely used for the treatment of many different types of cancers, such as liver metastases, thyroid cancer, NETs and metastatic prostate cancer. The therapeutic radiotracers are usually labelled with long-lived (few days' half-life) radioisotopes in order to have sufficient time for dose delivery. The selection of the

appropriate radiopharmaceutical for a particular patient not only depends on the type of the cancer and the characteristics of its biology, but also on its morphology. For example, bulky liver tumours are more likely to be treated with high energy β emitter ^{90}Y while for spotty, small bone metastatic disease α emitter ^{233}Ra tends to be more effective.

Personalized medicine has been shown to provide many benefits, thus is also desirable in NM therapeutic procedures [108,109]. In targeted radionuclide therapy, personalized medicine can be achieved by coupling the diagnostic imaging and therapy with the same biological molecules but labelled with different radionuclides [110]. The low dose diagnostic imaging, which employs a tracer labeled with γ emitting radionuclide, is performed to determine the patient's eligibility for therapy. The subsequent therapy is performed with the radiopharmaceuticals that employ the same biologically active agents as those used in the diagnostic radiotracer, but this time labeled with therapy isotopes. Same or at least very similar bio-distribution of tracer uptake is expected in both the diagnostic scan and the therapy course. Therefore, the diagnostic images are also helpful in predicting the treatment response and assessing the normal tissue toxicity. The idea of combing diagnosis and therapy is known as 'theranostics'. Many theranostics pairs have been developed in NM radionuclide therapy, such as ^{68}Ga-^{177}Lu DOTATATE [111] and ^{124}I-^{131}I Radioiodine [112].

2.2.2 Principles of quantitative SPECT imaging

Nowadays quantitative tomographic imaging plays an important role in many NM diagnostic and therapeutic applications [113–115]. Especially for radionuclide therapy, the estimation of radiation dose to critical organ/tumour is needed to assess the benefit of the treatment and the risk of normal tissue [116,117]. As discussed in Chapter 1, quantitative

information about radiotracer uptake bio-distribution at different time points, which can only be obtained from quantitative tomographic imaging studies, is required to estimate the radiation dose to volumes of interest. However, quantitative measurement of radiotracer within human body is not a trivial task as the quality of the acquired images is degraded by many factors, which can come from both the imaging system and the physical interactions of emitted γ photons. In order to address the challenges that involved in the optimization of radionuclide therapy, the principles of quantitative SPECT studies as well as the fundamentals of image-based dosimetry are described. Finally, lutetium-177, a promising radionuclide that has been widely applied in NM therapeutic procedures, is introduced.

2.2.2.1 Requirements for quantitative SPECT imaging studies

There are multiple factors that can affect the quantitative performance of SPECT. Due to the complexity of implementing corrections for image degrading factors, traditionally SPECT has been considered as a non-quantitative modality and the images were usually visually interpreted for diagnostic purposes only. In the past few decades, lots of effort has been made to produce quantitative data using SPECT imaging technique. Particularly, with the widespread installation of dual-modality SPECT/CT system, quantitative SPECT imaging became available in clinics [118]. In general, the requirements for quantitative SPECT imaging studies are:

1) The reconstructed images are linear, 3D representations of radioactive tracer concentration distribution in the camera field of view (FOV).

2) The imaging system must have the ability to compensate for the loss of the detected signal due to photon attenuation, and to correct for contamination from the scattered photons.
3) The calibration factor of the system, which translates the reconstructed counts into absolute activity values, has to be determined.
4) The imaging system must account for the potential counts loss due to camera dead-time.

The requirements mentioned above should allow users to obtain SPECT images that can provide quantitative measurement of the total activity in the camera FOV. However, in order to estimate the tumour/organ dose, there are additional requirements related to the activity quantification in the volume of interest (VOI): The collimator detector response (CDR) of the imaging system should be modeled as the partial volume effect (PVE) may significantly influence segmentation results.

The remaining part of this section describes all the steps and corrections, which are included in a typical quantitative SPECT imaging study.

2.2.2.2 The image reconstruction algorithm

In order to get 3D estimation of radiotracer distribution, the SPECT camera heads rotate around the patient body so that projection images are acquired at different angular positions. Subsequently, the acquired projection data is reconstructed as 3D images, mainly by either analytical approach or iterative method [119]. The analytical reconstruction methods are simple and fast, but rely on the assumption that no image degrading factors exist during the data acquisition process (which is never true in practice). Moreover, the reconstructed images usually

suffer from streak artifacts around the hot regions [120] and a noise enhancement effect [121]. The iterative approaches use system matrix (see below) to accurately model the image acquisition process, thus lead to significant improvement in both image quality and quantitative accuracy as compared with the analytical methods. The main drawback of iterative reconstructions is their relatively long computation time. However, with the increase of computer processor speed and the algorithm acceleration techniques, the iterative reconstruction can be performed within clinically acceptable time. Therefore, it has been recognized as the standard reconstruction algorithm in quantitative SPECT imaging studies.

The most commonly used iterative reconstruction method in quantitative SPECT imaging is the Maximum Likelihood Expectation Maximization algorithm (MLEM) [122] and its accelerated version Ordered Subset Expectation Maximization algorithm (OSEM) [123]. Some of the examples of the commercial software packages are *Evolution for Bone* from GE Healthcare, *Astonish* form Philips and *Flash3D* from Siemens [124,125]. These advanced SPECT/CT imaging systems, as well as the commercial data processing software, form the basics of performing quantitative imaging studies in clinical environment.

Benefiting from the assumption that the raw SPECT projections are subject to Poisson noise, these reconstruction algorithms are able to produce images with better noise properties compared to the analytical methods. This is particularly important for the acquisitions with low photon statistics. Additionally, some prior constraints can be included in these iterative methods to restrict reconstructed images to acceptable solutions. For example, all the voxel values in reconstructed images are non-negative, which is reasonable as they should represent the radioactivity distribution.

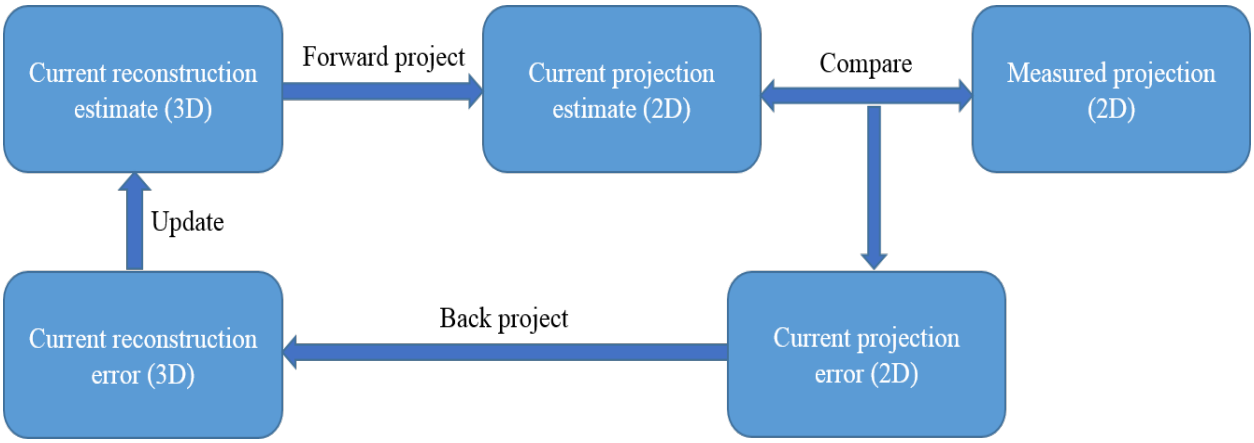

Figure 2.1 Flow chart showing the structure of the iterative MLEM algorithm (usually starts with a uniform activity distribution estimate). The current reconstruction estimate is forward projected to obtain the current projection estimate. By comparing the current projection estimate and the measured projection, the projection error is calculated. Then this projection error is back projected to get the reconstruction error, which is subsequently used to update the current reconstruction estimate. This procedure is repeated iteratively until the stopping condition is met, such as the iteration number is reached.

The structure of the MLEM algorithm is presented in Figure 2.1. Unlike the analytical reconstruction, the MLEM reconstruction aims to find the radioactivity distribution that maximizes the likelihood of producing measured projection images. There are two main processes involved in achieving this goal. Beginning with an initial estimation of radioactivity distribution (usually a uniform image), the forward projection and the back projection processes are repeated iteratively until the desired reconstructions are produced. This iterative MLEM algorithm can be described by the following equation:

$$X_j^{l+1} = \frac{X_j^l}{\sum_i C_{ij}} \sum_i C_{ij} \frac{P_i}{\sum_k C_{ik} X_k^l} \tag{2.1}$$

The meaning of the variables in this equation are:

- X_j^l – the *j* th voxel value of 3D estimation of the reconstructed image at iteration *l;*
- P_i – the *i* th pixel value of the measured projection image;
- C_{ij} – the *i,j* element of the system matrix, which represents the probability that photon emitted from image voxel *j* is recorded in the projection pixel *i*. The image degrading factors can be built into the system matrix to improve the quantitative accuracy of the reconstructions.

The general steps of the MLEM reconstruction are usually (see Figure 2.1):

1) The initial estimate of the 3D reconstruction image is created. Usually a uniform image is used as the initial reconstruction for the sake of simplicity;
2) The forward projection step: the projection estimate ($\sum_k C_{ik} X_k^l$) is computed based on the current estimate of the 3D reconstructed image (X_k^l), using the system matrix;
3) The error of the current projection estimate is calculated as the ratio of the measured projection P_i to the to the projection estimate ($\sum_k C_{ik} X_k^l$);

4) The back projection step: the error of the current reconstruction estimate ($\sum_i C_{ij} \frac{P_i}{\sum_k C_{ik} X_k^l}$) is calculated from the error of the current projection estimate, using the system matrix;
5) The current estimate of the 3D reconstruction is normalized and multiplied by the error of current reconstruction estimate to obtain the new reconstruction estimation.

Although the likelihood of producing the measured projection image increases as the iteration number increases, the reconstruction at a high iteration number can be very noisy [126,127]. In practice, the MLEM algorithm is usually stopped at a relatively low iteration number.

The OSEM algorithm accelerates the reconstruction by using only subgroups of the projection images to update the reconstruction estimation. For example, if the patient data is acquired with 15 projections and the image is reconstructed with the OSEM algorithm using 3 subsets. The measured projection is divided into 3 subsets containing the projection number: {1,4,7,10,13}, {2,5,8,11,14} and {3,6,9,12,15}. For each iteration, the OSEM reconstruction will update the image estimate with each one of the projection subsets, i.e. the OSEM will update the image estimate three times faster than the MLEM.

2.2.2.3 SPECT Camera, attenuation and scatter correction

As shown in Figure 2.2, a typical SPECT camera is mainly composed of two parts:

1) the detector which is used to record the energies and positions of the incoming photons emitted by the radiotracer.

2) the collimator (a think sheet of mental with high atomic number, pierced by an array of holes) which is mounted on the flat camera head to determine the trajectories of the detected photons.

The attenuation of photons in SPECT imaging depends on the distance traveled through the object before reaching the detector. Due to the attenuation effect, fewer photons are detected by the camera, leading to the underestimation of radioactivity (see Figure 2.2). The aim of the attenuation correction is to determine the number of photons emitted by the radioactive source (N_0), given the number of the photons detected by the camera (N). This can be achieved by solving the following equation:

$$N_0 = Ne^{\sum_i \mu_i \Delta x_i} \tag{2.2}$$

Where μ_i is the linear attenuation coefficient at the step i along the photon path, Δx_i is the distance traveled at the step i along the photon path.

In order to correct for photon counts loss due to the attenuation, it is important to determine the map of μ values for the object (attenuation map). In clinics, the attenuation map can be derived from the co-registered CT image (readily available for hybrid SPECT/CT system). Other methods such as a transmission scan with an external radionuclide source [128] or segmented magnetic resonance images [129] can also be used to generate the attenuation map. The attenuation correction factor, which is calculated based on the attenuation map, can be implemented into the system matrix during the iterative reconstruction process.

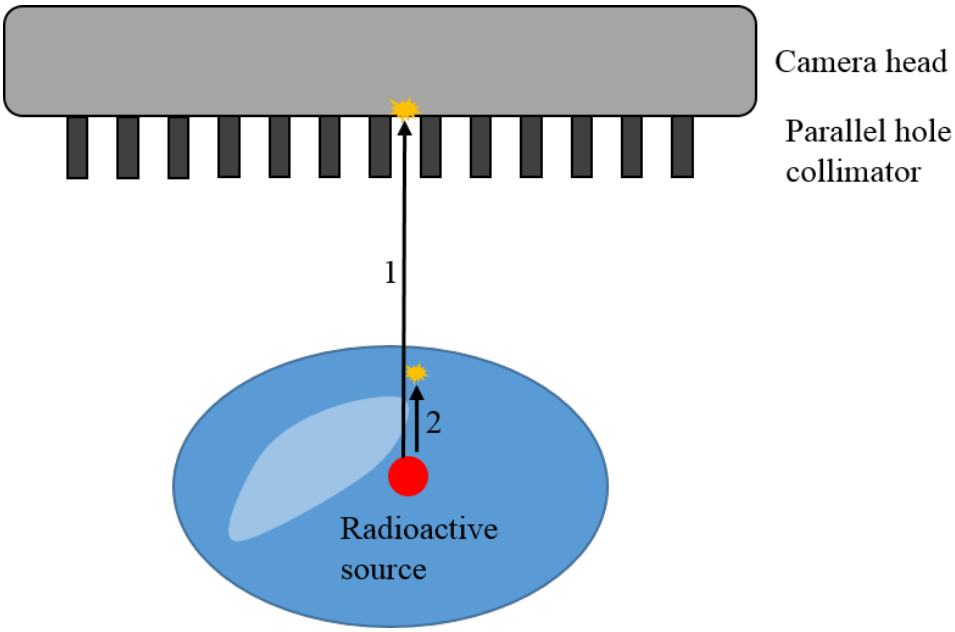

Figure 2.2 Illustration of the photon attenuation effect in SPECT acquisition. The arrows stand for the emitted photon paths. Photon 1 is properly collimated and provides useful information for activity quantification. Photon 2 is attenuated by the object and never reaches the camera head, resulting in underestimation of the radioactivity.

Scatter in SPECT acquisition usually refers to Compton scattering in which gamma photon interacts with matter, resulting in change of its direction and energy. When the scattered photons are detected by the camera, they will leave the impression that they come from the location that is different from that of the radioactive source (see Figure 2.3). Even for the radioisotope with single gamma emission, the energy of the scattered photon may fall within the range of the photopeak window. The situation becomes more challenging for the sources with multiple gamma emission as the scattered higher-energy emission could fall within the photopeak window of the lower-energy emission. If these scatter events are not properly corrected, the activity of the source will be overestimated.

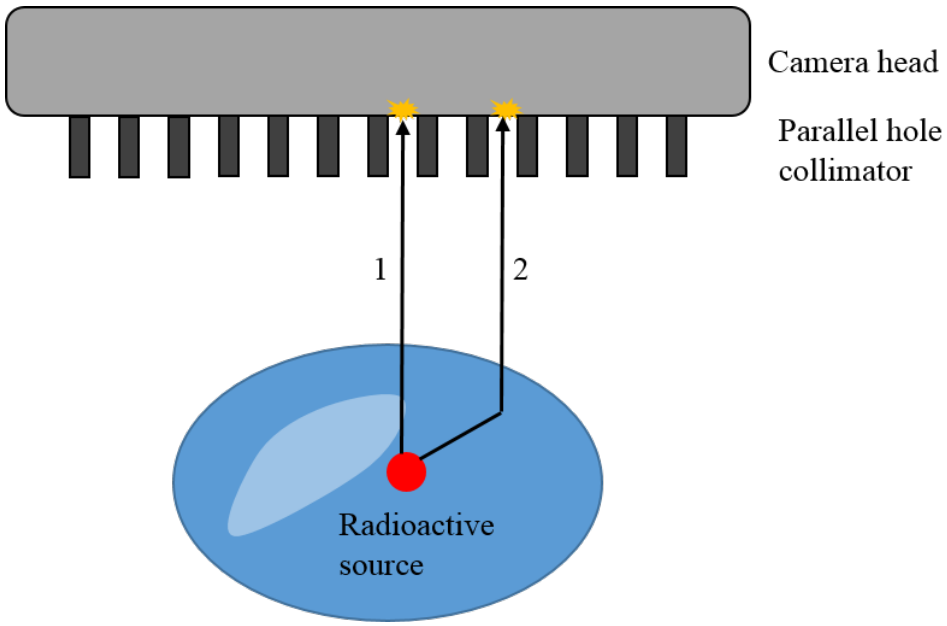

Figure 2.3 Illustration of the photon scatter effect in SPECT acquisition. The arrows stand for the emitted photon paths. Photon 1 is properly collimated and provides useful information for activity quantification. Photon 2 is scattered by the object, but still detected by the camera. This scattered count provides wrong information about the radioactive source location and energy.

Many methods have been developed for scatter correction in quantitative SPECT imaging [130]. In clinical studies, the most commonly used scatter correction techniques are the dual energy window (DEW) and triple energy window (TEW) methods, due to their simple implementation and fast execution even for complex scatter conditions [131]. These energy window based methods employ the counts measured in neighboring scatter windows to estimate the amount of scattered photons in the photopeak window (see Equation 2.3).

$$C_{scat} = \left(\frac{C_{LSW}}{W_{LSW}} + \frac{C_{USW}}{W_{USW}}\right)\frac{W_{PW}}{2} \tag{2.3}$$

Where C_{scat}, C_{LSW} and C_{USW} are TEW scatter estimate, lower scatter window (LSW) counts and upper scatter window (USW) counts, respectively. W_{PW}, W_{LSW} and W_{USW} are the window width of photopeak (PW), LSW and USW, respectively.

Despite their simplicity, these energy window based correction methods have been reported to achieve reasonable quantitative accuracy [132,133].

Other method such as convolution subtraction [134] has also been proposed for scatter correction in SPECT. One benefit of this method is it can provide additional information that might be relevant to the scatter conditions presented in a particular imaging study. However, this method requires additional effort for the measurement of the scatter kernels, which limit the popularity in busy clinics. Computationally expensive method such as analytical calculation of photon distribution [135] and Monte Carlo based approach [136] have been developed to achieve highly accurate scatter correction in complex scatter conditions. Many acceleration techniques have been used to make these scatter correction more efficient, which improves their potential for future clinical application [137,138].

Unlike the implementation of attenuation correction (where the correction factor is directly built into the system matrix), the estimated spatial distribution of the scattered photons is usually added to the denominator of the Equation 2.1 during the forward project step of the reconstruction. This scatter correction implementation method keeps the sparse property of the system matrix, allowing the reconstruction to be finished within clinically acceptable time.

2.2.2.4 Camera calibration

Once the attenuation and scatter effects have been corrected, an image with voxels representing the 3D distribution of primary photons (i.e. collimated photopeak window photons that are not scattered by either patient body or camera head) is obtained. The camera needs to be calibrated in order to translate the primary photon count map into absolute radioactivity map (i.e. in units of Bq or MBq). The camera calibration factor can be easily determined from a planar scan of a point source with well-known activity. The collimator and the energy window settings of this planar scan must be the same as those used in the SPECT acquisition. The planar calibration procedure relies on the assumption that the attenuation and scatter effects for the point source are minimal. Therefore, if all the image degrading factors are properly compensated during the image reconstruction, the planar calibration is expected to provide a good estimate of the radioactivity distribution within the object.

On the other hand, the system calibration factor can be obtained from a tomographic scan of a phantom containing extended source with activity concentration similar to that observed in patient images. Compared with the planar calibration, the SPECT scan is more cumbersome and usually requires handling much larger amount of activity. However, this method is expected to perform better for the case where the reconstruction algorithm is not fully quantitative, as the reconstructed images in both the calibration scan and the patient scan will suffer from similar quantification inaccuracies.

2.2.2.5 Camera dead-time correction

When high flux of photons hits the detector, dead-time effects may occur. Camera dead-time is defined as the time interval during which the system is incapable of recording another photon count, after one photon is recorded. Dead-time is not a concern for traditional NM diagnostic scans as low activities are used in these studies. However, dead-time might play an important role for the post radionuclide therapy scans, where patients are injected with much higher activities.

There are two models that characterize the system dead-time behavior: the paralyzable model and non-paralyzable model [139,140]. The main difference between these two models is that the photon count happening during the dead-time will trigger another dead-time for paralyzable system, while for non-paralyzable system the photon count during the dead-time will not extend the dead-time (see Figure 2.4).

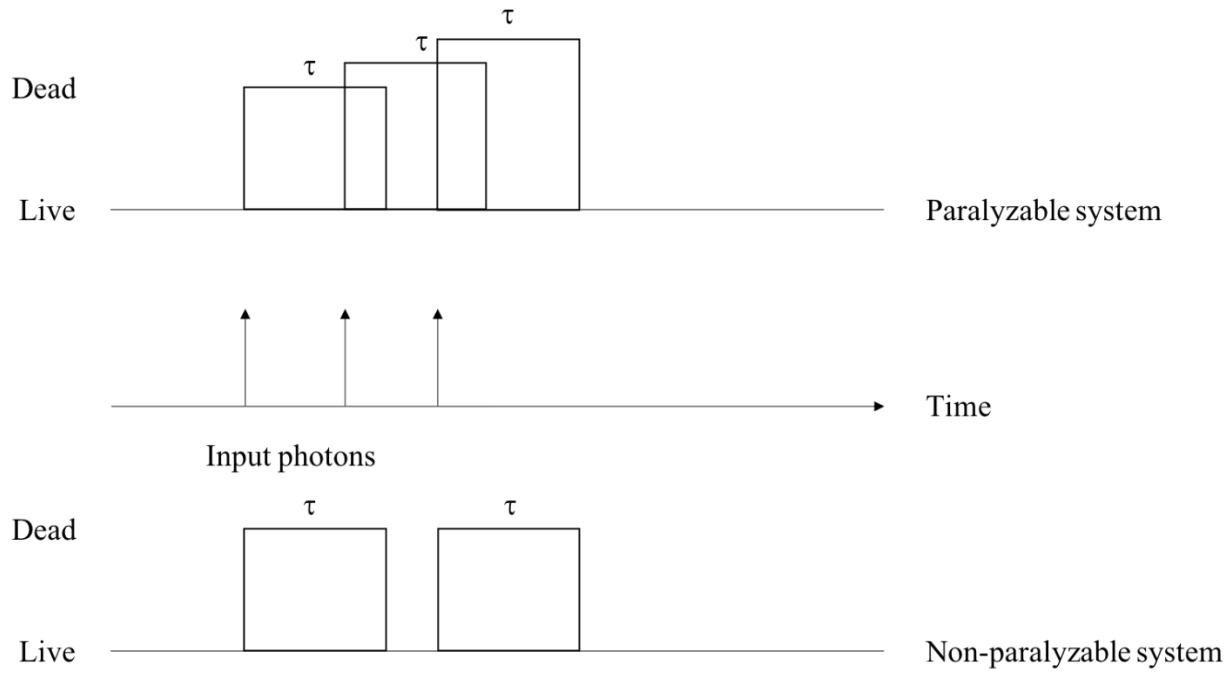

Figure 2.4 Comparison of the paralyzable and non-paralyzable dead-time behaviors, assuming the dead-time of the systems is τ. Both systems suffer from the dead-time effect, i.e. the observed counts are less than the true counts. In this example, in both cases there are three true counts. But the numbers of the observed counts are different. The paralyzable system will record only one count, while the observed counts in the non-paralyzable system are two.

Many methods have been proposed to correct for the dead-time effect in quantitative SPECT imaging. In general, they can be grouped into two categories. In the first method, the camera dead-time is determined from a series of phantom scans with different levels of activities [141,142]. The observed count rate is plotted against the true counts rate and the system dead-time is calculated based on the deviation of the fitted curve (to either paralyzable model or non-paralyzable model) from the line of equality. It should be noted that this method relies on the

assumption that the photon attenuation and scatter conditions are similar in both phantom study and patient scan. In the second approach, the system dead-time effect is measured using a small marker (point-like source) placed within the FOV of the camera [143]. The dead-time correction factor can be determined from the ratio of counts in the region of interest (ROI) around the marker in the image with dead-time (patient + marker) to the counts in the same ROI in the image without dead-time (marker only). One advantage of this method is that it does not require any assumption of dead-time behavior of the system.

2.2.2.6 Corrections related to the activity quantification in VOI

The effect that influences VOI activity quantification is the collimator detector response (CDR), which refers the image generated from the scan of a point-like source in SPECT imaging. The CDR is the primary factor that determines the system spatial resolution. There are two main components: 1) the intrinsic resolution of the camera (the detector and electronics), and 2) the geometric resolution, septal penetration and scatter components which are related to the collimator [144]. With proper selection of the collimator, the contribution of the septal penetration and scatter can be minimized. Unlike the intrinsic component which is constant for a given camera, the collimator related component increases as the distance between the source and the detector increases. For this reason, SPECT acquisition is usually performed with non-circular orbit in order to minimize the source-detector distance. Additionally, collimator resolution correction can be applied. The most common way for this correction is to build the point spread function template (usually Gaussian shape) into the system matrix and apply it during the iterative reconstruction [145]. This approach, however, significantly reduces the sparseness of the system matrix, resulting in increased computation time.

Even with proper modeling of the system CDR, the SPECT reconstructions still suffer from limited spatial resolution, which leads to the 'cross-talk' of activity between VOI and background. This spatial resolution related effect on VOI activity estimation is also known as partial volume effect (PVE). PVE depends on many factors such as imaging system characteristics, activity distribution, reconstruction algorithm etc. It has been shown to result in large errors for the activity quantification in small VOIs. Many methods have been developed to correct for the PVE. They are usually based on a recovery coefficient derived from the phantom experiments [146]. Alternatively, anatomical information provided by the high resolution CT images [147,148] can be used.

2.2.3 Dosimetry based on quantitative SPECT images

The knowledge of radiation dose absorbed by different organs in patient body is required to assess the risks and benefits of any NM therapeutic applications[149,150]. While in typical NM diagnostic procedures small amounts of radioactive material are used, the delivered doses are small and usually there is no need for dosimetry.

Once all the image degrading factors are corrected, a series of quantitative reconstructions can be used to determine the radiation dose to the organs of interest. According to the formalism proposed by Committee on Medical Internal Radiation Dose (MIRD): The mean internal dose $D\ (r_T, T_D)$ to a target organ, over a dose integration period T_D (usually from time zero to infinity), due to radioactive isotope presented in a source organ, r_S, is given by Equation 2.4 [150–152]:

$$D\ (r_T, T_D) = \sum_{r_S} \tilde{A}(r_S, T_D) \cdot S(r_T \leftarrow r_S) \quad (2.4)$$

Where $\tilde{A}(r_S, T_D)$ is the time-integrated activity in source region over dose integration period T_D and $S(r_T \leftarrow r_S)$ is the absorbed dose in the target organ per nuclear transformation. (Note: Source and target can be the same organ)

The absorbed radiation dose to a target organ depends on the fraction of administered activity accumulated and subsequently cleared from this organ, as well as the accumulation and washout in the surrounding region. Therefore, the estimation of time-integrated activities in both source region and surrounding tissues is required for calculating absorbed doses to target regions. The following parts of this section describe the most commonly used methods for time-integrated activity ($\tilde{A}$) estimate.

2.2.3.1 Time-integrated activity estimate

Time-integrated activity is defined as the total number of nuclear transformations in a source region over the dose integration period. To determine the time-integrated activity, the bio-kinetics of the radiopharmaceutical in the source organs needs to be determined. To achieve this, the following steps are usually performed:

1) A series of quantitative NM scans (planar or SPECT) are acquired at different time points after the radiotracer injection;
2) For each time point, the source organ is segmented and the corresponding activity is calculated;

3) The time-activity curve for each source organ is generated based on the measured data points;
4) The time-integrated activity is calculated as the area under the time-activity curve, which equals to the integration of time-activity curve over the dose integration period. As the integration period is usually from zero to infinity, proper time-activity curve fitting method is needed to accurately determine the time-integrated activity. The selection of the best fitting method depends on many factors such as the number of activity measurements, the temporal locations of these measurements and the bio-kinetics of the radiotracer in the source organ.

There are three imaging protocols that are usually used for the time-activity curve determination: the conjugate view planar method, the hybrid planar/SPECT method and the SPECT only method.

2.2.3.1.1 The conjugate view planar method

Traditionally, dosimetry calculations for radionuclide therapy have been based on conjugate planar imaging and geometric mean attenuation compensation, as described in MIRD pamphlet No. 16 [153]. This method employs source ROI counts delineated in two opposite planar images (anterior and posterior) to estimate the activity in the source organ at each time point. The attenuation correction factor is estimated from the patient's transmission scan data. Compared with the single planar view approach, the conjugate planar view method can incorporate corrections for source thickness and inhomogeneity, thus offers better source organ activity quantification [153]. This method, however, is known to have inherent limitations on accuracy of activity quantification due to VOI (tumours or organs)/ background region

overlapping and inability to perform exact correction for photon scatter and attenuation [154]. Additionally, only the mean dose to the target organ can be determined with planar data.

2.2.3.1.2 The hybrid planar/SPECT method and SPECT only method

Tomographic imaging techniques, such as SPECT, overcome these limitations, resulting in improved quantitative accuracy. Additionally, hybrid camera system combining SPECT with x-ray CT (SPECT/CT), can provide co-registered anatomic images of the patient, allowing for better identification of organ contours. Therefore, the recent dosimetry studies are usually performed using either the hybrid planar/SPECT method or the SPECT only method.

The hybrid method uses multiple planar scans and at least one SPECT/CT scan to determine the time-activity curve. The shape of the time-activity curve for the region of interest is determined from a series of planar imaging scans. Then the estimated shape is rescaled to the absolute activity value measurement by the SPECT/CT acquisition. This method is especially useful for the clinical situation where performing multiples SPECT/CT scans in not possible or the whole body information is crucial for the diagnosis and treatment planning [155].

For the SPECT only method, the activity changes in the source organ are accurately determined by performing a series of quantitative SPECT/CT scans at all desired time points. This technique is also known as the volumetric method.

Compared with the conjugate planar view method, both the hybrid planar/SPECT method and the SPECT only method offer better quantitative accuracy for the determination of radiation dose [156]. Moreover, benefiting from the 3D activity distribution information offered by SPECT images, the SPECT only method enables the radiation dose estimation at voxel level.

The voxel level dosimetry allows for the analysis of dose distribution, which might be valuable for the optimization of radionuclide therapy. It can also be used to create dose volume histograms, which have been widely used for treatment planning and tumour control probability prediction in external beam radiation therapy. However, careful selection of image reconstruction parameters and advanced data processing techniques are needed in order to obtain accurate 3D dosimetry information from NM images [157].

2.2.3.2 Methods for dose calculations

Once the time-integrated activity is determined for all source organs, the S value, which stands for: the absorbed dose in the target organ per one radioactive decay in the source organ, is used to calculate the dose to the target organ (Equation 2.4). The determination of the S value requires the knowledge of the radioactive source decay scheme (energies and intensities of all the emissions), as well as the source-target geometry. Many approaches are available for the calculation of the image-based dose value at either organ level or voxel level.

The organ mean dose calculation method uses organ level S value, which is calculated based on the standard human phantom assuming average body anatomy. These pre-calculated organ S values are readily available in many commercial dosimetry software packages such as OLINDA/EXM [158] and IDAC [159,160]. One limitation of these organ level S values is that the error of organ dose estimation might be substantial for the patient whose anatomy is significantly different from the standard human phantom.

In general, there are three approaches available for the calculation of voxel level dose [161]. The first approach is the dose point kernel, which represents the radial distribution of absorbed dose around an isotropic point source placed in an infinite homogeneous medium

(usually water). The voxelized form of dose point kernel is convolved with the source activity distribution to obtain the voxel level dose estimation. With modern computers, the voxel dosimetry based on this approach can be obtained very fast. However, the dose estimation is not reliable for the regions with inhomogeneous tissue density, such as the air-tissue interfaces in the lungs [162].

The second approach is the voxel S value, which is based on the similar principle to the dose point kernel method except the radioisotope is assumed to be uniformly distributed over the source voxel. Both these approaches allow for the application of the MIRD formalism (Equation 2.4) to generate voxel level dosimetry.

The third method is the direct Monte Carlo radiation transport. This approach is the most accurate method for absorbed dose calculation, but it is computationally expensive. The personalized dose estimation can be achieved by using patient's NM images for activity distribution and CT images as the Monte Carlo transport medium. It overcomes the drawback of first two methods and produces accurate dose estimation even for the inhomogeneous tissue density regions. Many Monte Carlo codes have been developed for the calculation of personalized radiation dose from NM images, such as Monte-Carlo N-Particle (MCNP) [163] and Geant4 applications for tomographic emission (GATE) [164].

2.2.4 The radioisotope of lutetium-177

Over the last several years, the lutetium-177 (^{177}Lu) has gained a lot of attention in both the NM research and clinical communities. The decay characteristics of ^{177}Lu, as well as the chemical properties, make it an ideal therapeutic agent for many types of cancers. In the

following parts of this section, the decay characteristics, production and NM application of ^{177}Lu are discussed.

2.2.4.1 Decay characteristics

^{177}Lu decays by beta minus to four states of ^{177}Hf (one ground state and three excited states). In this decay, four groups of electrons (each with continuous energy spectrum) and electron antineutrinos are emitted. The maximum and the average energies of the emitted electrons are 498.3 keV and 134.2 keV, respectively. At the same time, the three excited states of ^{177}Hf decay to the ground state, releasing gamma photons with discrete energies. Among these emitted gamma photons, two strongest emissions with energy of 208 keV (Intensity: 10.4%) and 113 keV (Intensity: 6.2%) are of interest in NM and have been successfully used in imaging studies for the quantification of ^{177}Lu [165,166]. A simplified decay scheme of ^{177}Lu is presented in Figure 2.5.

In addition to beta minus and gamma decays indicated in this figure, ^{177}Lu also emits conversion electrons, Auger electrons and X-ray radiation. The conversion electrons are emitted by the internal conversion process (de-excitation of the nucleus), which is a competing process with gamma decay. Moreover, when the electron of the atom is emitted (internal conversion in this case), it leaves a vacancy in the inner atomic shell. Then the outer shell electron fills this vacancy, resulting in the release of energy. This energy can either be released as characteristic X-ray or used to eject an Auger electron. Unlike the beta minus decay, discrete energy spectra are observed in the emissions of conversion electrons, Auger electrons and X-ray radiation. Table 2.1 summarizes the most intense emissions by ^{177}Lu.

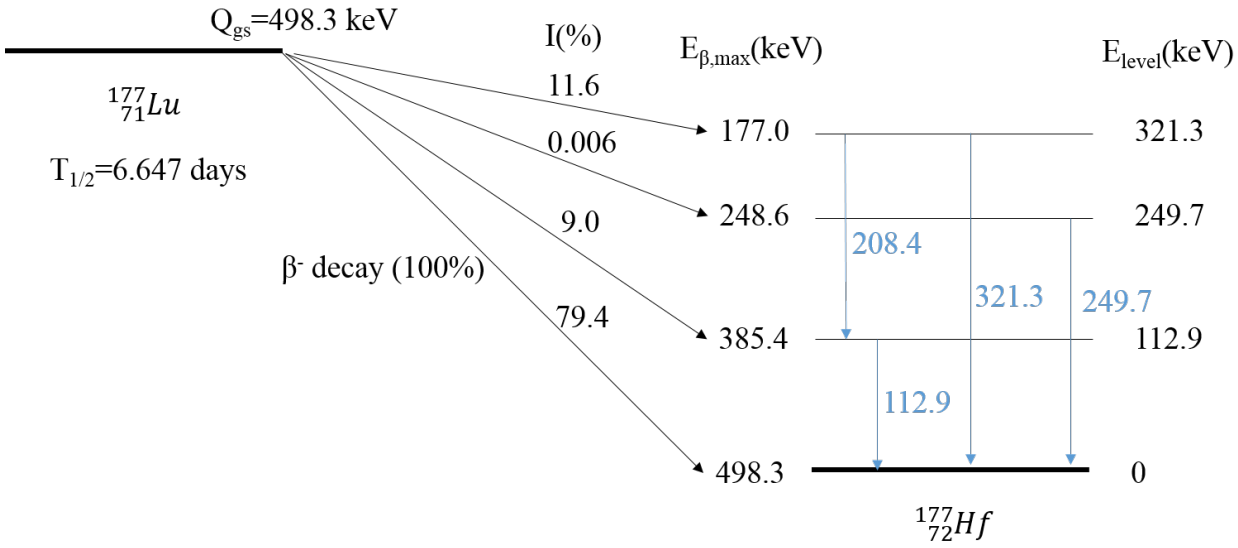

Figure 2.5 A simplified decay scheme of ^{177}Lu [167]**. Four beta minus branches as well as four gamma transitions with largest intensities are listed in the figure. The intensities of beta emissions are shown in black fonts while the energies of gamma transitions are shown in blue fonts.**

Table 2.1 Summary of the most intense emissions and their energies by ^{177}Lu [167]**. Only emissions with >1% intensity are listed. For X-ray radiation, only emissions with energy >50keV are included.**

Emission type	Intensity (%)	Energy (keV)
X-ray kα2	1.6	54.6
X-ray kα1	2.8	55.8

Emission type	Intensity (%)	Energy (keV)
Gamma	6.2	112.9
	10.4	208.4
Auger electron L	8.7	6.2
Conversion electron K	5.1	47.6
Conversion electron L	6.7	101.7
Conversion electron M	1.7	110.3
Beta minus	11.6	E_{max}=177.0
	9.0	E_{max}=385.4
	79.4	E_{max}=498.3

2.2.4.2 Production

Currently, ^{177}Lu is mainly produced by reactor-based methods, which can use either direct or indirect routes. The direct production route employs the ^{176}Lu (n, γ) ^{177}Lu nuclear reaction, which has large neutron capture cross section [168,169]. Due to the limited natural abundance (2.6%) of ^{176}Lu [170], the target usually needs to be enriched before it can be used to produce the ^{177}Lu. The final product is usually contaminated by many waste isotopes, such as the nonradioactive isotopes ^{176}Lu, ^{175}Lu and long lived (160.4 days half-life) radioactive isotope ^{177m}Lu [171]. The presence of these waste isotopes not only decreases the specific activity of the produced ^{177}Lu but also creates problems for radiation protection and waste disposal. Despite the drawbacks mentioned above, majority of the ^{177}Lu used in hospitals is produced by the direct

route because 1) it is a cost effective implementation, 2) it results in adequate specific activity of the product for medical use.

The indirect production route uses the neutron capture reaction of ^{176}Yb to produce the ^{177}Yb, which subsequently decays to ^{177}Lu by beta minus mode (1.9 hours half-life) [172]. This process can be described by the nuclear reaction: ^{176}Yb (n,γ) ^{177}Yb (β^- decay)→ ^{177}Lu. This method offers ^{177}Lu with the highest specific activity. It also has the potential to produce ^{177}Lu with highest possible radionuclide purity, meaning the long-lived radioactive wastes such as ^{177m}Lu are avoided. However, this production method is more technically demanding than the direct route and requires complicated radiochemical separation, as lutetium and ytterbium are adjacent isotopes of the lanthanide family with similar chemical properties [172,173].

Other production of ^{177}Lu such as the accelerator based methods have also been investigated [174,175]. Usually the deuteron induced nuclear reactions are used for ^{177}Lu production. Unlike the reactor based methods, these accelerator based production methods are currently not accepted as the basic approach for cost-effectively mass production of ^{177}Lu, due to extremely low cross sections for these reactions and associated technical challenges [171,176].

2.2.4.3 Application in NM

^{177}Lu has been widely used as a therapeutic radionuclide in NM due to its favorable nuclear decay characteristics (Figure 2.5), which includes 6.6 days physical decay half-life, low energy beta emissions for effective dose delivery of small tumours (2.0 mm maximum tissue range) [177] and gamma emissions that are suitable for SPECT imaging. Additionally, the chemical properties of Lu^{3+} allows easy and stable radiolabeling of many molecular carriers, which can be useful to target different types of cancers [178].

Many ^{177}Lu based radiopharmaceuticals have been developed and successfully applied in clinics over the past few decades. An important clinical application of ^{177}Lu is in the PRRT for the treatment of metastatic NETs. As discussed, ^{177}Lu radionuclide therapy has been recognized as one of the most effective and safe treatment options for the SSTR overexpressing NETs [179]. This application will be used as an example to evaluate the performance of the image-based dosimetry protocol developed in the following chapters of this thesis.

Additionally, ^{177}Lu-EDTMP has been evaluated in many pre-clinical and clinical studies as a radiopharmaceutical for the palliation of pain from bone metastasis [180–183]. A phase II study by Yuan et al. indicated that ^{177}Lu-EDTMP is an effective and safe (maximum tolerate dose 2,590 MBq) treatment for bone metastasis in patients with prostate or breast cancer [184]. ^{177}Lu labelled antibodies have been used for treatments of many types of advanced stage cancers that originated from breast, renal cells and colon [185–188]. Recently, ^{177}Lu PSMA-617 radioligand therapy has been proposed as a promising treatment option for patients with metastatic castration-resistant prostate cancer. The results of many clinical studies show that this therapy provides many benefits over the conventional treatments, such as high tumour response and low normal tissue toxicity [189–193].

Chapter 3: Camera calibration for the quantification of therapeutic radioisotopes

3.1 Introduction

In single photon emission computed tomography (SPECT), quantification of radiotracer distribution has recently become an increasingly important component of many clinical studies [113,194]. In particular, quantitative SPECT can be very helpful in the diagnosis of multi-vessel heart disease and assessment of myocardial blood flow reserve [195], as well as in quantitative evaluation of lungs, kidneys, brain [196] and other organs.

However, the most important role activity quantification has to play is in the targeted radionuclide therapies (TRT) [197]. The assessment of tumour burden, prediction of normal tissue toxicities and calculation of the dose are all necessary elements of the personalized, image-based therapy. They all require accurate absolute quantification of the amount of the radioactive material that is localized in tumour(s) and critical organs and characterization of its changes over time (bio-kinetics) [87,198].

There are three essential steps, which have to be performed for quantification of SPECT images. The first step involves quantitative SPECT reconstructions. Since the data acquired in projections are affected by physical phenomena such as photon attenuation and scatter, collimator blurring, camera dead-time and partial volume effects; in order to get quantitatively accurate images, all these factors must be properly compensated for during the reconstruction process. Fortunately, in the past few decades, considerable technical advancement has been

achieved in both SPECT hardware and data processing software. Particularly, with the introduction of hybrid SPECT/CT imaging systems and the development of statistical iterative reconstruction algorithms, quantitative reconstructions have become available for a majority of the commercial SPECT/CT cameras [118,199,200].

The second step is to apply the camera calibration factor (CF) to the reconstructed images, which will translate the three-dimensional (3D) count maps into 3D activity maps. The value of CF represents the joint sensitivity of the camera and the collimator for detection of a particular isotope's emissions in the energy window(s) that is used for data acquisition. Therefore, it depends on the energy of the measured photons and must be determined for each isotope and each energy window settings. Additionally, the value of CF might be influenced by the potential errors in dose calibrator readings when measuring the activity.

Finally, in order to obtain a quantitative value of the activity contained in any particular volume of tissue (for example in an organ or a tumour), the third step involving segmentation of this activity map must be performed. As segmented volumes will be affected by partial volume effects (PVE), for accurate activity quantification appropriate PVE correction methods need to be applied [201]. For example, one such method would be to use experimentally determined recovery coefficients (RC) [202,203].

To determine CF of the camera, an experimental measurement using phantom with an accurately calibrated radioactive source needs to be performed. Camera settings, including energy windows, collimator and the isotope must be the same as those used in patient study. Considering that quantitative reconstruction methods generate images from primary photons (PP) (as quantitative reconstruction has already removed the scattered photons and corrected for losses due to attenuation), CF must relate these PP images to the activity that produced them.

Different camera calibration methods have been proposed, but there is still no consensus which method is the best. Some researchers use planar scans of a small source (point source, **PS**) placed in air at a certain distance (usually 20-30cm) from the collimator surface [204–209]. This is a simple method where the CF is directly calculated from the acquired planar images. Care must be taken, however, that photon scatter is accounted for and that attenuation in the source and source support are minimized. Different small-volume geometries ranging from a vial or a syringe [205,208], a small container [204] or a petri dish (following NEMA protocol for camera sensitivity test [209]) have been employed. Some researchers even performed tomographic scans of such a point source [206], however, it is not clear what would be the advantage of such acquisition.

Alternatively, tomographic scans of large cylindrical phantoms containing accurately measured amounts of radioactive materials have been proposed [6,142,202,203,210–214]. This approach is more cumbersome, especially when radioisotopes with long half-lives are used. However, its rationale is that the geometry of the extended calibration phantom better models the body of a patient and the physical effects (photon attenuation and scatter) which occur in patients' acquisitions than the point source. Therefore, all approximations (and potential inaccuracies) due to the clinical reconstruction method which may affect the accuracy of patient images will be replicated in the reconstructed images of the calibration phantom. The geometries, which have been used in the extended phantom experiments can be divided into three categories: (a) small container(s) filled with activity (hot-sources, **HS**) placed in the large cylinder filled with non-radioactive water (cold-background, **CB**) [142,203,212,214], (b) small container(s) with activity placed in the large cylinder filled with radioactive water (warm-

background; **WB**) [211], and (c) large cylinders with no inserts, filled uniformly with activity (hot-cylinder; **HC**) [202].

The purpose of the present study is to evaluate all these methods, compare their performance and check if, and under what conditions, the planar calibration and tomographic calibration produce equivalent results. A large series of phantom experiments, as well as extensive simulation studies have been performed. The objective of the simulations (done with GATE Monte Carlo program [215]) was to generate the true CF values, and to investigate and understand the physical effects, which may be responsible for the discrepancies observed between CFs obtained using different experimental methods. In addition to ^{177}Lu, other popular therapeutic radioisotopes, such as ^{131}I and ^{188}Re, were also investigated.

3.2 Methods

The current study was composed of two parts: 1) phantom experiments and 2) Monte Carlo simulations. In both parts ^{131}I, ^{177}Lu and ^{188}Re radioisotopes were used and in total 21 experimental scans and 12 simulation runs were performed. The information about the isotopes' half-lives, their most intensive gamma emissions and maximum and mean energy of their beta emissions are provided in Table 3.1.

Table 3.1 Decay characteristics of ^{131}I [216]**, ^{177}Lu** [167] **and ^{188}Re** [217]**. For gamma emission, only intensities higher than 1% were listed.**

Isotope	Half-life	Strongest γ emissions	Mean β energy	Max β energy
		E_γ [keV] (I_γ [%])	E_{mean} [keV]	E_{max} [keV]
^{131}I	8.03 d	284(6.1)	181.9	970.8
		364(81.5)		
		637(7.2)		
		723(1.8)		
^{177}Lu	6.65 d	113(6.2)	134.2	498.3
		208(10.4)		
^{188}Re	17.00 h	155(15.6)	763	2120.4
		478(1.1)		
		633(1.4)		

3.2.1 Phantom experiments

For each isotope, the data were acquired using the following three experimental configurations (Table 3.2 and Figure 3.1):

A. Planar acquisition of a small source suspended in air (point source-**PS**; Table 3.2: experiments #1, #6-7, #15-17),
B. Tomographic (SPECT/CT) acquisition of hot inserts (spheres and/or cylinders) placed in non-radioactive water (hot source + cold background-**HS+CB**; Table 3.2: experiments #2-3, #8-9, #18-19),
C. Tomographic (SPECT/CT) acquisition of the same set of hot inserts placed in radioactive water (hot source + warm background-**HS+WB**; Table 3.2: experiments #4-5, #10-13, #20-21).

Additionally, for ^{177}Lu the following fourth configuration was used:

D. Tomographic (SPECT/CT) acquisition of a cylindrical phantom filled with uniform activity (hot cylinder-**HC**; Table 3.2: experiment #14).

All data acquisitions were performed using Symbia SPECT/CT cameras (Siemens Healthineers, Germany). The acquisitions #6-13 for ^{177}Lu and #15-#21 for ^{188}Re were performed at the Vancouver General Hospital, Nuclear Medicine Department, Vancouver (Canada). Experiments with ^{131}I (acquisitions #1-5) were done at the Department of Radiology, University

of Michigan Medical School, Ann Arbor (USA). Finally, the ^{177}Lu acquisition #14 was performed at the Department of Radiology and Nuclear Medicine, Université Laval, Quebec (Canada). The acquisition conditions, the camera model, the collimators, and the total activities used in the experiments are specified in Table 3.2.

Table 3.2 Parameters of acquisitions and source activities used in phantom experiments.

Experiment number #	Isotope	Camera & Collimator	Experimental Configuration	Total Phantom Activity [MBq]	Source-Collimator Distance [cm]
1	^{131}I	SymbiaT	A → PS	24.35	25
2			B → HS+CB	16.02	Non-circular
3		HE (High		20.76	orbit
4		Energy)	C → HS+WB	89.54	
5				203.86	
6	^{177}Lu	SymbiaT	A → PS	11.70	36
7				13.10	35
8		ME	B → HS+CB	446.79	Non-circular
9		(Medium		277.50	orbit
10		Energy)	C → HS+WB	681.26	
11				489.08	
12				2486.60	
13				2459.89	
14			D→HC	659.60	

Experiment number #	Isotope	Camera & Collimator	Experimental Configuration	Total Phantom Activity [MBq]	Source-Collimator Distance [cm]
15	^{188}Re	SymbiaT	A → PS	14.15	30
16				16.25	13
17		HE (High		119.02	13
18		Energy)	B → HS+CB	664.0	Non-circular
19				554.0	orbit
20			C → HS+WB	491.0	
21				1193.0	

Figure 3.1 Examples of experimental configurations used in planar (A) and tomographic (B) acquisitions.

For experiments performed using Configuration A, the volume of the point source was always equal to or less than 1mL. In each case, a syringe containing the point source was suspended in air between the detectors and it was equally spaced from each collimator surface (Figure 3.1A and Table 3.2). The scan duration ranged from 5 min to 20 min.

For tomographic acquisitions, cylindrical phantoms with hot spherical and/or cylindrical inserts were used (Figure 3.1B and Table 3.2). The total volume of the hot inserts varied between experiments and ranged from 58mL to 560mL, while the volume of the cylinder was about 6L (Jaszczak phantom) or 10L (Elliptical Thorax phantom). In the experiments where inserts were placed in the hot-background, the ratio of sphere to background activity concentration was always close to 6:1 (which corresponds to that often observed in clinical studies).

For each phantom configuration and each experiment, the total activity in the phantom was sufficiently low that the camera did not display any dead time effects. For all scans, the projection data were acquired in three abutting energy windows, namely the 20% photopeak window (PW), the lower scatter window (LSW) and the upper scatter window (USW). The data in these three windows were subsequently used to perform triple energy window (TEW) scatter correction. The acquisition times ranged from 8s to 40s per projection with a total of 60-90 projection (30-45 camera stops). Table 3.3 provides energy window settings used in our experiments and simulations (for ^{177}Lu, only the 208keV photopeak was used).

Table 3.3 Energy window settings for ^{131}I [152], ^{177}Lu [218] and ^{188}Re [219] used in the experimental acquisitions and in the simulations.

Isotope	Photopeak window (PW) [keV]		Lower scatter window (LSW) [keV]		Upper scatter window (USW) [keV]	
	Center	Range	Center	Range	Center	Range
^{131}I	364	328-400	317	306-328	411	400-422
^{177}Lu	208	187-229	167	146-187	249	229-270
^{188}Re	155	140-171	136	132-140	175	171-178

3.2.2 Monte Carlo Simulation Experiments

The Geant4 Applications for Tomographic Emission (GATE version 6.1 [215]) Monte Carlo code was used for the simulated experiments. The Siemens SymbiaT dual head SPECT imaging system was modeled. The system geometry (detector, collimator and shielding) used in our simulations was identical to that described and validated in our previous study [220].

The emission energy spectra of the three isotopes, which have complex decay schemes, are built-in into GATE and included accurate modelling of β^- and gamma emissions. The simulated radionuclides were distributed uniformly within their respective source volume, as described in the next paragraph.

For each radionuclide, four phantom configurations (analogous to those used in the experiments) were simulated:

I. point source (1 mL sphere) in air.

II. 100mL spherical source placed in the center of a cylinder filled with non-radioactive water.

III. 100mL spherical source placed in the center of a cylinder filled with radioactive water.

IV. cylinder filled with uniform activity.

In all simulation experiments, the phantoms were placed at the center of the field of view (FOV) of the camera. The distance from the source to each of the collimator surfaces was equal to 25 cm. The cylindrical phantom used in these simulations had the same dimensions as that used in the experiments. Although multiple inserts with different sizes were used in the phantom experiments, while only a single sphere was used in the simulations, the characteristics of photons recorded by the camera when using this simple phantom model were very similar to those from the experiments, providing us with information sufficient to explain discrepancies in CF values obtained from different methods.

The total number of decays (N_{tot}) simulated for each phantom configuration and corresponding activities (assuming in each case 5 min acquisition time) are listed in Table 3.4 (N_{tot} was selected so that the total number of photons detected in PW was more than 15000 in order to ensure errors are <1%). For each simulation experiment, the projection images corresponding to the true primary photons, the total photons recorded in the photopeak window (PW), as well as those recorded in the two scatter windows (LSW and USW) were generated.

Table 3.4 Total number of decays used in the simulation experiments. Additionally, for each radioisotope, activities (in MBq) corresponding to these simulations, assuming 5-minute acquisition times, are provided (in brackets).

	N_{tot} (total activity [MBq])				
Isotope	Conf. A→PS	Conf. B →HS+CB	Conf. C[1]	→HS+WB	Conf. D →HC
^{131}I	5E8 (1.7)	1E9 (3.3)	Sphere	2.6E8 (0.9)	3E9 (10)
			Bkg	2.7E9 (9)	
^{177}Lu	1E9 (3.3)	2E9 (6.7)	Sphere	1.7E9 (5.7)	2E10 (66.7)
			Bkg	1.8E10 (60)	
^{188}Re	3.5E8 (1.2)	2E9 (6.7)	Sphere	1.1E9 (3.7)	1.2E10 (40)
			Bkg	1.2E10 (40)	

[1] The number in decays in the sphere and the background was specified so that the ratio of activity concentrations was equal to 6.

For all phantom configurations, only one planar projection was simulated for each of the photopeak windows (PW) and for each of the two scatter energy windows (LSW and USW). Benefiting from the cylindrical symmetry of the simulated phantoms, the tomographic images were created by replicating these single projections 90 times with Poisson noise added to the data.

3.2.3 Image Reconstruction

The images from the experimentally acquired tomographic projection datasets, as well as those from simulations, were reconstructed using in-house developed software packages (MIRG software [218] for ^{177}Lu and ^{188}Re, UM software [221] for ^{131}I). In all cases, the OSEM algorithm (Table 3.5), with CT-based attenuation correction and TEW scatter correction [222,223] was employed.

Additionally, ^{177}Lu experimental datasets were reconstructed using the Siemens software available on the camera (Flash3D) [210]. By definition, these reconstructions included resolution recovery (RR) correction. This correction, however, should have no effect on the total number of counts recorded in the reconstructed image. Therefore, CFs obtained from images reconstructed with and without RR should be considered as equivalent. In all cases, the matrix size was 128x128x128 with the pixel size equal to 4.79mm.

Moreover, for each isotope and each phantom configuration, the images were reconstructed from the simulated data corresponding to the primary photons only. In this case, no scatter correction was required so only attenuation correction was included in the reconstruction. The attenuation maps used in all reconstructions of the simulated data were generated using cylindrical phantom shapes filled with narrow-beam attenuation coefficients.

Table 3.5 Parameters used in the reconstructions of images from experimental and simulated tomographic data (experiments performed using configurations HS+CB, HS+HB and HC).

Isotope	Reconstruction	Iterations	Subsets
^{131}I	UM Software [221]	35	6
^{177}Lu[1]	MIRG qSPECT [218]	6	10
	Siemens Flash3D [210]	6	10
^{188}Re	MIRG qSPECT [218]	6	10

[1]For the reconstruction of phantom experiment D (performed at Quebec), 12 subsets which were used as the tomographic data were collected with 96 projections.

3.2.4 Determination of Camera Calibration Factor (CF)

The camera calibration factor (CF) can be determined using the following general formula:

$$CF = \frac{C}{A\,t} \tag{3.1}$$

Where: C is the number of photons emitted by the source having the activity A and recorded by the camera in time t. This general formula formed the bases of all our data processing; the details of calculations are summarized in Table 3.6a and Table 3.6b. For

simulated data, the product of activity and time was replaced by the total number of decays (Table 3.6b).

Planar acquisitions (Experimental and Simulated Configurations - PS)

For planar acquisitions, the CF was directly calculated from the acquired planar images, no reconstruction was required. The counts collected in the entire field of view of the camera were employed and C_{PWSC} corresponding to the PW counts corrected for scatter using the TEW method was used.

Additionally, our simulated data provided us with the estimate of the number of primary photons. This allowed us to calculate C_{PPsim} (the "true" CF), which was not affected by approximations related to the TEW scatter correction.

Tomographic acquisitions (Experimental and Simulated Configurations – HS+CB, HS+HB and HC)

For tomographic phantom experiments, the total numbers of counts, summed over the entire 3D image, were used to determine the CFs corresponding to each isotope and each phantom configuration.

Additionally, for simulated data, the CF factors were calculated using the images reconstructed from primary photons only (Table 3.6b).

In Table 3.6, the CF symbols corresponding to the values obtained from planar data are marked with subscript *PW* for "photopeak window" and *PWSC* for "photopeak window scatter

corrected"; CF obtained from tomographic data are marked with subscript *R* for "reconstructed" and superscript *B, C or D* indicating configuration of the phantom. Furthermore, the CF obtained from simulated data was labeled with subscript *sim*, while CF calculated from primary photons only are additionally marked with subscript *PP*.

Table 3.6a Techniques used in CF determination from the experimental data.

Config	CF	Definitions		
		Counts	**Time**	**Activity**
A	CF_{PWSC}	Count in PW corrected for scatter using TEW: C_{PWSC}	Scan time: t	Small source activity: A
B	CF_R^B		Number of projections	Total activity in spheres: A
C	CF_R^C	Total counts in the image reconstructed with AC+SC: C_R	multiplied by the projection duration: $n_p t_p$	Total phantom activity: A
D	CF_R^D			

Table 3.6b Techniques used in CF determination from the simulated data.

Config	CF	Definitions	
		Counts	**Product of time and activity**
A	$CF_{PWSCsim}$	Count in PW corrected for scatter using TEW: $C_{PWSCsim}$	Total number of simulated decays: N_{tot}
	CF_{PPsim}	Primary photons simulated in PW: C_{PPsim}	
B	CF^{B}_{Rsim}	Total counts in the image that was reconstructed from PW with AC+SC: C_{Rsim}	
	CF^{B}_{RPPsim}	Total counts in the image reconstructed from primary photons only with AC: C_{RPPsim}	Number of projections multiplied by number of decays simulated in each projection: $n_p N_{tot}$
C	CF^{C}_{Rsim}	Total counts in the image that was reconstructed from PW with AC+SC: C_{Rsim}	
	CF^{C}_{RPPsim}	Total counts in the image reconstructed from primary photons only with AC: C_{RPPsim}	
D	CF^{D}_{Rsim}	Total counts in the image that was reconstructed from PW with AC+SC: C_{Rsim}	

3.3 Results

Figure 3.2 presents the energy spectra for the three investigated radioisotopes, generated by our GATE simulations. The phantoms used in these simulations corresponded to a point source scanned in air (blue line), a 100mL sphere filled with activity placed at the center of a cylinder filled with cold (black line) and warm (red line) water.

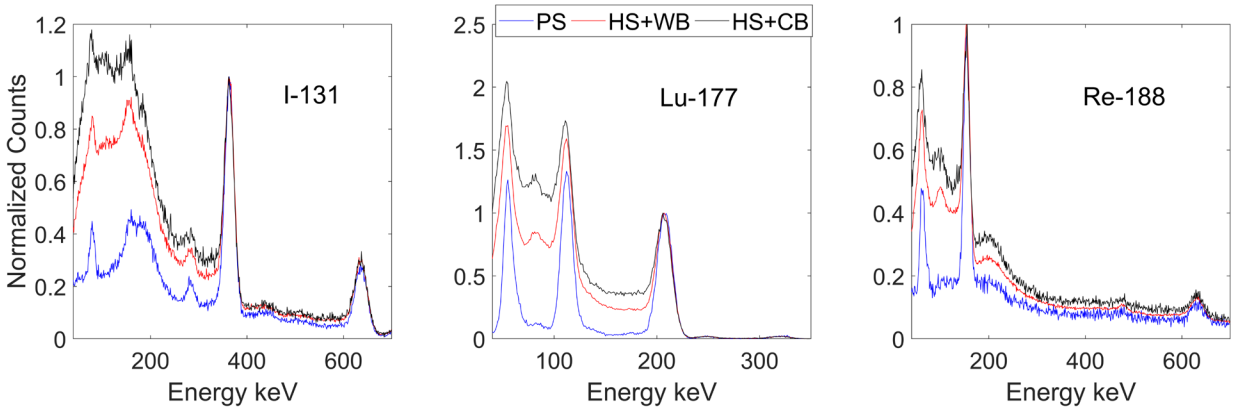

Figure 3.2 Simulated energy spectra as would be acquired by the SPECT camera from emissions of ^{131}I, ^{177}Lu and ^{188}Re. For each isotope, a point source scanned in air (blue line), a 100-mL hot sphere placed at the center of a 20cm diameter cylindrical phantom filled with non-radioactive water (black line) and warm (red line) water were simulated.

Table 3.7 and Table 3.8 summarize the CF values obtained using all planar and tomographic configurations (as outlined in Table 3.6) from simulations and phantom experiments, respectively. Additionally, these results are presented in a graphical form in Figure 3.3 and Figure 3.4. Since the CF values for ^{177}Lu data obtained from MIRG and Siemens

reconstructions agreed to within 3%, only CF from MIRG reconstructions were used in the subsequent analysis.

In order to facilitate comparison of CFs obtained from different experiments with different phantom configurations, the CF values in Figure 3.3 and Figure 3.4 are presented in relative units. For simulated data, shown in Figure 3.4A CF obtained from primary photons recorded in the photopeak window of the planar acquisition of a point source were considered to be the "true" CF values and were set to 1. For the experimental data presented in Figure 3.3 and for simulations shown in Figure 3.4B, the data were normalized using counts in the planar acquisition of a point source corrected for scatter, i.e. CF_{PWSC} and $CF_{PWSCsim}$, respectively.

Table 3.7 Experimental camera CF determined using different phantom configurations.

Experiment	Isotope	Configuration	CF [cps/MBq]	Mean CF value [cps/MBq]
1	^{131}I	A → PS	58.32	58.3
2		B → HS+CB	59.94	60.5
3			61.10	
4		C → HS+WB	56.91	55.0
5			53.05	

Experiment	Isotope	Configuration	CF [cps/MBq]	Mean CF value [cps/MBq]
6	^{177}Lu	A → PS	9.94	9.4
7			8.93	
8		B → HS+CB	11.04	10.5
9			9.87	
10		C → HS+WB	9.75	9.5
11			9.68	
12			9.84	
13			8.90	
14		D→HC	10.10	10.1
15	^{188}Re	A → PS	15.8	16.5
16			17.56	
17			15.99	
18		B → HS+CB	18.64	18.5
19			18.26	
20		C → HS+WB	15.09	15.5
21			15.95	

Table 3.8 Camera CF obtained using simulated data.

Isotope	Configuration A [cps/MBq]		Configuration B [cps/MBq]		Configuration C [cps/MBq]		Configuration D [cps/MBq]	
	$CF_{PWSCsim}$	CF_{PPsim}	CF^{B}_{Rsim}	CF^{B}_{RPPsim}	CF^{C}_{Rsim}	CF^{C}_{RPPsim}	CF^{D}_{Rsim}	CF^{D}_{RPPsim}
^{131}I	65.74	66.51	69.23	65.55	67.05	67.63	66.54	67.04
^{177}Lu	11.18	11.33	12.44	11.32	11.49	11.59	11.51	11.54
^{188}Re	17.60	18.37	20.47	17.98	18.29	18.77	18.51	18.98

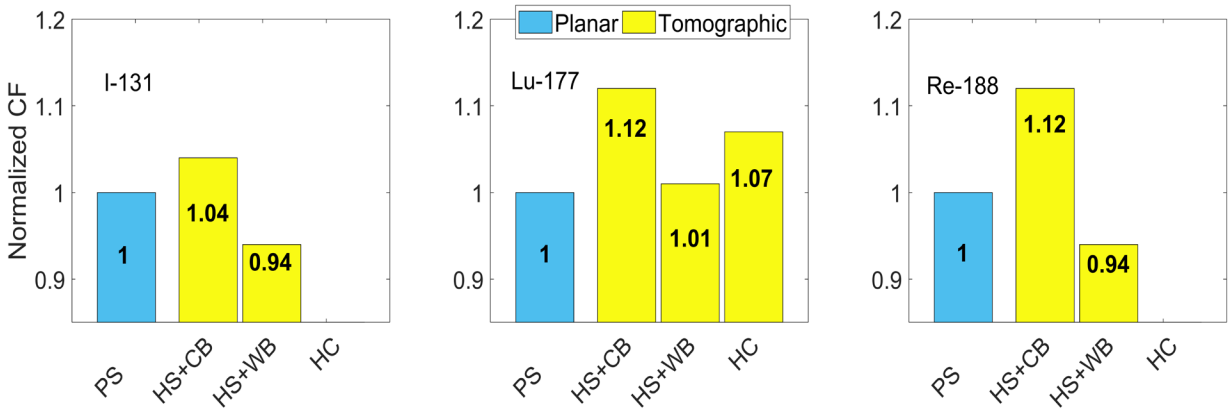

Figure 3.3 Summary of CF obtained experimentally using different phantom configurations. The data were normalized using counts in the planar acquisition of a point source corrected for scatter with TEW.

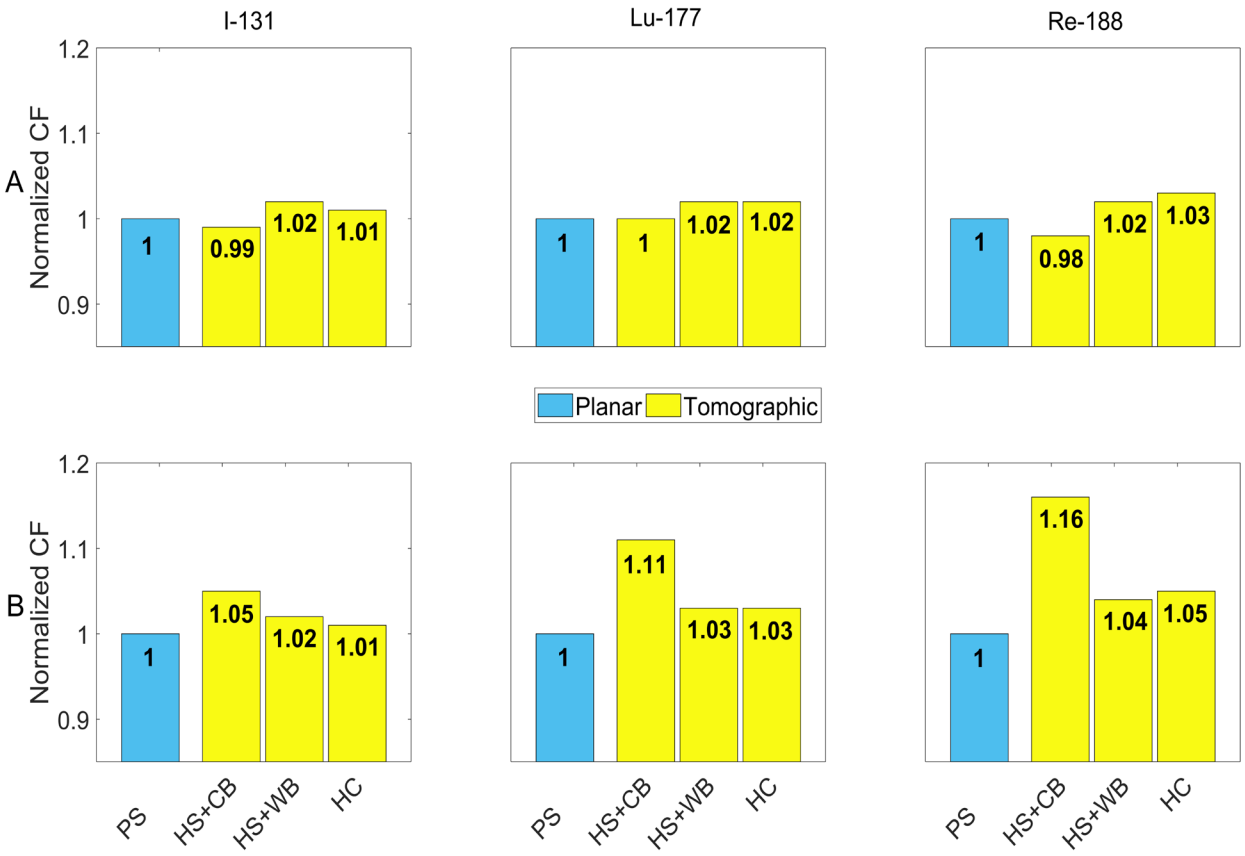

Figure 3.4 Summary of CF obtained from simulated phantom experiments performed using different phantom configurations. Part (A) shows CFs obtained from primary photons only normalized using CF_{PPsim}, while CFs shown in part (B) were calculated using total counts recorded in the photopeak window corrected for scatter with TEW and normalized using $CF_{PWSCsim}$.

3.4 Discussion

The spectra presented in Figure 3.2 allow us to evaluate the contribution of scattered photons to the photopeak energy window for different phantom configurations. While scatter component in point source (PS) scans of ^{177}Lu is relatively low, for ^{131}I and ^{188}Re, the photons from high energy gamma transitions, which were scattered mostly in the camera head, substantially increase the background. This observation supports our claim that scatter correction should be performed even when CF is derived from the data obtained using planar scans of point sources. The scatter correction method which is the most popular in clinics is TEW. Besides being simple and easy to implement, TEW allows us to correct not only for self-scattered photons, but also for high-energy scatter and other background.

Further analysis of the data presented in Figure 3.2 confirms that scatter correction should be included in all tomographic image reconstructions. All energy spectra for HS+CB and HS+WB phantom configurations that were used in our tomographic acquisitions, and which model patient scans better than point sources, display large scatter background under the photopeaks.

For all isotopes (^{131}I, ^{177}Lu and ^{188}Re), the experimental CFs (Figure 3.3 and Table 3.7) show relatively good agreement between CF_{PWSC} obtained from planar scans corrected for scatter and CF_R^C obtained from tomographic scans performed using hot sources placed in warm background (HS+WB). These CF values agree to within 6%. The agreement usually improves (to below 3%) when CF obtained from the experiments performed on the same day are considered. This improvement may be attributed to the fact that for the same-day experiments all

errors in activity determination are minimized, as the activity measurements are performed using the same vial and same dose calibrator settings. However, the differences between CF_{PWSC} and CF_R^B (HS+CB) values are much larger, for ^{177}Lu and ^{188}Re even reaching 12%.

The explanation of all these effects can be provided by the analysis of our Monte Carlo simulation results. Firstly, as expected, when considering only primary photons, for all radioisotopes CFs obtained from planar scans (CF_{PPsim}) and those reconstructed from tomographic data (with attenuation correction) agree to within 1-3% (Table 3.8 and Figure 3.4A). Such small differences may be caused by statistical fluctuations and small approximations in attenuation correction used in the reconstructions of the simulated tomographic data (voxelized attenuation maps were used in reconstructions, while in GATE analytical shapes were used).

However, larger discrepancies, similar to those observed in experimental data, are found when comparing CFs obtained from simulated PS scans corrected for scatter $CF_{PWSCsim}$ and simulated tomographic scans (Table 3.8 and Figure 3.4B). The differences between $CF_{PWSCsim}$ and both CF_{Rsim}^C and CF_{Rsim}^D remain below 5%, while CF_{Rsim}^C and CF_{Rsim}^D agree with each other to within 1%. However, the differences between $CF_{PWSCsim}$ and CF_{Rsim}^B increase to 12-16%. These effects are caused by the approximations of the TEW scatter correction method, which can be visualized when considering the shapes of the profiles presented in Figure 3.5.

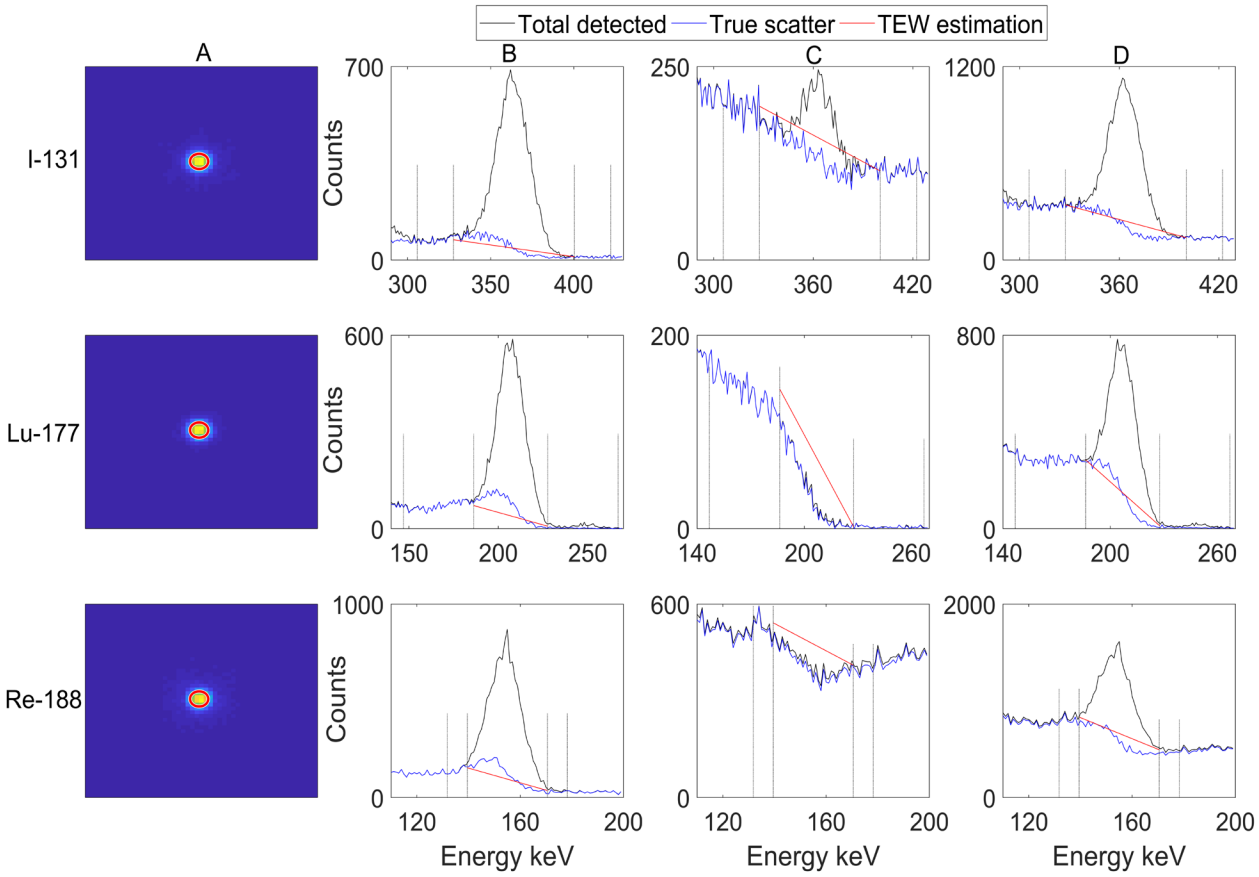

Figure 3.5 Energy spectra obtained from the simulations of the phantom scanned in configuration B (HS+CB). The counts recorded in the photopeak window and correspond to the ROI drawn on the projection images: around the hot object (column B), in the background surrounding this ROI (column C) and in the entire image (column D). Column A shows the simulated PW projections. The hot object ROI was placed inside the red circle while the background ROI comprised all counts found on the outside of the red circle.

Simulated spectra presented in Figure 3.5 correspond to the phantom configuration B (HS+CB). The graphs compare the shapes of the photopeak, the true scatter component observed

in PW and the scatter estimated by the TEW method using counts recorded in LSW+USW. Counts in the three regions were analyzed. Spectra presented in Figure 3.5B correspond to counts recorded in the source ROI and Figure 3.5A shows the location of the source ROI drawn in the projection images of each isotope. Spectra in Figure 3.5C correspond to counts recorded in the background region around the source, and Figure 3.5D shows spectra of counts recorded in the entire image (these counts were used for the CF determination). Please note that Figure 3.5C for ^{131}I contains a small peak corresponding to septal penetration of the collimator by 364keV photons.

The analysis of these graphs clearly demonstrates that for all isotopes, the TEW method (area under the red line) underestimates the true scatter (marked by the blue line) in the source ROI region while overestimates it in the background region. As a result, the source region seems to have more counts, while counts in the background around the source seem to be lower than they should be. This “surplus” is further enhanced by the attenuation correction, which boosts the excess of counts in the source region, because it is located in the center of the phantom where attenuation correction is the highest. On the other hand, the overestimation of scatter counts in the background potentially might have created negative counts. These, however, will be set to zero by the reconstruction algorithm as TEW scatter prediction was added to the estimated projection in the OSEM reconstruction. As a result, the total number of reconstructed counts used for CF calculation is higher than the truth, and also higher than that determined from planar scans. This effect is relatively smaller for phantom configurations in which activity is distributed over the entire phantom (HS+WB and HC).

Additionally, please note that although CFs determined experimentally and obtained from simulations are quite similar, CF from simulations exceed experimental values by 3-10%. In our

opinion, these differences should be attributed to approximations made in the simulated camera model [220] and inaccuracies in dose calibrator measurements of source activities.

At this point, it is important to emphasize that the CF value, as defined in our study, corresponds purely to the camera efficiency for given radioisotopes, collimator and energy window settings. It does not depend on the image resolution, the size and shape of the imaged object, the signal-to-background ratio and other factors. Although some authors propose to combine CF and RC into a single calibration coefficient [224], such approach would be very challenging, as it is impossible to design a calibration experiment which would model every patient geometry and every activity distribution. More importantly, in order to account for these different conditions, such a "combined" approach would require not a single value of CF, but a large table of values, which additionally would depend on the segmentation method that was used to generate RC.

This is not to say that the proposed method of CF determination allows us to avoid the challenges related to image segmentation. Still the activity maps, which are obtained by multiplying patient images (i.e. count-maps) by CF, must be segmented if one wants to get activity in any particular volume. The advantage of the proposed method is that CF determined using a single planar scan can be repeatedly applied to many patient studies, as long as they were acquired using the same camera, collimator, radioisotope and energy window settings. It has been shown that, under normal exploitation conditions, the camera sensitivity (thus this CF) will remain unchanged over a long period of time [208].

Actually, another observation from this study (and also from our previous experience) is that often calibration experiments performed using the same type of camera (from the same manufacturer) and same acquisition protocols (collimator and energy window settings) but

located in different Nuclear Medicine departments (often even in different countries) result in very similar values of CFs. This fact may be illustrated by the experimental CFs for ^{177}Lu phantom configuration C and D, which agree well (within 6%) in spite of the fact that one of these studies was done using Siemens camera located in Vancouver and the other camera in Quebec City.

3.5 Conclusions

The planar acquisition of a point-like source provides CF very close to those obtained from tomographic images (reconstructed with attenuation and scatter corrections) of a phantom where the activity is distributed over the entire volume (with or without the hot object(s) in its center). The value of CF determined using these two approaches agree to within 3% when experiments are performed on the same day and to 6% for experiments done over the period of several months. Usually such phantom configuration is considered a good approximation of activity distribution encountered in clinical patient studies. However, our analysis suggests that, for all investigated radiotherapy isotopes, the camera calibration based on a planar scan of a point source must include scatter correction. This is because photopeak windows for ^{131}I and ^{188}Re, and to a lesser degree for ^{177}Lu, contain important components from scattered high-energy gamma emissions (and septal penetration for ^{131}I).

Additionally, our experiments indicate that camera calibration performed using tomographic scan of a source placed in non-radioactive (cold) background may overestimate CF by more than 10% (thus this calibration method is not recommended). Analysis of simulations helped us to understand that this large discrepancy is due to the approximations made by the

TEW scatter correction, even further enhanced by attenuation correction performed during image reconstruction.

Based on these considerations we conclude that camera CF may be confidently determined using planar scans of the point source, providing that the scatter and background contribution to the photopeak are removed, for example using the TEW method. The approach is simple and easy to perform, and provides CF with sufficient accuracy (~5%) to be used in clinical quantitative imaging studies. The proposed method is general and is expected to provide good results for other isotopes than those reported here.

Chapter 4: Quantification performance of the Siemens Flash3D reconstruction software for ^{177}Lu

4.1 Introduction

As discussed in Chapter 1, dosimetry for critical organs and tumours is important for improving the treatment efficacy of the ^{177}Lu DOTATATE radionuclide therapy. However, image-based dose calculations require quantitative measurement of activity distribution within patient body. In response to this requirement, substantial expertise of quantitative ^{177}Lu imaging has been acquired by our group and other investigators using both phantom and patient studies. Usually the in-house developed reconstruction software packages were employed for the imaging of ^{177}Lu placed in different attenuation and scatter medium [203,218], resulting in good quantification accuracy of the reconstructed images. For example, Shcherbinin et al. showed that the errors of ^{177}Lu activity quantification based on the in-house developed algorithm remained below 2%, for phantom experiments containing ^{177}Lu source and ^{90}Y/^{177}Lu mixed source [165]. A study by Hippeläinen et at. used a torso phantom with nine spherical ^{177}Lu sources to test the performance of quantification [203]. The error of activity in the largest sphere, obtained from the images reconstructed using in-house developed algorithm, was reported to be 15%.

However, these in-house developed reconstruction algorithms would be very difficult to apply on a widespread scale in clinical studies, because they are often computation expensive, time consuming and/or may require manual user interventions.

Therefore, it is expected that the patient images acquired in routine PRRT clinical studies will be reconstructed using commercial software that comes with SPECT/CT cameras, such as the Flash3D algorithm provided by Siemens Healthineers, USA [225]. With Flash3D, the SPECT image reconstructions can be performed very fast, well within clinically acceptable time. However, to compensate for faster computation time, approximations in the distance-dependent collimator detector response modeling have been made.

In order to assess the influence of these approximations on the activity quantification of the reconstructed images, a study comparing the quantification performance of Flash3D and in-house developed reconstructed images is deemed necessary. Although some authors focus on the ^{177}Lu activity quantification with Flash3D reconstruction software [142,226], to the best of our knowledge there is no direct comparison of ^{177}Lu images reconstructed with Flash3D and in-house developed software. Additionally, when the Flash3D reconstruction was introduced, its main application was quantitative ^{99m}Tc myocardial perfusion studies [210,227]. Given the fact that ^{177}Lu energy spectrum is quite different from ^{99m}Tc, the ^{177}Lu activity quantification in Flash3D reconstructed images needs to be investigated.

Therefore, the purpose of the current study is to evaluate the quantification performance of ^{177}Lu using Flash3D reconstructed images, under clinically relevant settings and conditions. A series of phantom experiments with different attenuation and scatter medium have been performed. The reconstructions performed using both Flash3D and our in-house developed algorithm (referred as MIRG, which has been extensively tested by Uribe et al. in quantitative ^{177}Lu phantom studies [218]) were compared.

4.2 Methods

This study was composed of two parts:

1) Comparison of ^{177}Lu activity quantification from both Flash3D and MIRG reconstructed SPECT images, using phantom experimental data.
2) Comparison of mean kidney dose calculated based on Flash3D and MIRG reconstructed SPECT images, for five NET patients undergoing ^{177}Lu DOTATATE radionuclide therapy.

4.2.1 Phantom experiments

To compare the quantitative accuracy of Flash3D and MIRG reconstructed images in different attenuation and scatter conditions, a series of phantom experiments were performed:

A. Sphere sources in air: Three source inserts (Table 4.1) were placed in an empty phantom, to evaluate the quantification accuracy of reconstruction algorithms when there is minimal amount of attenuation and scattering medium.
B. Sphere sources in non-radioactive water: Same source inserts were placed in a phantom filled with non-radioactive water, to evaluate the quantification accuracy of the reconstruction algorithms when there is attenuation and scattering medium.
C. Sphere sources in radioactive water: Same source inserts were placed in a phantom filled with radioactive water, to evaluate the quantification accuracy of reconstruction algorithms using different segmentation methods.

Same cylindrical Jaszczak phantom containing three spherical inserts filled with ^{177}Lu activity was used for all experimental scans. The information about sizes and activities of the source inserts and the phantom background for each experimental configuration is presented in Table 4.1.

Table 4.1 The sizes and activities of three source inserts and phantom background for each phantom configuration.

	Source inserts (S1, S2 and S3)			**Phantom background**	
Phantom Configuration	**A, B and C**			**A and B**	**C**
	S1	S2	S3		
Size [mL]	113.1	15.9	8.1	7290	7290
Activity [MBq]	233.0	32.3	16.4	0	2188

As shown in the Table 4.1, the activity concentration of the spherical sources was about 2 MBq/mL. For configuration C, the activity concentration of the radioactive water background was about 0.3 MBq/mL. The activity concentration ratio in spherical sources to that in the radioactive water background was about 6.5, which is close to that observed in a typical SPECT image of NET patient treated with ^{177}Lu DOTATATE. The sources and background activities reported here were measured at the beginning of the experiments. All the phantom scans were performed within five hours. For this duration, the amount of ^{177}Lu that decayed was less than 2.5%.

4.2.1.1 Data acquisition and reconstruction

All the phantom experiments were performed using Siemens Symbia SPECT/CT camera, at the Nuclear Medicine department, Vancouver General Hospital, Vancouver, BC, Canada. For each SPECT scan, the projection images were acquired at 90 angular views, using 128 by 128 matrix. The medium energy low penetration collimator (MELP) was used to image the 208 keV photopeak. In order to investigate the influence of the LSW/USW window width on the activity quantification, the SPECT acquisitions were performed with two settings of scatter energy windows, namely narrow scatter windows (NS) and wide scatter windows (WS). The SPECT scans of phantom configuration B and C were performed with both NS and WS, while scans of phantom configuration A were only performed with WS. The lower and upper limits of these energy window settings are provided in Table 4.2.

Table 4.2 Lower and upper limits of energy window settings used for SPECT scans in phantom experiments. The window width, expressed as percentage of 208 keV photopeak, is provided in brackets.

Energy window setting	LSW [keV]	PW [keV]	USW [keV]
NS	176.8-187.2 (5%)	187.2-228.8 (20%)	228.8-239.2 (5%)
WS	145.6-187.2 (20%)	187.2-228.8 (20%)	228.8-270.4 (20%)

The projection durations, energy window settings in each phantom configuration are provided in Table 4.3.

Table 4.3 The energy window settings, projection durations used in phantom experiments.

Phantom Configuration	Energy windows settings	Projection duration [s]
A	WS	20
B	WS and NS	40
C	WS and NS	40

For all SPECT projection data, the images were reconstructed with two methods: Flash3D and MIRG. They are both OSEM based reconstruction methods with triple energy window (TEW) based scatter correction [222], CT based attenuation correction and 3D camera resolution recovery (RR) enabled. For both reconstructions, the images were stored in 128 by 128 by 128 matrices, with 4.79 mm cubic voxel. The reconstruction parameters were set as 10 subsets and 6 iterations. Image post-filtering was disabled.

4.2.1.2 System calibration

Appling the conclusions of Chapter 3, the Symbia SPECT/CT camera was calibrated using planar scan of a point-like source placed in air, with both NS and WS energy window settings. The scan duration was 10 mins and the activity of the source was equal to 15 MBq. For each energy window setting, the TEW method was used to calculate the number of primary

photons in the entire FOV of the planar images. Then the camera calibration factor was calculated as the total number of primary counts in the entire FOV divided by the product of source activity and scan duration. To convert the voxel values into absolute activities, the calibration factor corresponding to the NS or WS window setting was applied to the SPECT images reconstructed (by either Flash3D or MIRG) from the data with the same energy window setting.

The background counts, which was measured by a 5 mins planar scan (with WS energy window setting) when there was no radioactive source exists, was removed from the total counts of the planar calibration scans.

4.2.2 NET patient study

Five patient datasets were acquired using Siemens Symbia SPECT/CT camera with MELP collimator, at the Department of Radiology and Nuclear Medicine, CHU de Québec—Université Laval, Quebec, Canada. In order to calculate the kidney dosimetry, three SPECT/CT scans were performed for each patient, at approximately 4 hours, 23 hours and 70 hours after the radiopharmaceutical injection. The projection images were stored in 128 by 128 matrix, with 96 views. The scan duration per projection was 15s for measurements performed at 4 hours and 23 hours, 20s for the measurements at 70 hours. The details of the energy window settings for the patient acquisitions are provided in Table 4.4.

Table 4.4 Lower and upper limits of energy window settings used for SPECT scans in patient study. The window width, evaluated as a percentage of 208 keV photopeak, is provided in brackets.

	LSW	PW	USW
Lower and upper limit [keV]	166.4-187.2 (10%)	187.2-228.8 (20%)	228.8-249.6 (10%)

The acquired SPECT projection data were reconstructed the same way as the phantom experimental data, except for that 8 subsets and 4 iterations were selected as the reconstruction parameters.

4.2.3 Data analysis

4.2.3.1 Phantom data

In order to assess the quantitative accuracy of the reconstructed images, the spherical sources had to be segmented. Depending on the phantom configuration, different segmentation method was applied to the SPECT images, reconstructed by either commercial Flash3D or in-house MIRG algorithm:

- For configuration A (Spheres in air): a large 3D VOI manually drawn around the desired sphere was used to segment the source.
- For configuration B (Spheres in non-radioactive water): a large 3D VOI manually drawn around the desired sphere was used to segment the source.

- For configuration C (Spheres in radioactive water): the source was segmented using the following three methods:
    - Fixed threshold of 40%: First a large 3D VOI around the desired sphere was manually drawn. Then a fixed threshold of 40% was applied to the data inside this large VOI to segment the source. The threshold was calculated based on the mean of the 9 voxels containing highest activities within the large VOI. This method was tested because it has been widely used for organ or tumour segmentation in clinical studies [228].
    - Manually drawn VOIs based on the true volume of the spheres determined from CT images. This method exploits the fact that the CT images are co-registered with SPECT images when the data is acquired with a hybrid SPECT/CT camera. However, this method tends to underestimate the source activity as it does not consider the activity 'spill out' caused by PVE (discussed in Section 2.2.2.6).
    - The iterative adaptive thresholding (IAT) method developed by our former group member Grimes et al. [229]. This method is expected to have the best performance in terms of activity quantification, as it should account for PVE. The threshold of the segmentation applied to SPECT images was iteratively determined from the calibration curve, which was obtained from a series of phantom experiments with activity distributions that had a wide range of source to background ratios (SBR) [218].

Once the activity of the sphere source was determined using the segmentation methods listed above, the quantification performance of the reconstruction algorithm was evaluated in the following three aspects:

- The activity recovery coefficient (RC) of each spherical source, calculated using either Flash3D or MIRG reconstructed images, were compared. The activity RC was defined as:

$$RC = \frac{A_{SPECT}}{A_{measured}} \tag{4.1}$$

Where: A_{SPECT} is the activity of the spherical source calculated from the reconstructed SPECT image, while $A_{measured}$ is the decay corrected activity of the same source measured by the dose calibrator.

- The voxel values of the slice in the reconstructed images (from both Flash3D and MIRG method) passing through the centers of all three sphere sources, was compared.
- Coefficients of variation (CV) for all the voxels inside the physical boundary (evaluated for both Flash3D and MIRG reconstructions, using CT images) of each source was calculated and compared. The CV was defined as:

$$CV = \frac{\sigma}{\mu} \tag{4.2}$$

Where: σ and μ stand for the standard deviation and mean value of the voxels inside each spherical source, respectively.

The activity RC was evaluated because it relates to the accuracy of quantification of organ activity. It can be used to estimate the mean organ dose. The activity distribution and CV were investigated as they directly relate to the activity values in each voxel. They can be used to calculate the dose distribution.

4.2.3.2 Patient data

For each patient, the activity of the kidney at each time point was determined from the corresponding SPECT images (reconstructed by either Flash3D or MIRG) using the iterative thresholding segmentation method [229], while the anatomical volume of the kidney was determined from the manual segmentation of the CT images acquired at 4 hours post injection. The time-activity curves were modeled as two segments trapezoidal function (zero to the first data point and the first data point to the second data point), followed by the monoexponential curve passing through second and third data points. The time integrated activity, defined as the area under the time-activity curve, was multiplied by the kidney S value to get the mean dose. Here, the standard OLINDA kidney S value (0.289 mGy/(MBq·h) for 299 g mass) was used and rescaled for each patient's kidney mass to account for the anatomical differences between the current patient and the OLINDA's 'average' human phantom [158].

Once the doses were calculated from the images reconstructed by both Flash3D algorithm ($D_{Flash3D}$) and MIRG algorithm (D_{MIRG}), the percentage difference (ΔD) in dose estimate was evaluated using the following equation:

$$\Delta D = \frac{D_{Flash3D} - D_{MIRG}}{(D_{Flash3D} + D_{MIRG})/2} \times 100\% \quad (4.3)$$

4.3 Results

4.3.1 Phantom experiments

The camera calibration factors determined from the planar scans, for both WS and NS energy window settings, are compared in Table 4.5.

Table 4.5 Summary of camera calibration factors for both WS and NS energy window settings.

	WS	**NS**
System calibration factor [cps/MBq] (Average value of two camera heads)	8.9	8.8

The comparison of the activity RC for all spherical sources calculated from both reconstructions (Flash3D and MIRG) is presented in Figure 4.1, for two energy window settings (WS and NS) and three phantom configurations (A, B and C). Depending on the phantom configuration, the activity RC was calculated using different segmentation method.

Figure 4.2 compares the activity distribution obtained from both Flash3D and MIRG reconstructed images, for all three phantom configurations. The comparison was performed on the slice passing through the centers of all three sources. The images reconstructed from the data

acquired with WS are presented in Figure 4.2a, while the images reconstructed from the data acquired with NS are presented in Figure 4.2b.

The comparison of CV for all the voxels inside the spherical sources is presented in Figure 4.3. For each sphere, the CVs, calculated based on both MIRG and Flash3D reconstructed images, are compared, for all phantom configuration (A, B and C) and both energy window settings (WS and NS).

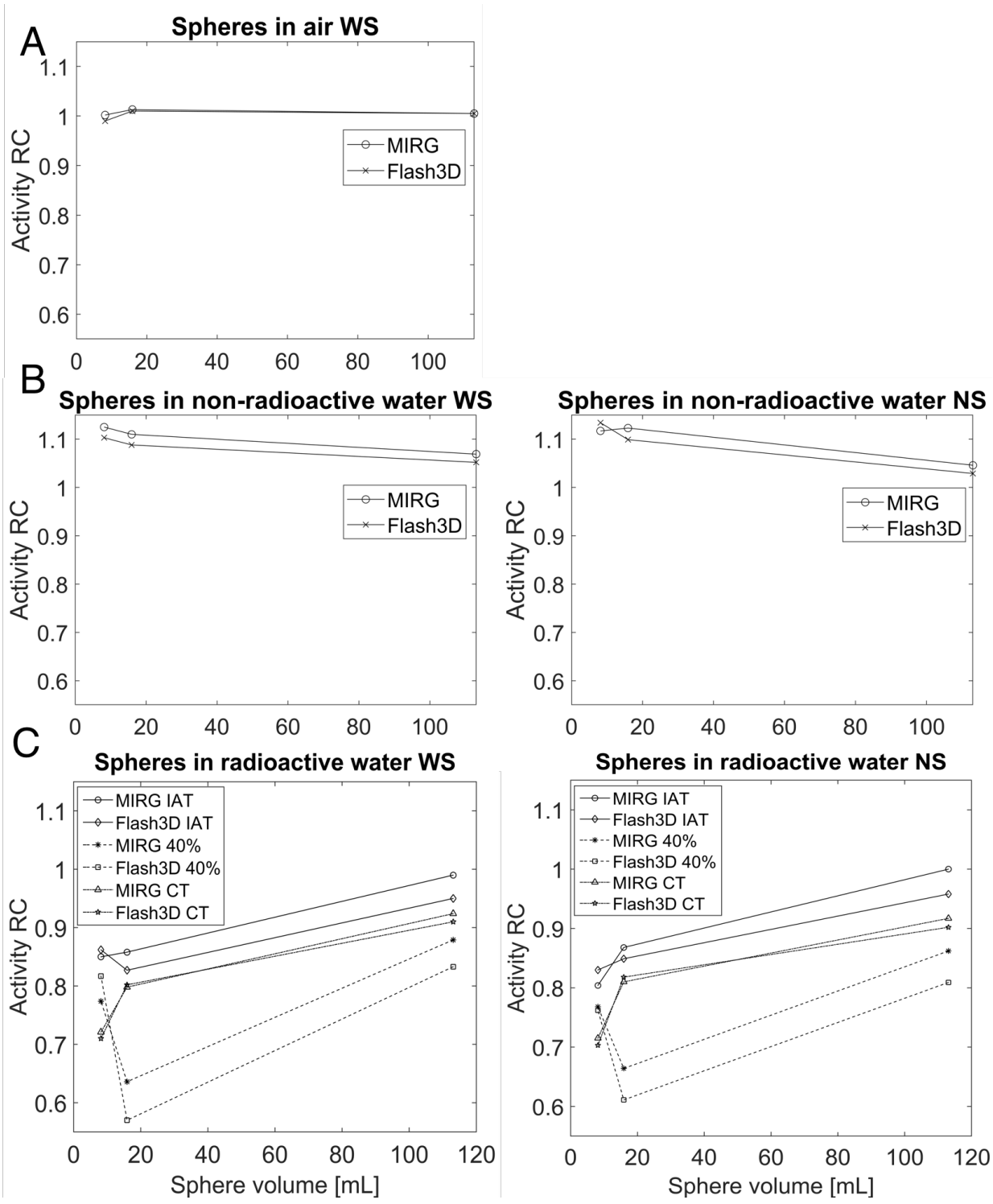

Figure 4.1 Comparison of activity RC calculated from both reconstructions. The phantom configuration A is presented in the first row, while the phantom configuration B and C are

shown in the second and third row, respectively. There were two energy window settings: WS (first column) and NS (second column). For phantom configuration A and B where there was no activity in the background, a manually drawn large VOI around each sphere source was employed. For phantom configuration C where the sources were placed in the radioactive background, the performance of three segmentation methods was compared: iterative adaptive thresholding (IAT), 40% fixed threshold (40%) and CT volume (CT).

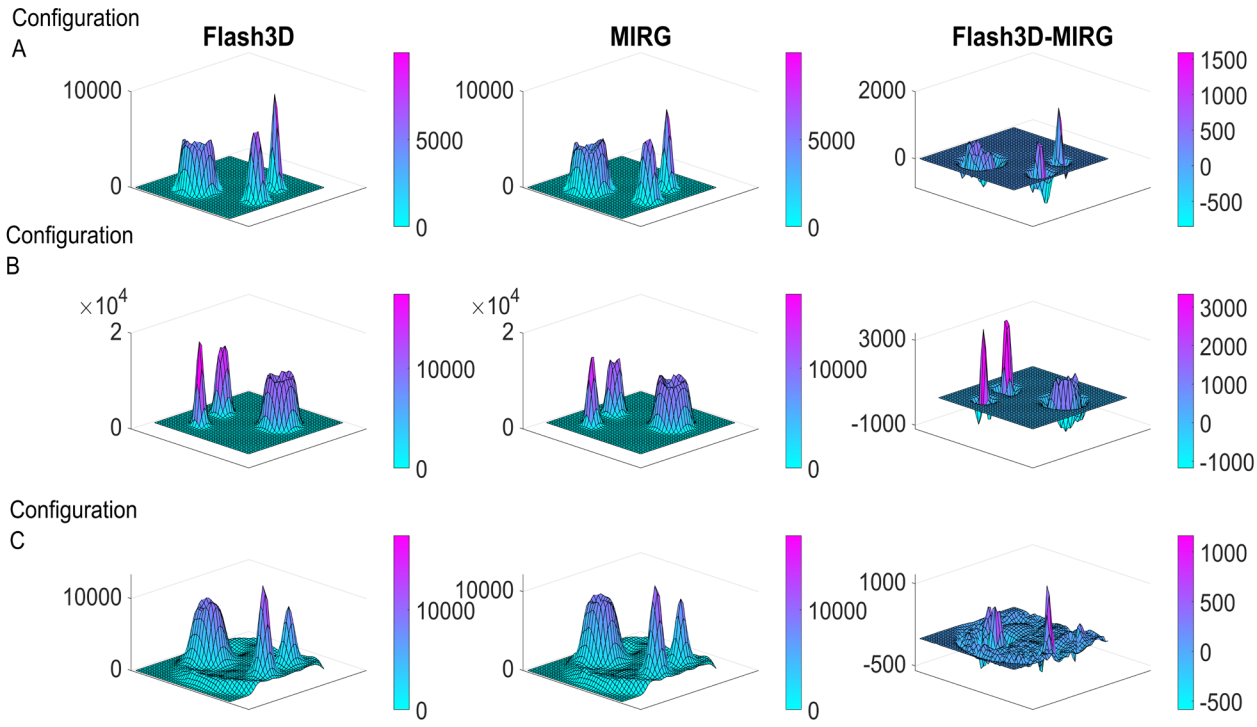

Figure 4.2a Comparison of activity distributions in the slice passing through the centers of all spherical sources, for the phantom configuration A (first row), configuration B (second row) and configuration C (third row). The presented slices correspond to the images reconstructed from projection data with WS energy window setting.

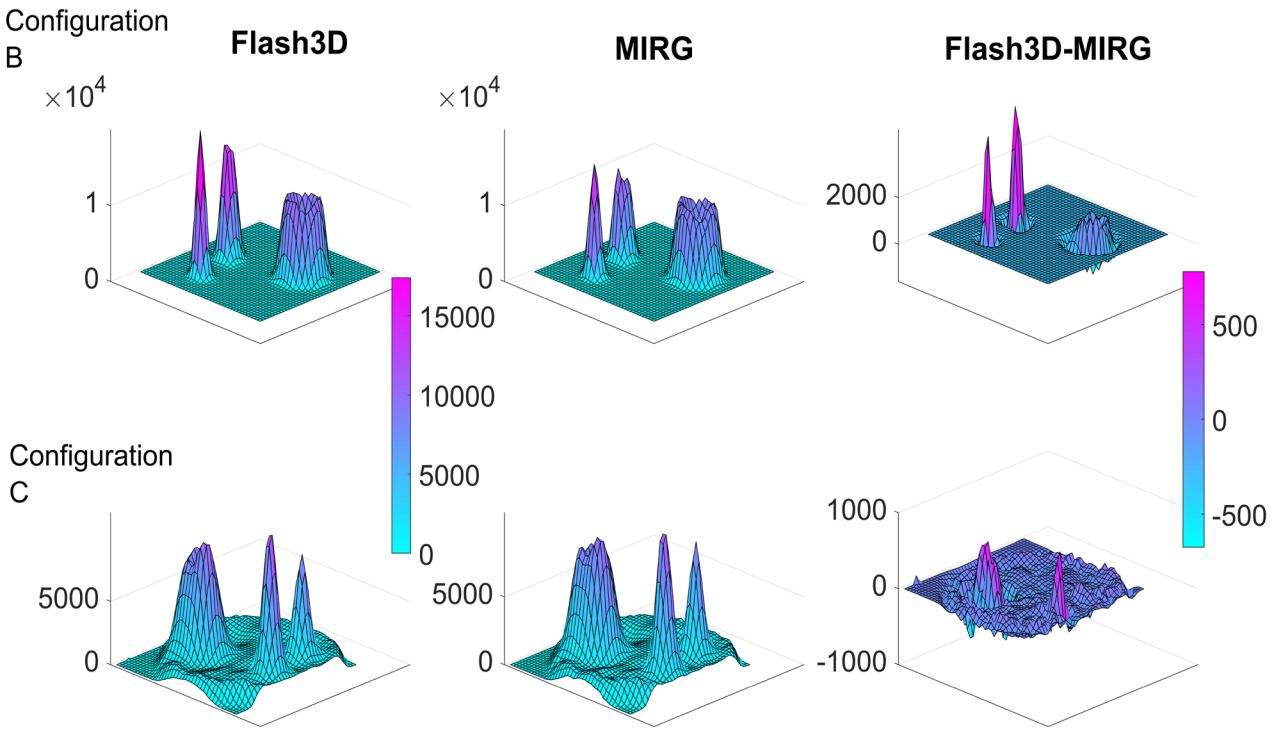

Figure 4.2b Comparison of activity distributions in the slice passing through the centers of all spherical sources, for the phantom configuration B (first row) and configuration C (second row). The presented slices correspond to the images reconstructed from projection data with NS energy window setting.

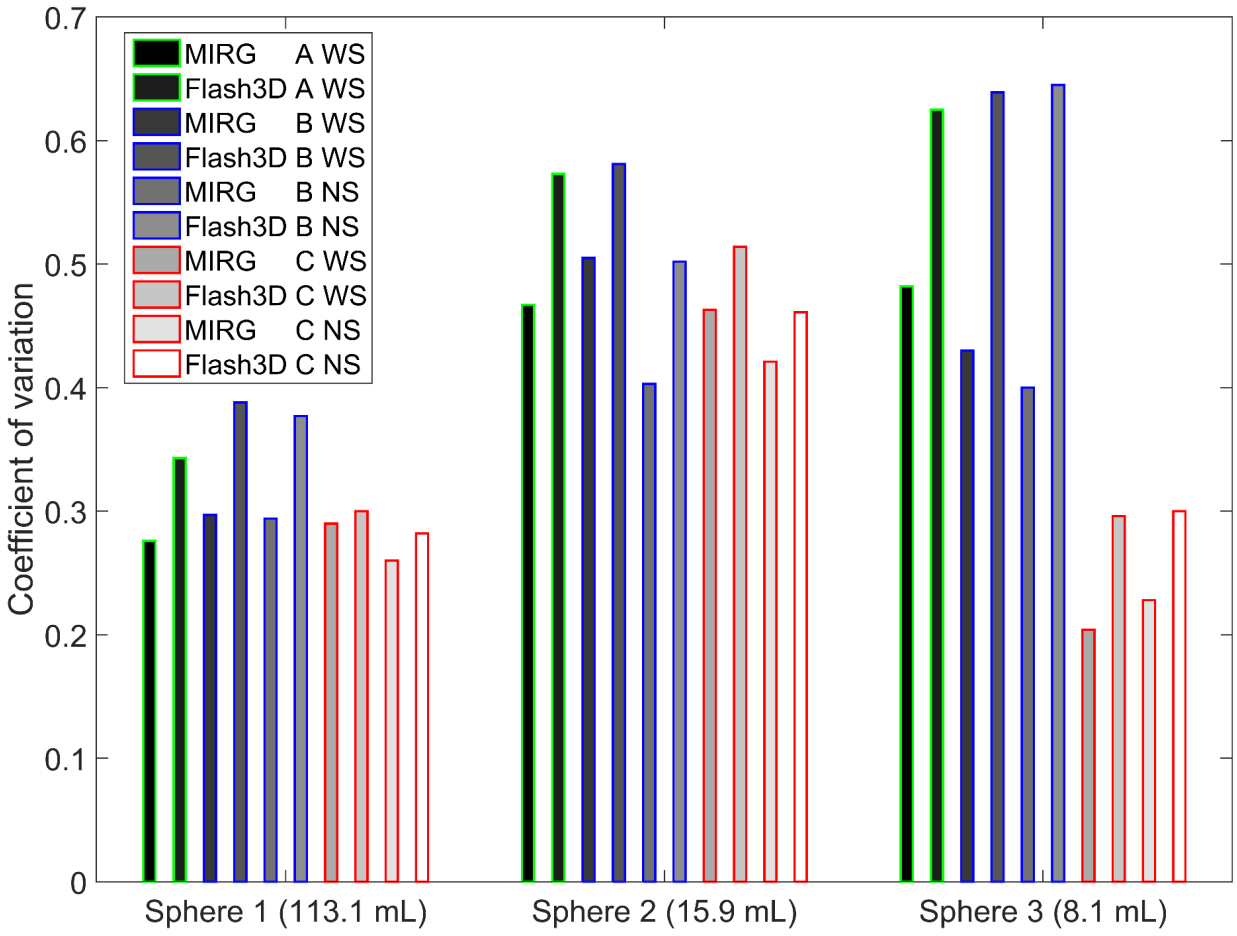

Figure 4.3 Comparison of CV for the voxels inside each spherical source, calculated based on both MIRG and Flash3D reconstructed images. The bars with green edges stand for the phantom configuration A. The bars with blue edges stand for the phantom configuration B. The bars with red edges stand for the phantom configuration C. For any given phantom configuration (second word of the legend) and energy window setting (third word of the legend), the left bar shows the CV obtained from MIRG while the right bar shows the CV obtained from Flash3D.

4.3.2 Patient study

The kidney doses estimated based on the images reconstructed using both Flash3D and MIRG algorithm are summarized in Table 4.6. In order to investigate the influence of the reconstruction method on the calculated kidney doses, the percentage difference between the two dose estimates (defined by Equation 4.3) is also provided in the table.

Table 4.6 Summary of kidney doses obtained from both Flash3D and MIRG reconstructed images. For comparison purposes, the percentage difference between the two kidney dose estimates is also included in the table.

Patient #	**Left kidney dose [mGy]**			**Right kidney dose [mGy]**		
	MIRG	Flash3D	Difference [%]	MIRG	Flash3D	Difference [%]
1	3338	3151	-5.8	4502	4129	-8.7
2	3924	3733	-5.0	4401	4154	-5.8
3	3590	3525	-1.8	3508	3367	-4.1
4	4755	4422	-7.3	2949	3150	6.6
5	3661	3287	-10.8	3602	3237	-10.7
Average	3853	3624	-6.1	3792	3608	-4.5

4.4 Discussion

Different widths of LSW/USW were used in the patient scans (10% windows) and phantom experiments (20% windows). This was because the patient data were acquired by the collaborators in Quebec City, while the phantom data were acquired by me in Vancouver. To investigate this issue, the influence of LSW/USW width on activity quantification was investigated by using WS (20%) and NS (5%) windows. Although the width of the scatter photon windows (LSW or USW) in WS and NS energy window settings differs by 15%, the system calibration factor only differs by 1.1% (Table 4.5). This means that the scatter estimated by TEW method mainly depends on the photon counts in PW and not on the width of the scatter window.

The activity RC calculated based on the MIRG and Flash3D reconstructed images is almost the same for phantom configuration A, both of them are very close to 1 for all three spherical sources (Figure 4.1A). This result confirms that the activity quantification performance of these two reconstruction methods is the same when minimal photon attenuation and scattering exists.

The difference of activity RC increased (up to 3%) for the phantom configuration B (Figure 4.1B), where the activity quantification becomes more challenging due to the presence of photon attenuation and scattering. Both the MIRG and Flash3D reconstructed images overestimate the activity in the spheres by about 5% to 12%, depending on the volume of the sources. This is because the TEW fails to model the scattered photons within the sources when they are placed in the non-radioactive water background. This finding agrees with the conclusions of Chapter 3.

The situation becomes more complex for phantom configuration C. Due to the presence of the activity in background, the manually drawn large VOI around the sphere will certainly overestimate the source activity. Therefore, three segmentation methods were evaluated for the source activity quantification in this situation. The activity RCs obtained from both Flash3D and MIRG reconstructed images were very similar (difference was less than 2%) when CT volume was used for the source segmentation (Figure 4.1C). The RC increased as the volume of the source increased, with more than 90% of the source activity recovered for the largest sphere (113 mL). Unlike the CT based segmentation, the threshold-based methods (IAT and 40% fixed threshold) tend to result in larger differences in activity RCs: The MIRG reconstructed images recovered source activity up to 5% higher than the Flash3D reconstructed images. The performance of IAT method was the best as it accounts for the source activity 'spill out' by PVE. In particular, at least 95% activity recovery for the largest sphere was achieved, which is quite impressive. The lowest activity RC for two largest spheres was obtained from the 40% fixed threshold, which suggests this method may not be a good candidate for the segmentation of source activity. Similar activity recovery was obtained when the energy window setting was changed from WS (first column of Figure 4.1) to NS (second column of Figure 4.1). This confirms that the activity quantification mainly depends on the photon counts in PW when TEW was applied for scatter correction.

Small differences in activity distribution are observed between the Flash3D and MIRG reconstructed images (Figure 4.2a and Figure 4.2b). Compared with the MIRG reconstructions, the sphere activity concentration obtained from Flash3D reconstructions was a little bit higher in the center and a little bit lower at the sphere boundary (phantom configuration A and B). This difference became even less pronounced when there was activity in the background (phantom

configuration C, which had similar activity distribution to those usually observed in clinical studies).

The analysis of the results presented in Figure 4.3 indicates that the CV is lower in MIRG reconstructed images, for all sphere sources and phantom configurations. In other words, the variation of the voxel counts inside each sphere is smaller for MIRG reconstructions than for Flash3D reconstructions. This means the MIRG reconstruction better represents the activity distribution since the spheres were filled with uniform activity concentration. Similar activity distributions were obtained when the energy window setting was changed from WS to NS.

The results of the patient study showed that similar radiation doses to kidneys were obtained from MIRG and Flash3D reconstructed images. The average differences in mean dose were -6.1% and -4.5% for left kidney and right kidney, respectively (Table 4.6). This result was close to the difference in activity quantification for phantom configuration C when using IAT segmentation.

4.5 Conclusions

In this chapter, activity quantification performance of Flash3D reconstruction software was evaluated. This was done by comparing the activity quantification and activity distribution in the spherical sources obtained from the Flash3D reconstructions to those from MIRG reconstructions. Three phantom configurations with different photon attenuation and scattering conditions, as well as two scatter window settings were employed. Since the activity

quantification will eventually be used for dosimetry, the kidney doses calculated based on MIRG and Flash3D reconstructed patient images were also compared.

Activity recovery from MIRG and Flash3D reconstructions agreed to within 5% for all phantom configurations, meaning Flash3D reconstructions were accurate enough for organ level dosimetry. For the phantom configuration C, which had activity distribution most similar to those observed in clinical studies, at least 90% activity recovery was achieved for the largest sphere (113 mL) when CT volume was used for segmentation. The activity RC for the largest sphere was even higher (at least 95%) when IAT segmentation was applied. The mean kidney dose calculated from Flash3D reconstructions was similar (on average the percentage difference was around 5%) to those calculated from MIRG reconstructions. However, activity distribution from Flash3D was slightly different from MIRG reconstructions for the acquisitions with no background activity. This activity distribution difference was less noticeable for the phantom configuration C. The reconstructed images from Flash3D were noisier than those from MIRG. Thus, we recommend applying post filtering when estimating activity distribution from Flash3D reconstructions. Another conclusion from this study is that when using TEW scatter correction, the width of the scatter windows (5%-20% of 208 keV photopeak) does not affect activity quantification.

Chapter 5: Image-based dosimetry for the NET patients undergoing ^{177}Lu DOTATATE radionuclide therapy

5.1 Introduction

Medical use of radiation aims to provide therapeutic benefit to patients, but inevitably brings risk to the critical organ dues to potential radiation exposure. In conventional external beam radiation therapy, radiation dose has been widely recognized as an important quantity for the prediction of tumour control and normal tissue toxicity. Many guidelines have been published, aiming to limit normal tissue toxicity [230] and to achieve high tumour control [231,232]. These recommendations on radiation dose are usually based on previous clinical experience. In general, the outcome of a fractionated course of radiation therapy is determined by the well-known 4 R's rule [233]:

1) Repair of DNA damage
2) Redistribution of cell cycles
3) Repopulation
4) Reoxygenation

Additionally, the dose rate may have a significant impact on the tumour response to radiation [234]. A clinical study on prostate cancer by Brenner et al. showed that large dose per fraction/dose rate resulted in an improved tumour control in the brachytherapy and external beam radiotherapy [235]. The most commonly used model in the field of external beam radiotherapy, which describes the dose fractionation and protraction effects on the therapeutic response, is the

linear quadratic formalism [236–238]. However, the extrapolation of radiobiology from traditional external beam therapy to radionuclide therapy may not be straightforward, because the dose delivery schemes are very different in these two radiotherapies [239]. Contrary to the external beam radiation therapy, in radionuclide therapy the dose is usually delivered over a long period of time and at a relatively low rate. As a result, the well-established linear quadratic model might not be suitable (or at least its validity needs to be confirmed) to predict the treatment response in radionuclide therapy due to its inaccuracy in the small dose range [237].

As described, radiation dose estimation is not routinely performed in ^{177}Lu DOTATATE radionuclide therapy. As a result, fixed amount of radiopharmaceutical is currently used at the cost of underdosing or overdosing some patients. In order to improve the treatment efficacy, establish the model for the tumour control and safety profile predication, a solid dosimetry approach needs to be developed and applied to the ^{177}Lu DOTATATE clinical studies.

As discussed in Chapter 2, the first step of the image-based dose estimation involves a series of quantitative imaging studies. Some of the problems related to the quantification of ^{177}Lu SPECT images under clinically relevant conditions were discussed in Chapter 3 and Chapter 4. Additionally, bremsstrahlung photons generated by beta particles might also be detected by the gamma camera. Luckily, this is not a concern because for ^{177}Lu bremsstrahlung yield is very low and contributes mostly to the counts of low energy background of the spectrum [220]. Other questions, such as the influence of the camera dead-time on the dose calculation results, remain to be answered.

Once the quantitative data points are obtained, according to equation 2.4, the time-integrated activity, as well as the S factor (Section 2.2.3.2), need to be determined for the dose

estimation. These steps involve: accurate modelling of the time-activity curve and appropriate selection of the S factor.

The aim of this study was to propose an accurate image-based dosimetry protocol using multiple quantitative SPECT/CT acquisitions, for the optimization of ^{177}Lu DOTATATE radionuclide therapy. The effect of the camera dead-time on the radiation dose estimate was also investigated. Different time-activity curve integration methods were compared. The patient data acquisitions schedules were carefully selected, taking into account the requirements of accurate time-activity curve measurement and the constraints of clinical resources.

5.2 Methods

5.2.1 Patient characteristics and radionuclide therapy

Thirty-nine patients diagnosed with progressive metastatic and/or symptomatic NET were treated with fifty-three cycles of ^{177}Lu DOTATATE radionuclide therapy, at the Division of Nuclear Medicine, CHU de Québec—Université Laval. The patient inclusion criterion was: demonstrated overexpression of SSTR in tumours by Octreoscan or ^{68}Ga PET scan. Amino acid solution was administered with radiopharmaceutical to reduce the nephrotoxicity [240]. All the patients were enrolled in the P-PRRT clinical trial (registration No: NCT02754297) and gave informed consent to participate in the study. For each therapy cycle, the injection (median 9.3 GBq, range 4.1-26.1 GBq) was personalized by the physician, based on the patients' kidney function, body habitus and dosimetric results from the previous therapy cycle(s) [241]. The details about the treatment protocol were described in [242]. The patient characteristics are summarized in Table 5.1.

Table 5.1 The characteristics of NET patients included in this study.

All patients (n=39)	
Gender, n (%)	
Male	24 (62)
Female	15 (38)
Age at first therapy cycle, median (range)	62 (26-82)
Weight [kg], median (range)	77 (46-122)
eGFR[1] [mL/min/1.73m^2], median (range)	88 (42-134)
Primary tumour location, n (%)	
Small intestine	13 (33)
Pancreas	10 (26)
Adrenal gland	6 (15)
Lung	3 (8)
Esthesioneuroblastoma	1 (3)
Unknown	6 (15)
Number of therapy cycles analyzed in this study, n (%)	
1	33 (85)
3	4 (10)
4	2 (5)

[1]eGFR: Estimated glomerular filtration rate.

5.2.2 Data acquisition and SPECT quantification

For each treatment cycle, three SPECT/CT scans were performed using Siemens SymbiaT camera (Siemens Healthineers, Germany). The MELP collimator was used in all acquisitions. The first scan (D0) was acquired at about 4.3 hours (range 3.6-5.3 hours) after the ^{177}Lu DOTATATE administration, the second scan (D1) at 22.7 hours (range 19.6-25.0 hours) and the third scan (D3) at 69.8 hours (range 67.2-74.1 hours). Additionally, one patient was scanned two more times at 140.4 hours (D6) and 213.1 hours (D9) post injection.

The projection images were acquired at 96 angular views, with 128 by 128 matrix size. The projection duration was 15 s for the measurements on D0 and D1, 20 s for the measurements on D3 and D6, and 25 s for D9. Two scatter windows (LSW and USW) were used to measure the scatter counts in 208 keV photopeak window (PW). In addition, three other energy windows (OW) were employed to estimate the whole spectrum count rate. The details about the energy window settings are provided in Table 5.2.

Table 5.2 Energy window settings used in SPECT/CT acquisitions. For LSW, PW and USW, the widths of the window (in percentage of 208 keV) are provided in brackets.

Energy windows [keV]	**LSW**	**PW**	**USW**	**Other windows (OW)**
Range	166.4-187.2 (10%)	187.2-228.8 (20%)	228.8-249.6 (10%)	18.5-55.4 55.5-166.4 249.6-680.0

The images were reconstructed with commercial software package Flash3D provided by Siemens (OSEM based algorithm, 8 subsets, 4 iterations, no post filtering). The reconstructed images were stored in 128 by 128 by 128 matrices, with 4.79 mm cubical voxel. CT based attenuation correction, TEW scatter correction and resolution recovery were applied in image reconstruction.

The SPECT/CT imaging system was calibrated using a tomographic scan of a cylindrical phantom (Jaszczak) filled with uniform activity [243]. The acquisition and reconstruction parameters for this calibration scan were the same as those used in patient acquisitions (except for the 10 s projection duration). The calibration factor was calculated as the total counts in the reconstructed image divided by the total activity in phantom, the number of projections and projection duration.

5.2.3 Kidney segmentation

It has been showed that the DOTATATE uptake in kidney is mainly at the outer zone of the medulla and the cortex [240,244]. Moreover, the fact that for our patient data the activity in kidney pelvis could only be observed in the first SPECT scan, indicating that this activity's contribution to the kidney dose was negligible. Considering this, the kidney pelvis was not included in both the volume (mass) and the activity segmentation. For each therapy cycle, the mass (or volume) of left kidney (L-kidney) and right kidney (R-kidney) was determined from a 3D manual segmentation of the kidneys in the CT images acquired on D0.

According to the results of Chapter 4, the IAT segmentation method performs the best (at least 95% activity recovery was achieved for the 113 mL sphere source), followed by the CT image based segmentation method (about 90% activity recovery was achieved for the 113 mL

sphere source). These findings indicate that the IAT segmentation method is an ideal candidate for the determination of activity in large region (>100mL), when: 1) the source has uniform activity concentration and 2) the ratio of activity concentration in the source region and surrounding background (i.e. SBR) is about 6. Please note that these two conditions might not be satisfied for the kidney uptake situations observed in the entire patient population.

Therefore, in order to accurately determine the kidney activity (thus the radiation dose) at each time point, the patients were divided into two groups depending on their activity uptake in the kidneys: A) high uptake and B) low uptake. Figure 5.1 shows the comparison of kidney activities obtained from both: the IAT segmentation method and the CT image guided segmentation method, for the patients from group A (Figure 5.1a) and group B (Figure 5.1b). For the majority of our patients (group A), the kidney activity estimated based on IAT segmentation method was larger than that obtained from the CT guided segmentation (Figure 5.1a). For the patients in this group, the IAT segmentation method was applied to determine kidney activity, as this method accounts for the activity 'spill out' effect. For the patients in group B, the IAT segmentation method underestimated the kidney activity due to their low SBR (Figure 5.1b). In this case, the CT image guided segmentation was applied to determine the kidney activity.

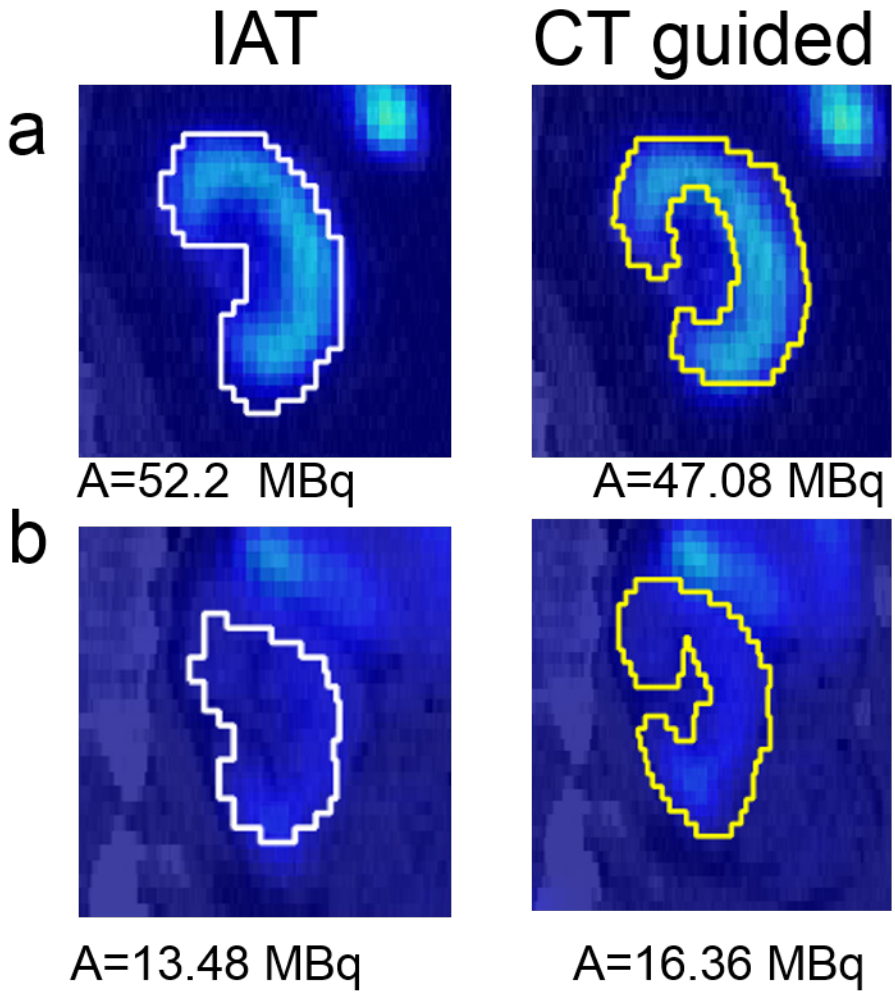

Figure 5.1 Examples of the L-kidney activity obtained from the IAT segmentation (white boundary lines) and CT guided segmentation (yellow boundary lines). The corresponding segmented kidney activity (A) is provided under each image. Here the SPECT and CT fused views are shown. The figure shows two patients which represent two possible situations of kidney uptakes observed in the entire population: a) high uptake (group A) and b) low uptake (group B).

5.2.4 Time activity curve creation

For each therapy cycle, the kidney activities (at D0, D1 and D3 scanning time points), determined from the segmentations of images (described in Section 5.2.3), were used to establish the time activity curves (TACs).

Several studies have shown that the elimination of DOTATATE from the kidneys could be described by exponential functions [7,203,245,246]. Alternatively, the trapezoid functions have been successfully employed in many clinical studies [247,248]. Since there is no information about TACs shape for the time interval between the therapy administration and the first scan (D0) and for the time beyond the last scan (D3), some assumptions about this behavior have to be made. Based on these considerations, four different methods of kidney TACs creation were investigated (Figure 5.2).

- M1: Trapezoid function from the administration time to D0 and from D0 to D1 (two segments) followed by the monoexponential curve obtained from fitting to two (D1 and D3) data points.
- M2: Monoexponential curve obtained from fitting to all three (D0, D1 and D3) data points.
- M3: Trapezoidal function from the administration time to D0, from D0 to D1 and from D1 to D2 (three segments) followed by monoexponential curve fit to D1 and D3 data points.
- M4: Trapezoidal function from the administration time to D0, from D0 to D1 and from D1 to D2 (three segments) followed by monoexponential curve fit to all three (D0, D1 and D3) data points.

Additionally, in order to investigate the influence of camera dead-time effect on the estimated kidney doses, the dead-time corrected kidney activity data points were used to create the TACs based on M1. This method was referred as M1 DT.

The dead-time correction factor, estimated from our previous phantom study [141], was applied to the reconstructed images to recover counts loss due to camera dead-time. For each SPECT scan, the average full spectrum count rate (sum of LSW, PW, USW and OW) was used for the determination of the dead-time correction factor. Although the width of LSW and USW in our dead-time phantom scans were different from those used in the current patient study, the dead-time correction factor determined in [141] should be applicable to the patient scans. This is because: 1) the width of LSW and USW doesn't affect the activity quantification as long as the PW settings are the same (conclusions of Chapter 4), 2) the photon counts recorded in the whole spectrum, which is directly related to the dead-time correction factor, does not depend on scatter windows settings.

Ideally, to model accurately the shape of the kidney TACs, at least 4-5 data points would be needed, as they would allow one to fit biexponential function modelling both the uptake and the clearance phases of ^{177}Lu DOTATATE. Considering that in our study only three data points were available (except for the one patient study with five measurements), and only one scan was performed on the first day, there was not enough information about the uptake phase to fit a separate function. Therefore, for our first method (M1), the uptake phase was approximated by the two segments of a trapezoidal function, from time zero to D0 and from D0 to D1. This approach was considered the most appropriate taking into account that in many patients the D0 scan might have contributions from both uptake and clearance phases, and that the ^{177}Lu DOTATATE uptake phase in kidney is usually much shorter (<24h) than D1 [245,249]. For the

remaining part of TACs, we used a monoexponential curve obtained from fitting to D1 and D3 data points. This part corresponded to the clearance phase of the TACs.

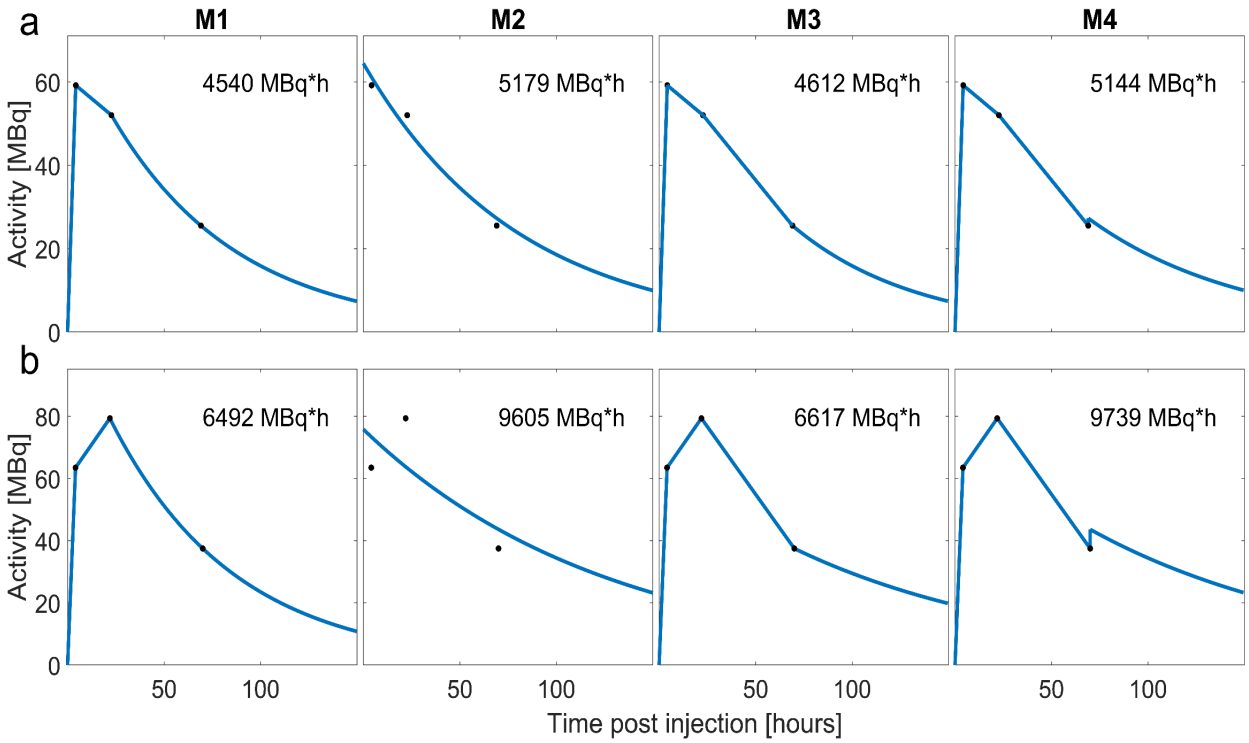

Figure 5.2 The plot illustrating four different time-activity curve creation methods used in this study. For each method, the corresponding time-integrated activity (area under the time-activity curve) is provided. The data presented in Figure 5.2a was from a patient with typical kidney bio-kinetics, while data presented in Figure 5.2b was from a patient with slow kidney uptake (5% of the patients in this study showed this behavior).

The purpose of the M2 was to investigate what would be the effect on the absorbed dose estimate if TACs were created using monoexponential curves (no trapezoids) fit to all three data points. The purpose of M3 (or M4) was to check if the kidney doses would change from those

obtained using M1 (or M2) when three segments trapezoidal functions (zero to D0, D0 to D1 and D1 to D3) were used in TACs creation.

Only one set of patient data with five data points was available in our study. For this patient, the TACs for the left and the right kidneys, obtained using M1 were compared with those obtained from the biexponential curve fit to all five data points.

The exponential curves determined from these fits were subsequently used to obtain the corresponding effective half-lives T_{eff} of the ^{177}Lu DOTATATE elimination from the kidneys. Obviously, the value of T_{eff} depends on the parameters of the curve and its shape. In the four TAC creation methods mentioned above, two curve fitting approaches were used:

- D1+D3: monoexponential fit to D1 and D3 data points. This monoexponential curve corresponds to that used in M1 and M3.
- D0+D1+D3: monoexponential fit to D0, D1 and D3 data points. This monoexponential curve corresponds to that used in M2 and M4.

The T_{eff} obtained from these two curve fitting methods were compared.

5.2.5 Kidney dosimetry

Time-integrated activity (Ã), defined as the area under the TAC integrated from time zero to infinity, was computed for each of the investigated TAC creation methods. Then, for each patient and each therapy cycle, the kidney absorbed dose (D) per unit injected activity (A_0) was calculated using the following formula:

$$\frac{D}{A_0} = \frac{\tilde{A} \cdot S}{A_0} \tag{5.1}$$

Where: S is the kidney dose factor, which equals to OLINDA's value of 0.289 mGy/(MBq·h) for 299 g kidney mass [158]. This factor was rescaled to each particular patient's kidney mass obtained from his/her CT-segmented kidney volumes, using the following equation (assumed kidney density=1 g/cm^3):

$$\frac{S}{0.289\ \mathrm{mGy/(MBq \cdot h)}} = \frac{299\ g}{m_{kidney}} \tag{5.2}$$

5.3 Results

To check if the TACs determined from M1 accurately represents the kidney bio-kinetics, the data from the patient study with five imaging points were analyzed. To this end, the two TACs (for the left and right kidneys) built using M1 were compared with those obtained from the more advanced, biexponential curve fit to all five data points. The results, presented in Figure 5.3, show very little difference between the two curves.

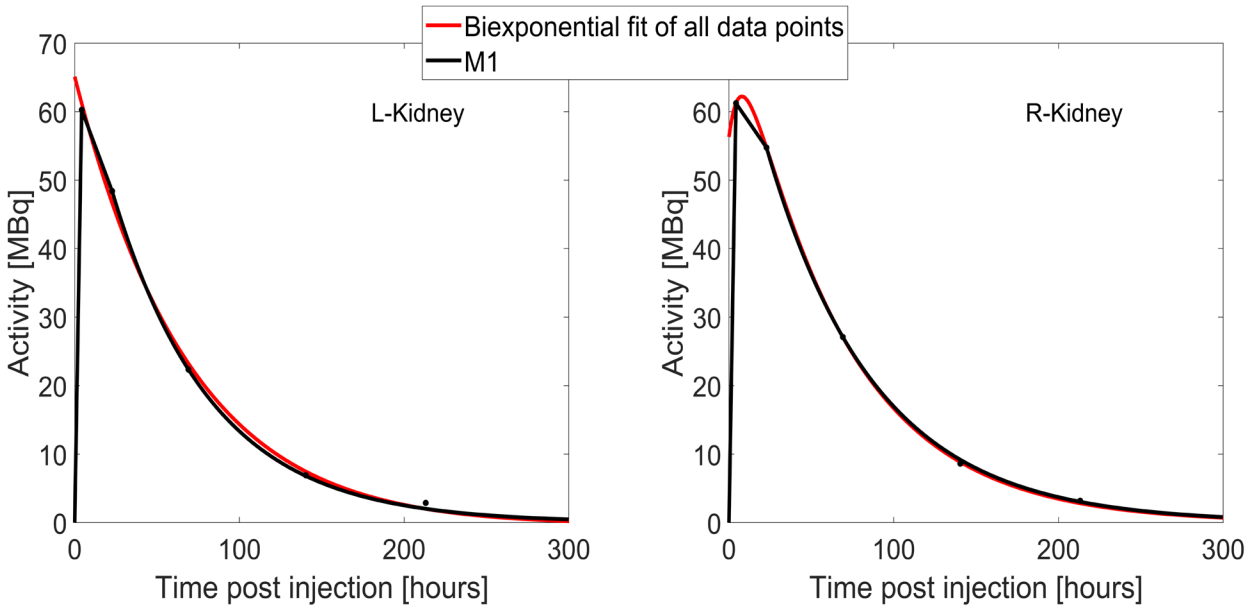

Figure 5.3 A comparison of TACs obtained from biexponential fit of all data points to that obtained from M1 for the patient with five SPECT/CT measurements.

Next, for each patient, the kidney absorbed doses (D) calculated using M1-M4 were compared. The results are presented in Figure 5.4. Please note that, for the box plots presented in this thesis, the central mark indicates the median, and the bottom and top edges of the box represent the interquartile range (25^{th} percentile to 75^{th} percentile). The whiskers extend to the most extreme data points that are not considered outliers, and the outliers are plotted individually using the '+' symbol.

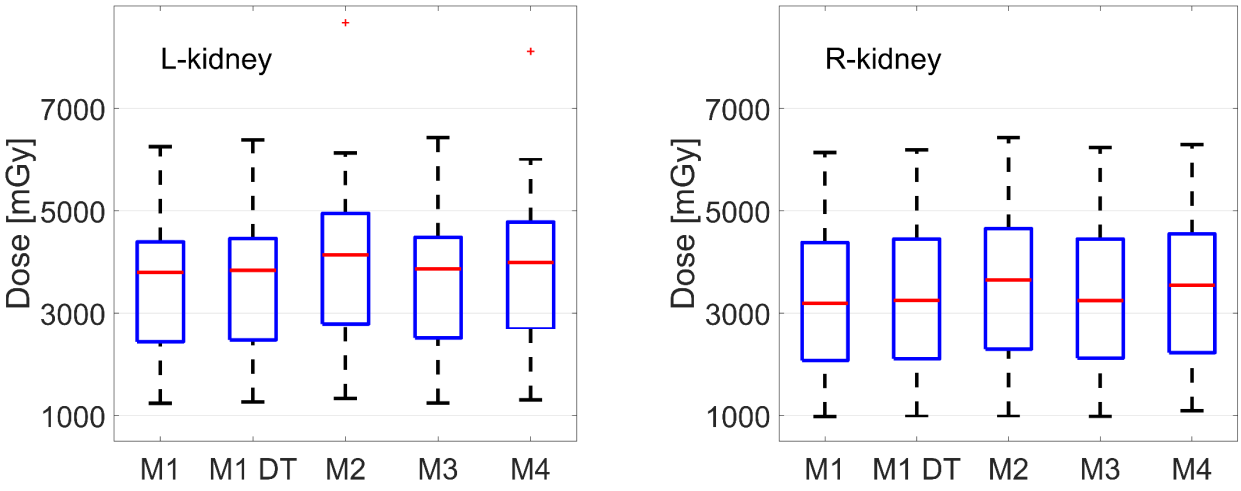

Figure 5.4 Boxplots comparing the patients' kidney doses calculated using different methods (see Section 5.2.4).

The kidney clearance effective half-lives obtained from the D0+D1+D3 method (used in M2 and M4) were compared to those obtained from D1+D3 (used in M1 and M3). The results are presented in Figure 5.5.

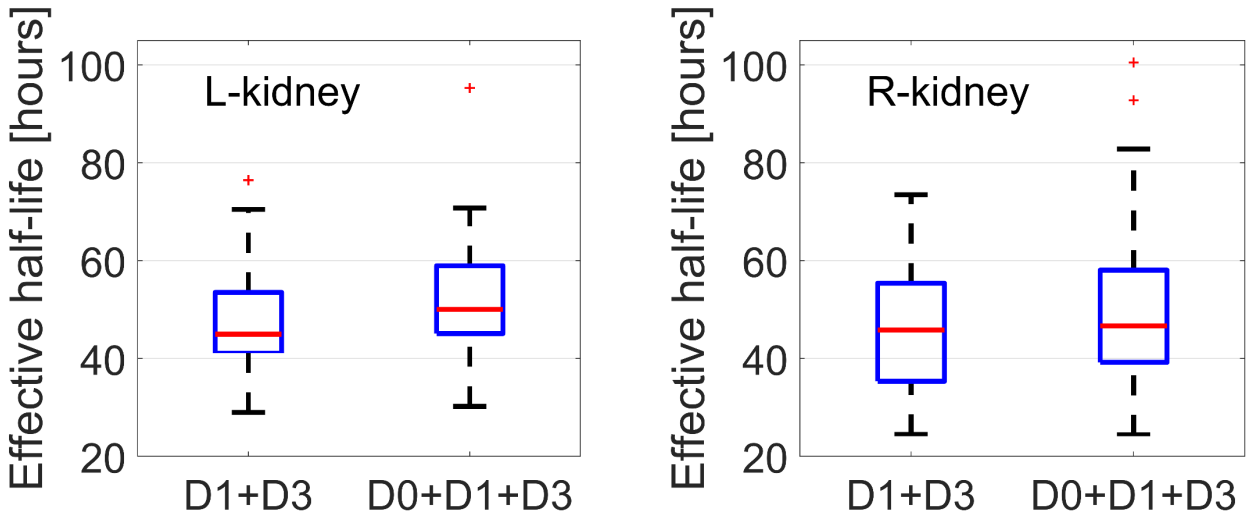

Figure 5.5 Boxplots comparing the kidney effective half-lives obtained from monoexponential fit to D1+D3 data points and D0+D1+D3 data points. The D1+D3 data

points fit method was used in M1 and M3, while the D0+D1+D3 data points fit method was used in M2 and M4.

The results of kidney dose calculation for the entire patient population are summarized in Table 5.3. Here, both the kidney dose (D) and dose per unit administered activity (D/A_0) estimated from method M1 are presented. Five statistical parameters are evaluated in this table: range (minimum - maximum), interdecile range (10^{th} percentile - 90^{th} percentile), median, mean and standard deviation.

Finally, for the patients that had multiple therapy cycles analyzed, the kidney doses per unit injected activity (D/A_0) for each cycle were compared. The results are displayed in Figure 5.6. The first three patients were treated with three therapy cycles while the last two patients were treated with four therapy cycles.

Table 5.3 Summary of the patients' kidney doses (D) and doses per administered activity (D/A_0) obtained from M1. For each quantity, the following statistical parameters estimated from the entire patient population are listed in the table: range (minimum to maximum), interdecile range (10^{th} percentile to 90^{th} percentile), median, mean and standard deviation.

Statistical	**L-kidney**		**R-kidney**	
Parameter	D	D/A_0	D	D/A_0
	[mGy]	[mGy/MBq]	[mGy]	[mGy/MBq]
Range	1239 - 6254	0.135 - 1.276	981 - 6139	0.131 - 0.859
(Minimum - Maximum)				
Interdecile range	1909 - 5197	0.188 - 0.645	1596 - 4825	0.173 - 0.489
(10^{th} percentile - 90^{th} percentile)				
Median	3797	0.404	3195	0.356
Mean	3605	0.409	3258	0.359
Standard deviation	1234	0.205	1278	0.161

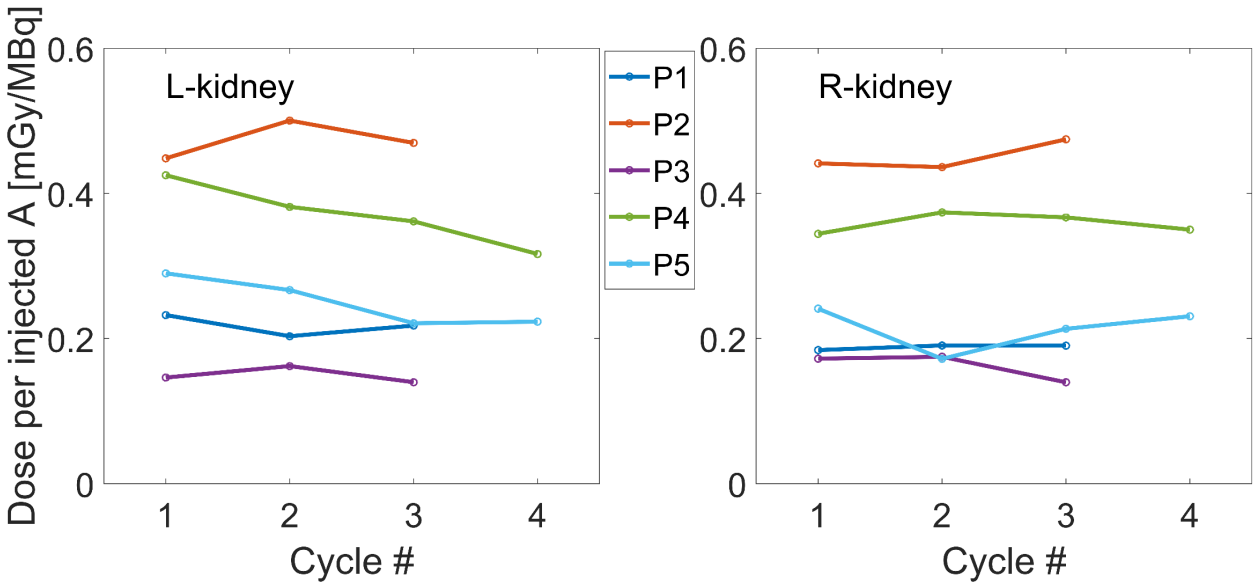

Figure 5.6 Kidney doses per unit injected activity (D/A_0) for the patients with multiple cycles of ^{177}Lu DOTATATE. The results of five patients, with multiple therapy cycles (three or four) analyzed in this chapter, are compared.

5.4 Discussion

The main motivation for the study presented in this chapter was to propose an accurate kidney dose estimation method based on multiple post therapy SPECT/CT images. All the procedures were performed under clinically relevant conditions, such as 1) the SPECT/CT acquisition schedule was carefully selected considering both the patient and NM department burden and 2) patients' images were reconstructed using commercial Flash3D software that comes with the SymbiaT camera. Following the MIRD formalism (equation 2.4 in Chapter 2), all the steps involved in the kidney dose estimation were discussed.

5.4.1 Kidney activity quantification

The results of Chapter 4 confirm that the Flash3D reconstructed images can be used for quantitative measurements of the ^{177}Lu activity within large region (>100mL). However, proper activity segmentation method needs to be applied. Unlike the phantom experiments where the VOI was filled with uniform activity and the SBR was about 6, the kidney activity distributions in the analyzed patient population were more complex. As shown in Figure 5.1, there were two kidney uptake situations. In order to accurately determine the activities in the kidneys, the segmentation method needed to be adjusted accordingly. For the patients with high uptake (Figure 5.1a, SBR of 5 or more; majority of the patients showed this behavior), the IAT segmentation method has been shown to be more accurate than CT image guided segmentation method as it accounts for activity 'spill out' effect. For the patients with low uptake (Figure 5.1b, SBR of 3 or less), the activities in the kidneys were underestimated by the IAT segmentation due to low SBR. In these cases, the CT image guided segmentation was used for the determination of kidney activity.

Although the IAT segmentation method performs better than CT-based segmentation in the kidney activity quantification for majority of the patients, it does require calibration experiments with phantoms containing different activity concentrations and SBRs. This might not be possible for busy NM clinics. Assuming the effect of 'spill out' on kidney activity quantification was approximately the same for the investigated patient population, the following suggestions were made for determination of the kidneys' activity in the clinical studies where the IAT segmentation method was not readily available:

- Use CT image guided segmentation.

- Apply correction factor on the segmented activity to account for the 'spill out' effect. This factor was experimentally determined to range from 1.05 to 1.1 based on our patient data.

The camera dead-time effect results in the loss of counts in the measured projection images, thus might introduce an error in ^{177}Lu activity estimate. In this chapter, the dead-time correction factor determined in [141] was applied to the patient images. For each SPECT/CT acquisition, the primary photon counts loss due to camera dead-time was assumed to be the same for projections acquired at different angular positions. Therefore, the average count rate of all projections was used to estimate the dead-time loss of the reconstructed counts. As suggested in our study, the dead-time correction factor should be analyzed as a function of whole spectrum count rate as this will be less affected by the body size of each particular patient [141]. In order to validate this claim, a series of planar scans with different amount of the attenuation medium (solid water) were performed, using Siemens Symbia Intevo, MELP collimator, at the NM department of Toronto General Hospital. The energy window settings were the same as those used in the patient acquisitions. The activity of the ^{177}Lu was ranged from 11 to 10585 MBq. The dead-time losses for primary photon were plotted as functions of detected photon count rate in PW, in PW+LSW+USW and in whole spectrum (Figure 5.7). The results presented in Figure 5.7 clearly show that the dead-time count losses for primary photon are least affected by the amount of the attenuation medium when analyzed as a function of whole spectrum count rate.

The average whole spectrum photon count rate (over all projections) for the entire patient population is summarized in Table 5.4. From this table, the mean value of the averaged whole spectrum count rate was about 30 - 80 kcps. The corresponding dead-time count losses were only

about 1.4% - 3.8% according to our previous study [141]. Moreover, the dead-time effect mainly affects the acquisitions performed on D0. This analysis suggests that the camera dead-time will not significantly change the estimated kidney doses. This was confirmed by the results presented in Figure 5.4.

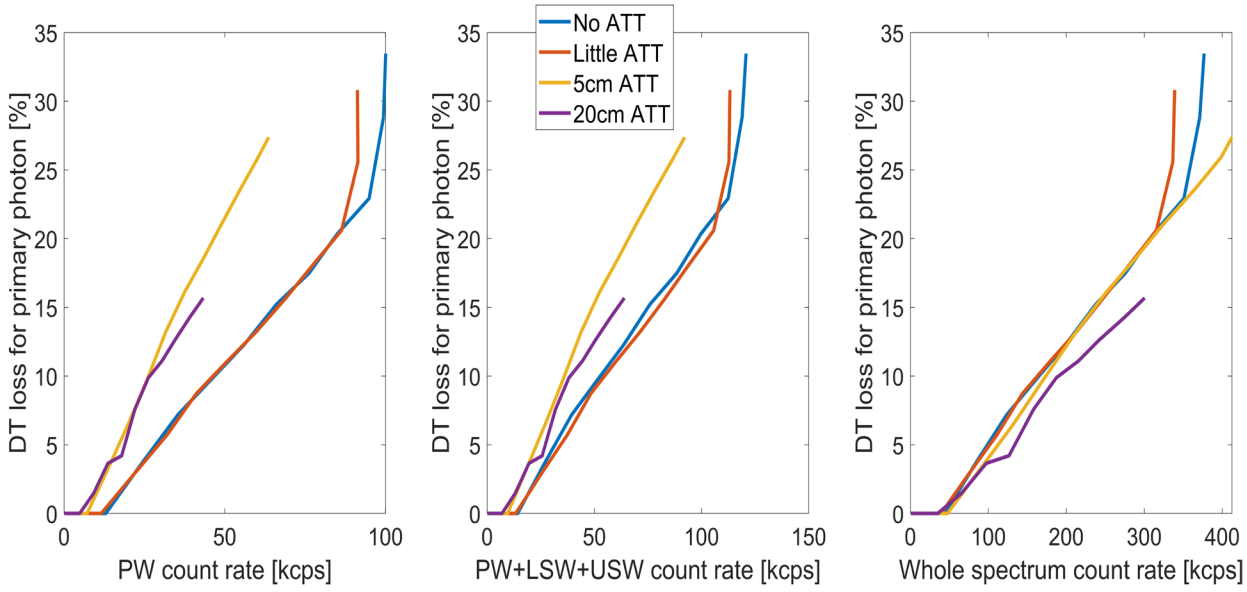

Figure 5.7 Dead-time (DT) losses of the primary photon counts, for a series of planar scans of the same radioactive sources (11 - 10585 MBq) performed under different level of photon attenuation (ATT) and scattering conditions (realized by solid water slabs with different thicknesses). The dead-time losses were analyzed as a function of the detected photon count rate in PW (left), the total count rate in PW+LSW+USW (middle) and the whole spectrum count rate (right). The unit of count rate was kilo count per second (kcps).

Table 5.4 Summary of the whole spectrum count rates (averaged over all projections) for the patient data analyzed in this chapter. The mean, minimum as well as the maximum count rate are provided. The maximum dead-time loss for primary photons was about 8.1% (happened at 169.2 kcps).

Whole spectrum count rate averaged over all projections [kcps]	D0 scan	D1 scan	D3 scan
Mean	79.4	54.3	32.3
Minimum	41.2	24.3	14.1
Maximum	169.2	143.5	75.3

5.4.2 TAC creation method

Ideally, in order to measure both the uptake and clearance phases of the radiopharmaceutical in an organ or tumour, multiple SPECT/CT acquisitions need to be performed. For example, EANM guidelines suggest three activity measurements per kinetic phase [250]. This approach, however, would put a lot of burden on both patients and nuclear medicine departments. Therefore, most dosimetry studies are being performed with three or four acquisitions [6,7,154,249,251]. For the same reasons, we performed three measurements and stopped the data collection three days' post injection. The discussion presented in this section focuses on the best TAC creation method based on the available SPECT/CT imaging data.

Analysis of the data from a patient with five SPECT/CT measurements shows that the kidney TACs created from M1 are very similar to those obtained from the biexponenital fit to all five data points (Figure 5.3): Monoexponential curve determined from D1 and D3 data points

also passes through points corresponding to late measurements (performed on D6 and D9). Compared with TACs modelled using M1, these biexponential curves include the information from two additional data points, thus can be considered a more accurate representation of TACs than those based on three data-point only. The areas under the TACs created by M1 and those created by biexponential fit differ by 1.5% for L-kidney and 3.6% for R-kidney and that the difference is mostly in the part corresponding to the first 24 h. This result supports the choice of M1 as the gold standard method for cases where only three SPECT/CT acquisitions are available.

Although in our study only one dataset with late measurements was available, similar conclusions about effective half-life of slow clearance phase were drawn from other studies with SPECT acquired up to 168 hours post injection, as detailed in Table 5.5. The last column provides the 95% confidence interval of difference in mean effective half-life, calculated based on unequal variances two-sample t statistics. This statistical analysis indicates that the population mean effective half-lives determined from these two studies agree well with that obtained in our study. This also supports using M1 as the gold standard TAC creation method, because monoexponential fit to D1 and D3 data points accurately determines the shape of TAC corresponding to the kidney slow clearance phase.

As discussed in the Methods section, the D0 measurement might contain the kidney uptake phase and/or clearance phase due to the inter-patient variability of the radiopharmaceutical bio-kinetics in kidney. Inclusion of D0 data points in the kidney slow clearance phase curve fitting will introduce error to the shape of the TACs. This agrees with the results presented in Figure 5.4 and Figure 5.5. The effective half-lives determined from the monoexponential fit to D0, D1 and D3 data points were longer than those determined from the fit

of D1 and D3 data points. As a result, the corresponding estimated radiation doses by M2 were bigger than those from M1.

Table 5.5 Comparison of population mean effective half-lives of kidney slow clearance phase obtained from the current study and from other studies with SPECT acquisitions up to 168 hours.

Study	Acquisition times & Number of patients	T_{em} - mean effective half-life of kidney slow clearance phase	95% confidence interval of difference in mean effective half-life[1]
Current study	4, 23, 70 h; 39 patients	45 h	—
Hippeläinen et al. [203]	24, 48, 168 h; 10 patients	~45 h	NA[2]
Garske et al. [252]	24, 72, 168 h; 30 patients	~52 h	(-9 h, -4 h)
Heikkonen et al. [253]	24, 72, 168 h; 24 patients	~45 h	(-3 h, 3 h)

[1] Calculated based on unequal variances two-sample t statistics.

[2] Tabulated effective half-lives were not available.

A recent review article published by Cremonesi et al. summarized the results of kidney absorbed doses from eighteen ^{177}Lu DOTATATE patient studies [254]. The mean (or median) kidney dose per unit injected activity ranged from 0.3 - 1.0 mGy/MBq in these studies. The results of our kidney dosimetry obtained from M1 also falls within this range (see Table 5.3). This is another evidence supporting the choice of M1 as the best TAC creation method for kidney doses estimation of the current ^{177}Lu DOTATATE patients. The mean value of the kidney doses determined in our study is smaller than most of the studies mentioned in [254]. This can be explained by the fact that the kidney was segmented using a small volume (usually 2 cm diameter spherical VOI) placed at uniform, high uptake region of kidney in most of these clinical studies. As a result, the activity concentrations (thus the absorbed dose value) estimated from these small volumes tend to exceed those calculated from the entire kidney segmentation applied in our study.

The results of Figure 5.4 also showed that the kidney dose calculated based on M3 (or M4) was almost the same as those estimated from M1 (or M2). This means that the area under the TAC (thus the absorbed dose estimate) mainly depends on the shape of the kidney slow clearance phase. Using the trapezoidal functions from zero to D3 has negligible impact on the estimated kidney dose.

5.4.3 S factor

Grimes et al. compared the image-based dosimetry obtained using OLINDA/EXM software and Monte Carlo technique [255]. This study showed that for ^{177}Lu:

- More than 98% of the dose delivered to the kidney was by the radiopharmaceutical within the kidney, i.e. the source and target regions in Equation 1.4 were both kidneys (also known as self-irradiating).
- The self-irradiating S factor obtained from OLINDA/EXM was accurate as its value was almost identical to those calculated based on Monte Carlo simulations.

Based on these results, the kidney self-irradiating S factor provided by OLINDA (0.289 mGy/(MBq·h) for 299 g kidney mass) was used to estimate the mean dose. In order to account for the kidney mass difference between the standard human phantom (used in OLINDA) and each particular patient, the OLINDA S factor was rescaled to each patient's kidney mass (based on Equation 5.2) before it was plugged into Equation 5.1.

5.4.4 Importance of personalized dosimetry

The results presented in Table 5.3 showed that among the investigated patients the dose per administered activity could differ by up to 9 times for the left kidney, and by up to 7 times for the right kidney. In other words, a large inter-patient variability in kidney absorbed doses will be observed if same amount of radiopharmaceutical is injected. This finding clearly shows the importance of performing personalized dosimetry for the patients undergoing ^{177}Lu DOTATATE radionuclide therapy.

Although the patients in our study were treated with personalized administration of ^{177}Lu DOTATATE, a large inter-patient variability in kidney absorbed doses per therapy cycle was observed (Table 5.3). This is because the personalization of the radiopharmaceutical injection mainly aimed to minimize the differences between patients in cumulative kidney dose delivered

over four therapy cycles. For the majority of the patients, only the first therapy cycle was included in the analysis. Due to the inter-patient variation, large differences in kidney dose per therapy cycle might occur.

Currently, most ^{177}Lu DOTATATE radionuclide therapies use 23 Gy (or 5.75 Gy per therapy cycle) as the kidney dose limit, which is based on the knowledge established from the experience of external beam therapy [256,257]. According to the results of Table 5.3, at least 90% of the patients' kidney dose was smaller than this limit. Thus, the administered activity could be potentially increased for later cycles in order to improve the treatment outcome.

The analysis of the results presented in Figure 5.6 showed that the inter cycle variability in kidney dose per injected activity was relatively small. This means that for the same patient, the dose estimation from the previous therapy cycle could be useful to predict the dose for the next therapy cycle. This result also strengthens the importance of performing dose based radiopharmaceutical prescription for reducing the inconsistency of the dose to kidney between patients.

The aim of the PRRT therapy is to deliver as large radiation dose to tumours as possible while keeping the radiation dose to kidney below pre-defined threshold. For our patients, the mean/median of the kidney dose per therapy cycle was about 3.5 Gy (Table 5.3). According to the clinical studies by other authors, the mean/median dose absorbed by the dominant tumour per therapy cycle was about 35 Gy to 45 Gy [258–260], while the kidney doses (3-4 Gy) were similar to ours. These tumour doses have been shown to be effective in decreasing tumour burden [258].

5.5 Conclusions

In this chapter, an accurate TAC curve creation method was proposed for the kidney absorbed dose estimation based on multiple post therapy SPECT/CT acquisitions. The dead-time correction factor should be analyzed as a function of whole spectrum counts rate, as in this case its value is less dependent on the photon attenuation and scattering medium. The dead-time count losses for primary photon were less than 5% for the majority of our patients and had negligible impact on the estimated kidney dose. Large inter-patient variability in kidney doses per injected activity observed in our patient study emphasizes the importance of performing personalized dosimetry for the optimization of ^{177}Lu DOTATATE radionuclide therapy.

Chapter 6: Accuracy of simplified image-based dosimetry protocol

6.1 Introduction

As discussed in Chapter 1, PRRT has been proved to be one of the most effective treatments for neuroendocrine tumours (NETs) [86]. In particular, PRRT with ^{177}Lu DOTATATE has been reported to result in substantially improved tumour response as compared to conventional treatments, improved quality of life, as well as low organ toxicity [4,74,79]. Although several studies have showed the clinical benefit of dosimetry in radionuclide therapies [198,261], currently it is not performed in routine clinical practice of ^{177}Lu DOTATATE therapy. The main reason is that the dose estimate in radionuclide therapy is considered a burdensome task for busy clinics. As in this therapy, the kidneys are the one of main critical organ [262], we focus our study on kidney dosimetry.

To make the dosimetry less demanding, many clinical studies investigated the performance of kidney dose calculation method based on simple planar images [257,263,264]. In these studies, 2D regions of interest, usually approximated by ellipses or polygons, were used to determine kidney activities and volumes. However, as discussed in Chapter 2, the planar scans are known to have limitations in quantitative imaging of activity because of the tissue overlapping. Consequently, dosimetry based on planar acquisitions and that based on tomographic studies have been shown to result in different dose to tumour response relationships [265].

To overcome the inherent quantification problems of planar imaging, multiple quantitative SPECT/CT scans were performed to calculate kidney absorbed doses in studies by other authors [242,246,266]. Aiming to simplify the dosimetry procedure, in some of these tomographic studies, instead of performing time-consuming 3D kidney segmentations on the series of reconstructed images, small VOIs were placed inside the kidneys. Activity concentrations determined using these small volumes, such as, for example, 2 cm diameter spheres, were subsequently used to estimate kidney absorbed doses. However, due to the inter-patient variability of the activity distributions in kidneys, the doses estimated from the small VOIs may not correlate with those estimated from the entire kidney volume. In other studies, kidney activities and their volumes were both determined using the same 3D VOIs drawn manually on CT images [245,262] with activity 'spill out', due to partial volume effect, ignored. Using this approach, Guerriero et al. investigated the influence of imaging timing and TAC integration method on kidney absorbed doses [245]. This study confirmed that using different TAC creation method results in large (more than 30%) differences in absorbed dose estimates, therefore multiple scans, with the emphasis on the late time-points, were recommended.

On the other hand, again in an attempt to make dosimetry procedures simpler and more practical, Hänscheid et al. [249] proposed to perform dosimetry calculations based on a single scan acquired on day four after the radiopharmaceutical injection. However, his recommendations may be difficult to generalize, because they were based on the data from whole body planar scans, with no corrections for photon attenuation and scatter. A similar absorbed dose estimation method from a single time point scan has been described by Madsen et al. [267]. Their study used simulation experiments, with conclusions retrospectively applied to

the analysis of patients' data undergoing therapy using ^{90}Y-DOTATOC and suggested scanning at time equal to the mean time of the washout rate constant. This radiopharmaceutical, however, may have different effective half-life and bio-kinetics compared to ^{177}Lu DOTATATE so their conclusion may not apply to our patient population.

The aim of this chapter is to propose a simple yet accurate method for absorbed dose estimation, which will be sufficiently practical to be implemented into routine clinical practice of radionuclide therapy. To achieve this goal, the accuracy of the kidney dose estimates obtained from the simplified data acquisition schedules (with two scans, or even potentially with only one) was assessed. Contrary to the study by Hänscheid et al. [249], the NET patients' data, acquired from three fully quantitative ^{177}Lu DOTATATE SPECT/CT scans, were analyzed. The timing of these three scans was carefully selected, taking into consideration patient and nuclear medicine department constrains [241,242]. In order to accurately determine the dose, the activities and volumes of the kidneys were estimated from SPECT and CT images, respectively.

6.2 Methods

Thirty-nine NET patients with one to four cycles of ^{177}Lu DOTATATE radionuclide therapy were included in the dosimetry analysis. The patient characteristics, as well as the therapy administration information were described in Chapter 5, Section 5.2.1.

Patient imaging protocols, image reconstruction, SPECT quantification and kidney segmentation were the same as those described in Section 5.2 of Chapter 5. To be consistent, the kidney activity data points obtained from three post therapy SPECT reconstructions were also

denoted as D0 data point, D1 data point and D3 data point. According to the conclusions of Chapter 5, the camera dead-time effect has no impact on the estimated doses. Therefore, the dead-time correction was not applied to the kidney activity data points discussed in this chapter.

6.2.1 TAC creation and dosimetry for simplified dosimetry methods

6.2.1.1 TAC creation for two data points methods

For the dose estimation methods based on two data points, one early data point (either D0 or D1) and one late data point (D3) were used. The following two TAC creation methods were investigated (since M1 - M4 were used in Chapter 4, M5 and M6 were used to denote these two methods based on two data points):

- M5: Monoexponential curve obtained from fitting to D0 and D3 data points.
- M6: Monoexponential curve obtained from fitting to D1 and D3 data points.

6.2.1.2 TAC creation for single data point methods

Madsen et al. have proposed a dose estimation method base on a single measurement, where the patient specific effective half-life was approximated by the population mean effective half-life [267]. To validate this approach, the data from our patient studies (53 therapy cycles in total) were randomly divided into two groups. The first group of patients (N=27, group-A) was used to determine the population mean effective half-life of kidney (T_{em}). For each dataset, the monoexponential curve fitting of D1 and D3 data points was used to determine the kidney effective half-life. This mean effective half-life was subsequently applied to the data from the second patient group (N=26, group-B) to evaluate the dosimetry based on the single data point

approach. For each patient, the performance of the following three TAC creation methods was evaluated:

- Monoexponential curve with effective half-live equals to T_{em}, passing through D0 data point.
- Monoexponential curve with effective half-live equals to T_{em}, passing through D1 data point.
- Monoexponential curve with effective half-live equals to T_{em}, passing through D3 data point.

6.2.1.3 Kidney dosimetry

Once the TAC was built based on these simplified methods (either two data points or single data point), the time-integrated activity was calculated as the area under the TAC, from time zero to infinity. Then, the Equation 5.1 and Equation 5.2 (Section 5.2 of Chapter 5) were used to calculate the kidney dose.

6.2.1.4 Data Analysis

As discussed in Chapter 5, in our opinion, the shape of TACs created from M1 reflects most accurately the bio-kinetics of radiopharmaceutical in kidneys. Therefore, the dose values corresponding to M1 were used as the reference to assess the performance of the simplified dose calculation methods.

Please note that dose estimated from M2 (described in Chapter 5) was also included in the analysis, because:

- It was considered to be a simple TAC modeling method since only monoexponential curve was used.
- The comparison between M2 and other simplified TAC creation methods described in this chapter (M5 and M6) could be useful for the determination of the best simplified acquisition schedule.

The accuracy of dosimetry was evaluated in terms of the relative error (Δ_{dose}) with respect to the absorbed dose estimated from M1:

$$\Delta_{dose} = \frac{D_i - D_1}{D_1} \times 100\% \quad (6.1)$$

Where D_1 is the absorbed dose calculated from M1 and D_i is the absorbed dose calculated from the investigated method (M2 or M5 or M6 or the single data point method).

The effective half-lives of the TACs depend on the data points used in the monoexponential curve fitting. There were three curve fitting methods used in this study. They are summarized in Table 6.1.

Table 6.1 The monoexponential curve fitting method applied in each TAC creation approach.

Name of the curve fitting method	Data points used in curve fitting	Corresponding TAC creation method
D1+D3	D1 and D3 data points	M1 and M6
D0+D1+D3	D0, D1 and D3 data points	M2
D0+D3	D0 and D3 data points	M5

Define the relative error in effective half-life ΔT_{eff} as:

$$\Delta T_{eff} = \frac{T_i - T_1}{T_1} \times 100\% \tag{6.2}$$

Where T_1 is the effective half-life determined from D1+D3 method (used in M1 and M6), while T_i is the effective half-life determined from either D0+D1+D3 method (used in M2) or D0+D3 method (used in M5).

6.2.2 Theoretical background for the single data point method

Following Madsen et al. [267] philosophy and assuming that the radiopharmaceutical elimination from the kidneys can be described by the monoexponential curve with an effective half-life equal to T_{eff}, the time-integrated activity (Ã) can be calculated using a single measurement at time T_s, according to the formula:

$$\tilde{A} = \int_0^{\infty} A(0) \cdot 2^{-\frac{t}{T_{eff}}} dt = \frac{A(0) \cdot T_{eff}}{ln2} \tag{6.3}$$

However, since the information about the kidney activity at time = 0, namely $A(0)$, is not available, we extrapolate it from $A(T_s)$ which corresponds to the activity value obtained from the measurement performed at time T_s:

$$A(0) = A(T_s) \cdot 2^{\frac{T_s}{T_{eff}}} \tag{6.4}$$

Then, Ã becomes:

$$\tilde{A} = \frac{1}{ln2} \cdot A(T_s) \cdot 2^{\frac{Ts}{T_{eff}}} \cdot T_{eff} \tag{6.5}$$

Assuming that for each particular patient, his/her kidneys' effective half-life (T_{eff}) can be approximated by the population mean effective half-life (T_{em}), the time-integrated activity ($\tilde{A}_{est}$) for this patient, estimated based on this assumption, can be computed using the following equation:

$$\tilde{A}_{est} = \frac{1}{ln2} \cdot A(T_s) \cdot 2^{\frac{Ts}{T_{em}}} \cdot T_{em} \tag{6.6}$$

Instead of searching for the optimal sampling time by solving the equation $\tilde{A} = \tilde{A}_{est}$ [267], we treat T_s as a known parameter and investigate the influence which the deviation of the particular patient's T_{eff} from T_{em} may have on the accuracy of the estimated time-integrated activity. This approach means that for a given T_s the percent difference between $\tilde{A}$ and $\tilde{A}_{est}$ is evaluated as a function of the percent difference between T_{eff} and T_{em}.

The results of this evaluation, calculated using Equations 6.5 and 6.6, could be represented by the following relationship:

$$\frac{\tilde{A}_{est} - \tilde{A}}{\tilde{A}} = \frac{T_{em}}{T_{eff}} \cdot 2^{\frac{T_s}{T_{em}}\left(1-\frac{T_{em}}{T_{eff}}\right)} - 1 \tag{6.7}$$

This equation can be expressed using the following substitutions:

$$y = \frac{1}{x+1} \cdot 2^{\frac{T_s}{T_{em}}\cdot\left(\frac{x}{x+1}\right)} - 1 \tag{6.8}$$

Where: $x = \frac{T_{eff} - T_{em}}{T_{em}}$ and $y = \frac{\tilde{A}_{est} - \tilde{A}}{\tilde{A}}$.

The shape of the curve represented by Equation 6.8 depends on the ratio of T_s to T_{em}. The optimal sampling time should result in a small value of y (<10%) for a wide range of x values occurring in the patient population. In our analysis, we used this equation to assess the robustness of the single data point dosimetry method for the effective half-lives observed in the patient population.

The accuracy of the single data point dose estimate is directly related to the deviation of the patient specific effective half-life from the population mean. Therefore, the evaluation of the statistical behavior of the effective half-life occurred in our patient population should be helpful to evaluate the performance of the single data point method. Considering this: 1) the histogram showing the distribution of the kidney effective half-lives (calculated based on D1+D3 fit method) observed in the patient population was plotted and, 2) the Kolmogorov–Smirnov test was performed to check the null hypothesis that the effective half-lives of kidneys from all patients were normally distributed.

6.3 Results

The kidney doses calculated based on the simplified TAC creation methods (M2, M5 and M6) were compared to those obtained from the gold standard method (M1). The corresponding relative errors are plotted in Figure 6.1.

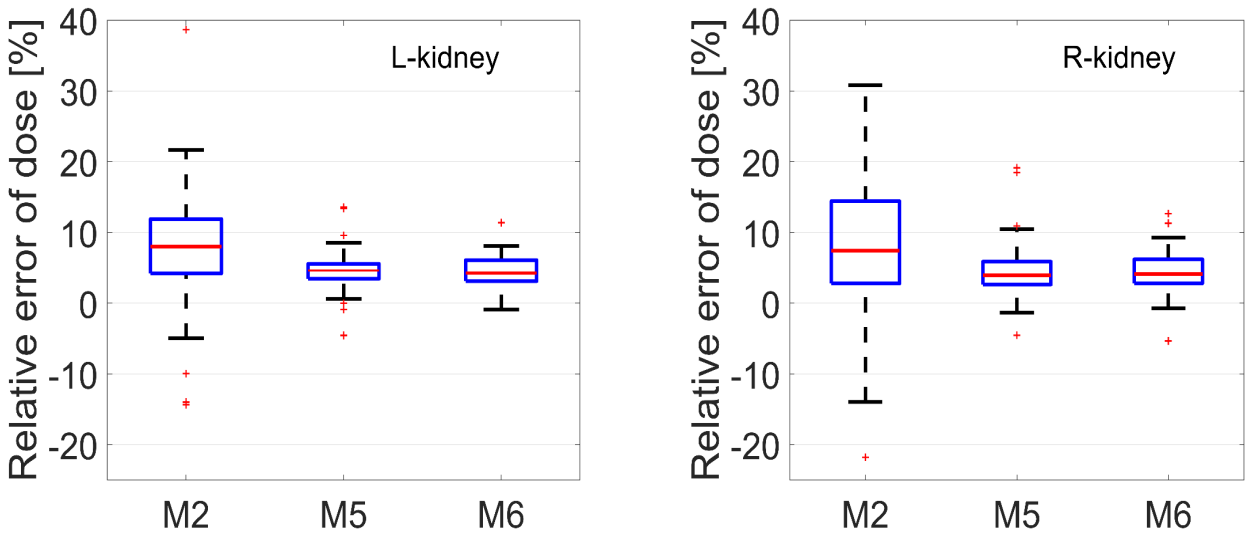

Figure 6.1 Boxplots comparing the accuracy of the kidney doses estimated from M2, M5 and M6. The accuracy was defined as the error of the estimated doses relative to those determined from the gold standard method (M1).

The kidney effective half-lives determined from the 1) D0+D1+D3 method and 2) D0 +D3 data method were compared to those calculated based on the D1+D3 method. The corresponding relative errors are presented in Figure 6.2. These results were used to explain the differences of kidney doses observed in different TAC creation methods.

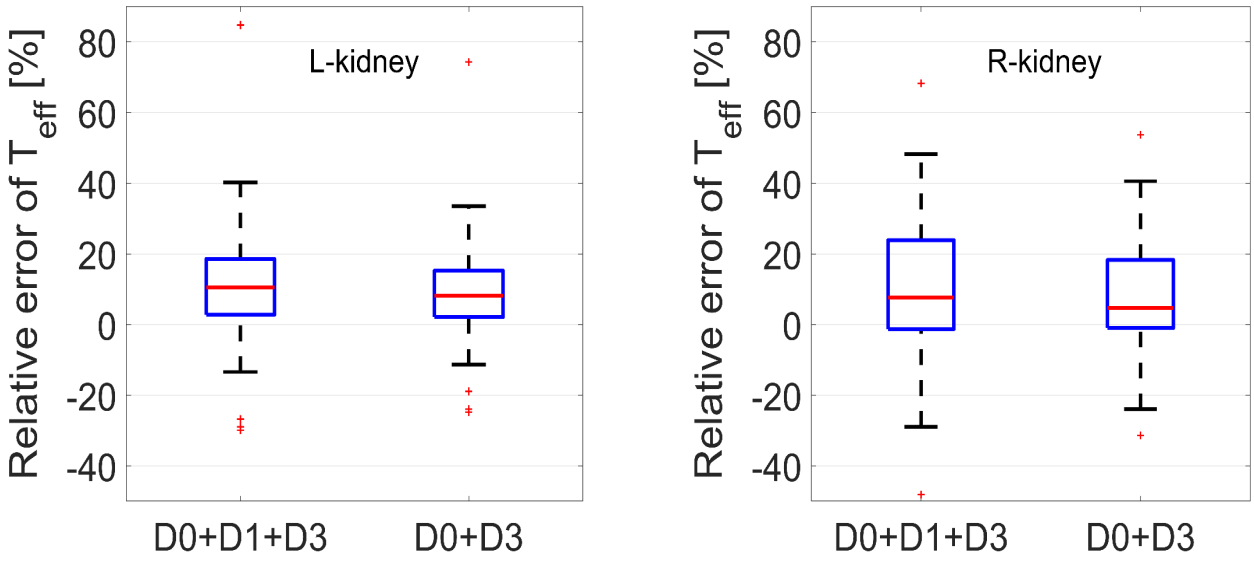

Figure 6.2 Boxplots comparing the relative errors of kidney effective half-lives determined from the D0+D1+D3 method (applied in M2) and D0+D3 method (applied in M5). The kidney effective half-lives obtained from the D1+D3 method (applied in M1 and M6) were used as the reference.

The dose estimates obtained from the single data point methods were compared to those from the gold standard method (M1). The corresponding relative errors are presented in Figure 6.3. Three single data point dose calculation methods were investigated. They use the single SPECT/CT acquisition performed on D0, D1 and D3, respectively.

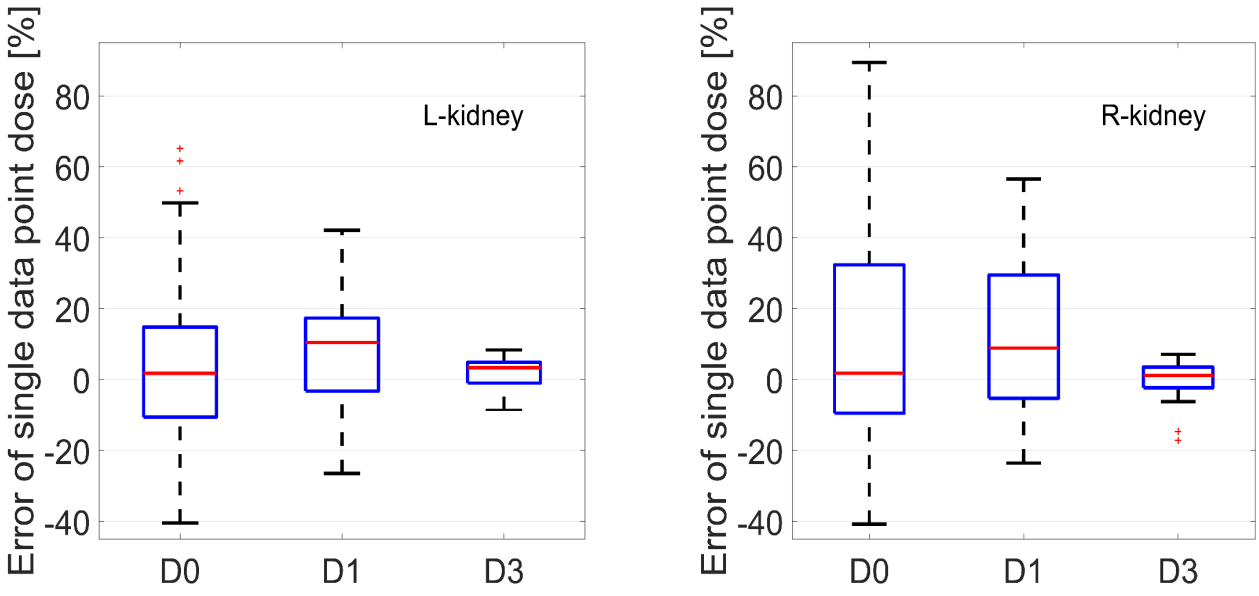

Figure 6.3 Boxplots comparing the accuracy of the kidney dose estimates from the single data point methods, where the patient specific effective half-life was assumed to be the same as the population mean. The performance of three single data point methods was compared. They use the single measurement performed on D0, D1 and D3, respectively. The accuracy was defined as the error of the estimated doses relative to those determined from the gold standard method (M1).

The error in the time-integrated activity (which is proportional to the dose) calculated based on single measurement performed at T_s was analyzed as a function of the deviation of the patient-specific effective half-life from the population mean, assuming monoexponential bio-kinetics in the organ. The results are presented in Figure 6.4. According to the Equation 6.8, the shape of the function depends on the temporal location of the single measurement (T_s). In Figure 6.4, five different values of T_s were investigated, namely $0.1T_{em}$, $0.5T_{em}$, T_{em}, $1.5T_{em}$ and $2T_{em}$. According to our patient data acquisition protocol, they correspond to the single measurement

performed at around 4.5 hours (D0), 22.5 hours (D1), 45 hours, 67.5 hours (D3) and 90 hours after the radiopharmaceutical administration. The distribution of the patient kidney effective half-lives observed in our patient population is shown in Figure 6.5.

The results of the Kolmogorov–Smirnov test, checking if the kidney effective half-lives obtained from different monoexponential curve fitting methods were normally distributed, are summarized in Table 6.2.

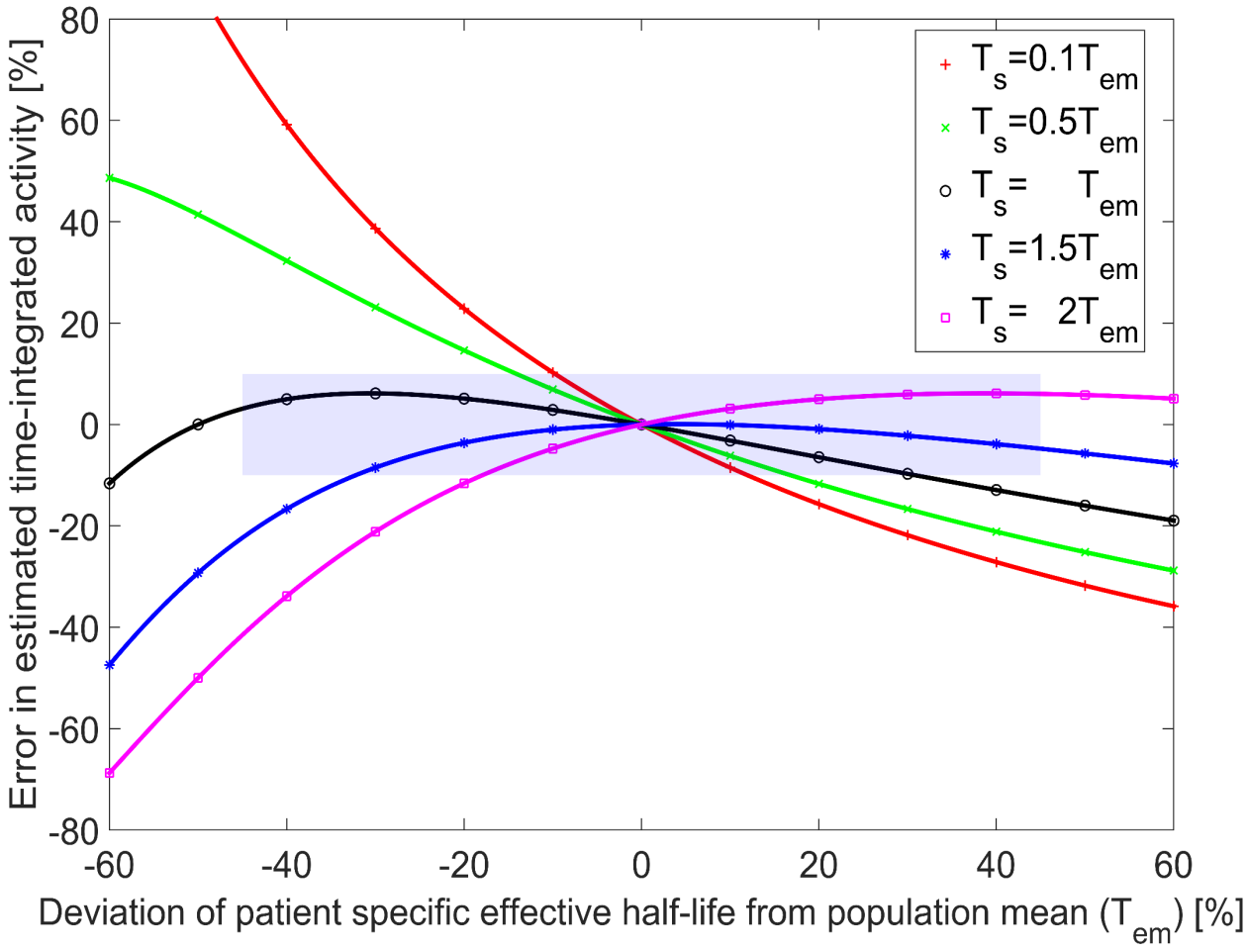

Figure 6.4 Relative errors of the time-integrated activities estimated by the single data point method, using the population mean effective half-life (T_{em}) and imaging data

measured at T_s (Equation 6.8). The organ bio-kinetics was assumed to be the monoexponential clearance. The shaded box represents 10% error threshold in y axis, 45% deviation (two standard deviations based on our patient data) threshold in x axis.

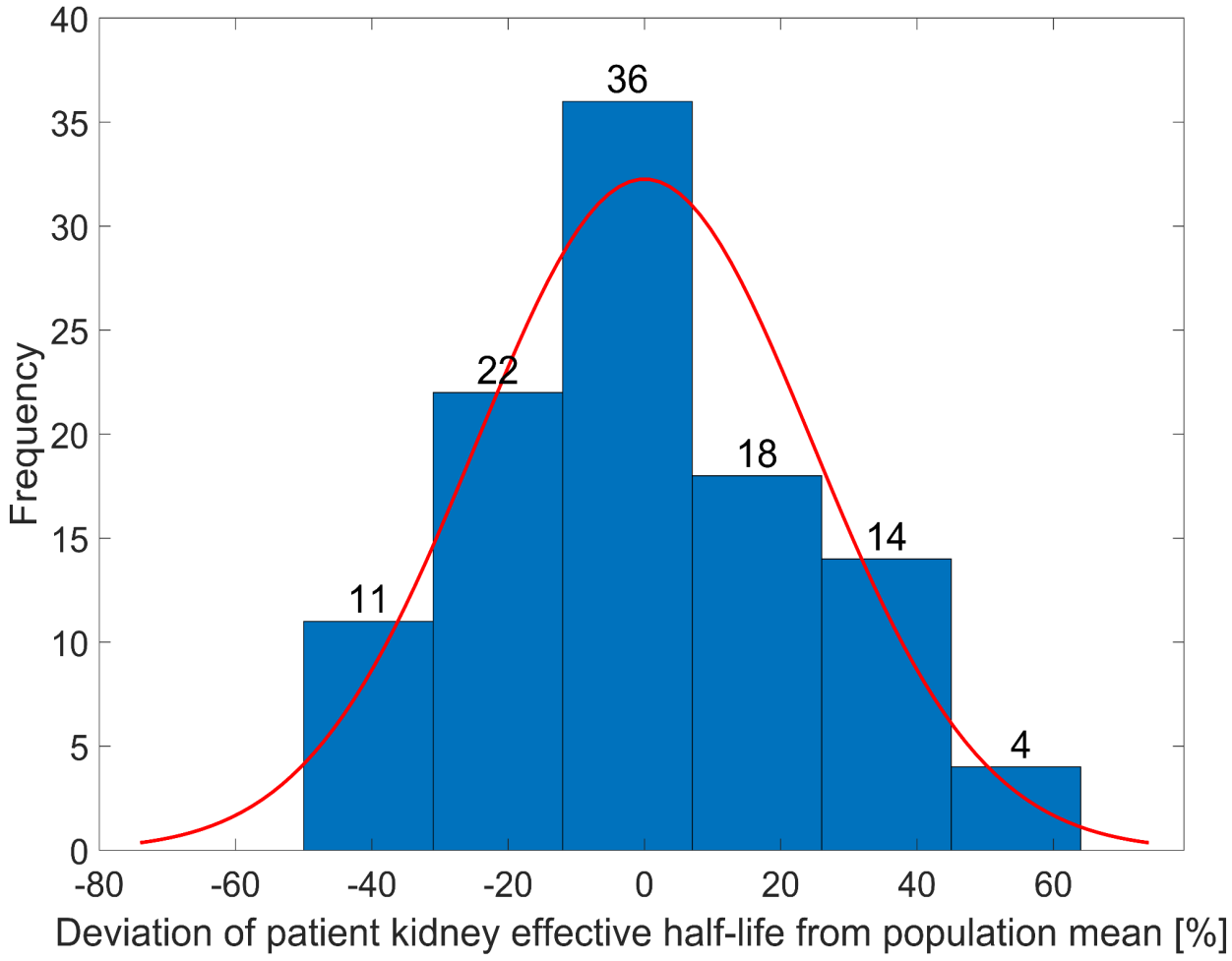

Figure 6.5 Histogram showing the distribution of the patient kidney effective half-lives observed in our patients. For each therapy cycle, the effective half-lives of the kidneys (left and right) were determined using the monoexponential fit to D1+D3 data points. To be consistent with Figure 6.4, the distribution of the deviations of the patient kidneys' effective

half-lives from the population mean was presented. The red curve was the fit of the histogram to normal distribution.

Table 6.2 Summary of the p-values of the Kolmogorov–Smirnov test for kidney effective half-lives obtained from different monoexponential fitting methods.

Monoexponential curve fitting method	**Test p-values**	
	Effective half-lives of L-kidneys	Effective half-lives of R-kidneys
D1+D3 (M1 and M6)	0.72	0.89
D0+D1+D3 (M2)	0.94	0.69
D0+D3 (M5)	0.81	0.64

6.4 Discussion

6.4.1 Influence of early data point (D0)

The analysis of the results presented in Figure 6.1 shows that both the range and interquartile range of errors in absorbed doses calculated based on the monoexponential fit to all three data points (M2) are larger than those calculated based on the fit to two data points only (M5 and M6). While the interquartile range of errors in absorbed dose estimation is comparable for both M5 and M6, the range of errors is larger when the data from D0 is used for the TAC creation (M5). This result can be explained by the fact that the early scan, acquired few hours

post injection, may contain information from both kidney uptake and clearance phases (also mentioned in Chapter 5), where the biggest differences between patients are likely to happen. Given the limited number of SPECT/CT acquisitions in clinical studies, the early data point measured on D0 should not be included in the monoexponential curve fitting as it could introduce error to the shape of the TACs and the dose estimates.

6.4.2 Importance of late data point (D3)

Our patient data show that on average around 75% of the area under the TACs comes from the integration of the time interval from D1 to infinity. Since the main contribution to the area under the TAC comes from the time interval from D1 to infinity, the accurate fit to the late data points is very important for accurate dose estimation. This is confirmed by the results presented in Figure 6.1: the range of the errors in kidney absorbed dose estimated by M6, which uses the same TAC shape as M1 in the time interval beyond D1, are the smallest of all methods.

The area under the monoexponential TAC (thus the absorbed dose estimate) depends on two factors: the normalization of the curve and the exponent of the curve (i.e. effective half-life). Contrary to the TACs built by M5, the TACs created by M2 do not have the same normalization at D3 as those used in M1. As a result, the maximum error of doses estimated by M2 is about 20% larger than the maximum error of those obtained from M5 (see Figure 6.1), even if the maximum errors in estimated effective half-lives by these two methods are similar (see Figure 6.2). The analysis of these results shows that, as long as the TACs have the same normalization at the late time point (D3), the area under the curve is less sensitive to the change of the effective half-life of the curve than when early time point (D0 or D1) would be used. In other words, the

SPECT acquisitions performed at the late time points are important for the accurate determination of the area under the monoexponential TACs, which is proportional to the absorbed dose estimation. In our study, the term 'late time point', which is obviously related to the exponent of the TACs, approximately equals to 1.5 times of the population mean effective half-life.

6.4.3 Single data point dosimetry

As described in Methods, in order to estimate the dose from a single measurement, the patient specific effective half-life of the monoexponential TAC needs to be approximated by the population mean effective half-life. This approximation may introduce errors in the absorbed dose calculation, especially for the case when the effective half-life of a particular patient is very different from the population mean. However, as discussed above, the impact of the error in effective half-life on the absorbed dose estimate can be minimized by using late data point for TAC normalization. Thus, the TACs normalized by the data points measured on D3 result in the smallest error in absorbed dose estimation, as shown in Figure 6.3. These results are further supported by the theoretical analysis of curves presented in Figure 6.4. When compared with the single measurement on D0 (red curve) and D1 (green curve), the single measurement on D3 (blue curve) results in a relatively flat curve over a wide range of T_{eff} deviations. That is to say, the single data point method using D3 measurements leads to small dosimetry errors even for the case when the patient-specific half-life deviates far from the population mean half-life.

The p-values presented in Table 6.2 indicate that we fail to reject the null hypothesis at 5% significance. The results in Figure 6.5 also indicate that the effective half-lives of kidneys from all patients are normally distributed. For the majority of our patient (two standard

deviations interval of normal distribution, corresponding to the shaded box in Figure 6.4), the deviations of kidney effective half-lives from the population mean are less than 45% (Figure 6.5). For these patients, the errors in absorbed dose estimation based on the single measurement performed in the time interval between T_{em} and $1.5T_{em}$ are relatively small, mostly below 10% (Figure 6.4). For the studies aiming at absorbed dose estimations in more than organs, the single acquisition time should be adjusted based on the statistical behaviors of the effective half-lives in all targeting regions. i.e. the acquisition time should be at T_{em} and $1.5T_{em}$ for all organs' T_{em}. For situations where the effective half-lives for these organs of interest differ largely, acquiring the single measurement at a later time would be recommended as overall it would result in relatively small error in dose estimate.

Similar to the observations by Madsen et al. [267], that kidney absorbed dose for ^{177}Lu DOTATATE patients can also be estimated with acceptable error (<10%) by the single data point method, assuming that the information about population mean effective half-life is available. However, the results presented in Figure 6.4 does show that the optimal time for this single scan is slightly influenced by the statistical behavior of the organ effective half-lives for the investigated patient population. For organs with effective half-lives normally distributed around the T_{em}, the best imaging time would be at about T_{em} to $1.5T_{em}$ (consistent with Madsen et al.'s suggestion: $1.44T_{em}$) which, according to our data, would be approximately 48-72 hours after the ^{177}Lu DOTATATE administration for kidney dosimetry. While for the organs which have slightly higher probability to have long effective half-life (i.e. more chance to have positive deviation in x axis of Figure 6.4), the best imaging time would be at $1.5T_{em}$ to $2T_{em}$ after the radiopharmaceutical injection. This result agrees with the study by Hänscheid et al. [249]: the

single measurement on 72 hours post-injection is adequate for dose estimate of kidney, while for NET lesions (which tend to have long effective half-lives) single measurement performed at 120 hours leads to the best result.

6.5 Conclusions

In this chapter, the performance of three simplified dose calculation methods (based on either two or three data points) was evaluated. When using monoexponential curve to model TAC, the late data point (D3 in our study) is important for accurate determination of the time-integrated activity. For ^{177}Lu DOTATATE therapy, the single data point method using late measurement (48 hours to 72 hours post therapy injection) yields small error (<10%) in kidney dose estimation for the majority of patients, thus it can be recommended for clinical use.

Chapter 7: Conclusions and future work

7.1 Conclusions

The ^{177}Lu DOTATATE radionuclide therapy is considered an effective treatment for patients with metastatic NETs. Currently, this therapy is conducted with 'one-size-fits-all' protocol where all the patients are injected with similar amount of radiopharmaceutical. This is obviously far from optimal as large inter-patient variability in dose to organ at risk and tumours was reported in many studies. The main motivation of this thesis was to propose a practical and accurate dosimetry protocol based on SPECT imaging studies, so that it can be implemented in clinics for the optimization of the radionuclide therapy. To achieve this goal, four studies focusing on different aspect of SPECT image-based dose estimation, were performed:

- The performance of different SPECT camera calibration methods was compared in Chapter 3. The objective of this chapter was to propose a simple, yet accurate SPECT camera calibration method for quantitative measurement of the therapeutic radioisotopes in clinics. The calibration factors determined from tomographic scans of a phantom filled with uniform activity were found to be equivalent to those calculated from planar scans of a point-like source, while the calibration factors obtained from tomographic scans of radioactive sources placed in a background of non-radioactive water had higher values. The analysis of the results from the simulation studies indicated that 1) for the source placed in non-radioactive water, the overestimation of the calibration factor was due to the inaccuracies of the scatter modelling by the TEW method, and 2) for planar scan

calibration, the background from high energy scattered photons and septal penetration need to be removed using TEW method. The planar calibration procedure is simple and fast, thus is recommended for clinical use.

- The ^{177}Lu activity quantification performance of the clinical software (Flash3D) reconstructed images was evaluated in Chapter 4. The aim of this chapter was to ensure the SPECT reconstructions from a clinical software (provided by the manufacturer of the camera) could be used to perform quantitative measurement of ^{177}Lu activity within patient body. The phantom experiments with different photon attenuation and scattering conditions were performed. The accuracies of the ^{177}Lu activity quantification, from the SPECT images reconstructed using both clinical software and in-house developed quantitative algorithm, were directly compared. For all phantom experiments, the activity recovery of the radioactive sources, calculated from both reconstructions, agreed to within 5%. In particular, for the phantom experiments with spherical sources placed in radioactive water background, at least 90% of the activity was recovered for the largest source (113 mL) when CT image was used for the segmentation. The activity recovery was even higher (at least 95%) when IAT method was used for the segmentation. These results showed that the SPECT images reconstructed by clinical software were accurate for the activity quantification of large regions (>100mL) if proper segmentation method was applied. However, the activity distributions estimated from these two reconstructions were slightly different. Due to the approximation made in camera 3D resolution recovery, the clinical reconstructions were noisier than those from the in-house developed

algorithm. Therefore, post reconstruction image filtering is recommended for the determination of the activity distribution using clinical reconstructions.

- The kidney absorbed dose for the NET patients undergoing ^{177}Lu DOTATATE radionuclide therapy was calculated in Chapter 5. The aim of this chapter was to propose an accurate dosimetry protocol under clinically relevant conditions. The conclusions from Chapter 3 and Chapter 4 were applied to this chapter in order to obtain a series of quantitative measurements of ^{177}Lu activity in kidney based on clinical reconstructions. The dose estimation from different TAC modeling methods was compared. The camera dead-time count loss was usually less than 5% thus was found to have negligible impact on the kidney doses. Large inter-patient variability in kidney dose per administered activity of the radiopharmaceutical demonstrated the importance of performing personalized dosimetry for improving tumour response and limiting normal tissue toxicity.

- The accuracy of the kidney dose estimated from the simplified dose calculation methods was investigated in Chapter 6. The aim of this chapter was to simplify the image-based dosimetry protocol so that it can be applied in routine clinics for the optimization of radionuclide therapy. The kidney doses calculated based on the most accurate method M1 (described in Chapter 5) were used as the reference standard to assess the accuracy of the kidney doses obtained from three simplified calculation methods. With the limited number of SPECT/CT acquisitions in clinical studies, including the early data point (few hours post radiopharmaceutical injection) in the TAC fitting can introduce errors to the

dose estimation. On the other hand, the late data point (about three days' post therapy administration in our study) was important for accurate determination of the TACs. The monoexponential TACs with population mean effective half-life, using single measurement performed at the late time (about two to three days' post therapy injection for kidney), led to small errors (<10%) in dose estimation for the majority of our patients. Benefiting from its simplicity, this single data point method has great potential to be widely accepted in routine therapies.

It should be noted that the conclusions of these four subprojects are general and can be applied to image-based dosimetry studies for other clinical therapies. For example, the camera calibration method proposed in Chapter 3 can be applied to the activity quantification study of ^{131}I, ^{188}Re and other medical radioisotopes. The CT image guided activity segmentation with partial volume effect correction factor can be applied for the activity quantification of critical organs in other radionuclide therapies. The single data point method can be used for the dose estimate in other treatments, as long as the organ bio-kinetics can be described (or approximated) by monoexponential TACs.

7.2 Contribution to the field

A general image-based dosimetry protocol has been developed for personalizing clinical radionuclide therapy. The accuracy of this protocol has been assessed for the NET patients undergoing ^{177}Lu DOTATATE therapy. The large inter-patient variabilities in kidney absorbed dose per unit injected activity emphasize the importance of using personalized approaches in clinical therapies. As the radiopharmaceuticals are usually delivered at multiple therapy cycles, the dosimetry results obtained from the early cycle(s) can be used to personalize the injection in the later cycles. The works presented in this thesis demonstrate that dosimetry for clinical radionuclide therapies can be performed with minor additional effort. The widespread usage of dosimetry will improve our understanding of clinical therapies, and ultimately benefit millions of patients.

7.3 Future work

There are many research topics that could potentially further improve the efficacy of radionuclide therapy. Some of these topics are described as follows.

7.3.1 Segmentation methods for tumour and critical organ

Due to the limited spatial resolution of SPECT images, the segmentation of tumours and critical organs is a challenging task. In this thesis, the critical organ activity was accurately determined using the IAT segmentation method [218,229]. However, this method needs the calibration curve, which requires a series of phantom experiments with a wide range of source to background activity ratios. These might not be possible to perform in a busy NM department.

Therefore, the performance of the automatic segmentation methods needs to be tested with SPECT reconstructed images. For example, the 3D gradient based edge detection [268] and fuzzy c-mean clustering segmentation [269] might be of interest, as they are 1) fast and easy to perform 2) shown to provide accurate and reproducible results for the segmentation of medical images acquired by other modalities. For such validation studies, high contrast CT images need to be acquired as they can provide reference for the anatomical volume, especially for the small VOIs. Additionally, these CT images can be used to create accurate photon attenuation maps. With this information, Monte Carlo simulation of patient projection images can be performed for given activity distribution within patient body. This could be very helpful since in simulated data the true activity of the VOI (tumours or critical organ), which should be used as the reference standard for activity segmentation, would be known.

7.3.2 Parameters for the prediction of tumour response and critical organ toxicity

The primary aim of the radionuclide therapy is to provide therapeutic benefits for patients. However, such therapy is always associated with a potential damage to critical organs due to their inevitable absorbed doses. Therefore, it is very important to define parameters that would correlate with treatment response and critical organ toxicity. Based on the experience in external beam radiation therapy, the absorbed dose could be a very powerful parameter for this purpose. With the dosimetry protocol presented in this thesis, large number of patient kidney dose datasets could be available. Future research should focus on the investigations of kidney toxicity for each patient in order to establish the kidney dose limit. The tumour dosimetry study should be performed in the future for the determination of the dose-response relationship. For this, high contrast CT images will be required for tumour segmentation.

Besides the mean absorbed dose, other dose characteristics such as the dose distributions and dose-volume histograms might be helpful in the assessment of the treatment response. Furthermore, quantitative feature related parameters provided by radiomics analysis may potentially further improve our understanding of treatment outcomes [270].

Bibliography

[1] Kwekkeboom DJ, De Herder WW, Kam BL, Van Eijck CH, Van Essen M, Kooij PP, et al. Treatment with the radiolabeled somatostatin analog [177Lu- DOTA0,Tyr3]octreotate: Toxicity, efficacy, and survival. J Clin Oncol. 2008;26(13):2124–30.

[2] Kwekkeboom DJ, Bakker WH, Kooij PP, Konijnenberg MW, Srinivasan A, Erion JL, et al. [177Lu-DOTA0,Tyr3]octreotate: Comparison with [111In-DTPA0]octreotide in patients. Eur J Nucl Med. 2001;28(9):1319–25.

[3] Wehrmann C, Senftleben S, Zachert C, Müller D, Baum RP. Results of individual patient dosimetry in peptide receptor radionuclide therapy with 177Lu DOTA-TATE and 177Lu DOTA-NOC. Cancer Biother Radiopharm. 2007;22(3):406–16.

[4] Ezziddin S, Khalaf F, Vanezi M, Haslerud T, Mayer K, Al Zreiqat A, et al. Outcome of peptide receptor radionuclide therapy with 177Lu-octreotate in advanced grade 1/2 pancreatic neuroendocrine tumours. Eur J Nucl Med Mol Imaging [Internet]. 2014;41(5):925–33. Available from: http://www.ncbi.nlm.nih.gov/pubmed/24504504

[5] Gupta SK, Singla S, Thakral P, Bal CS. Dosimetric analyses of kidneys, liver, spleen, pituitary gland, and neuroendocrine tumors of patients treated with 177Lu-DOTATATE. Clin Nucl Med [Internet]. 2013;38(3):188–94. Available from: http://www.embase.com/search/results?subaction=viewrecord&from=export&id=L368398490%5Cnhttp://dx.doi.org/10.1097/RLU.0b013e3182814ac1%5Cnhttp://sfx.library.uu.nl/utrecht?sid=EMBASE&issn=03639762&id=doi:10.1097/RLU.0b013e3182814ac1&atitle=Dosimetric+analys

[6] Sandström M, Garske U, Granberg D, Sundin A, Lundqvist H. Individualized dosimetry in patients undergoing therapy with 177Lu-DOTA-D-Phe1-Tyr3-octreotate. Eur J Nucl Med Mol Imaging [Internet]. 2010 Feb 2;37(2):212–25. Available from: http://link.springer.com/10.1007/s00259-009-1216-8

[7] Larsson M, Bernhardt P, Svensson JB, Wängberg B, Ahlman H, Forssell-Aronsson E. Estimation of absorbed dose to the kidneys in patients after treatment with 177Lu-octreotate: comparison between methods based on planar scintigraphy. EJNMMI Res [Internet]. 2012;2(1):49. Available from: http://www.pubmedcentral.nih.gov/articlerender.fcgi?artid=3506567&tool=pmcentrez&rendertype=abstract

[8] Cremonesi M, Botta F, Di Dia A, Ferrari M, Bodei L, De Cicco C, et al. Dosimetry for treatment with radiolabelled somatostatin analogues. A review. Q J Nucl Med Mol Imaging [Internet]. 2010 Feb;54(1):37–51. Available from: http://www.ncbi.nlm.nih.gov/pubmed/20168285

[9] Merola E, Rinzivillo M, Cicchese N, Capurso G, Panzuto F, Delle Fave G. Digestive neuroendocrine neoplasms: A 2016 overview. Dig Liver Dis [Internet]. 2015;48(8):829–35. Available from: http://dx.doi.org/10.1016/j.dld.2016.04.008

[10] Raj N, Fazio N, Strosberg J. Biology and Systemic Treatment of Advanced Gastroenteropancreatic Neuroendocrine Tumors. Am Soc Clin Oncol Educ B [Internet]. 2018 May 23;(38):292–9. Available from: http://ascopubs.org/doi/10.1200/EDBK_200893

[11] Basuroy R, Srirajaskanthan R, Ramage JK. Neuroendocrine Tumors. Gastroenterol Clin North Am [Internet]. 2016 Sep;45(3):487–507. Available from:

http://www.ncbi.nlm.nih.gov/pubmed/27546845

[12] Hallet J, Law CHL, Cukier M, Saskin R, Liu N, Singh S. Exploring the rising incidence of neuroendocrine tumors: A population-based analysis of epidemiology, metastatic presentation, and outcomes. Cancer. 2015;121(4):589–97.

[13] Öberg K, Castellano D. Current knowledge on diagnosis and staging of neuroendocrine tumors. Cancer Metastasis Rev. 2011;30(SUPPL. 1):3–7.

[14] Fraenkel M, Kim M, Faggiano A, de Herder WW, Valk GD, __. Incidence of gastroenteropancreatic neuroendocrine tumours: a systematic review of the literature. Endocr Relat Cancer [Internet]. 2014 Jun;21(3):R153–63. Available from: https://erc.bioscientifica.com/view/journals/erc/21/3/R153.xml

[15] Modlin IM, Oberg K, Chung DC, Jensen RT, de Herder WW, Thakker R V., et al. Gastroenteropancreatic neuroendocrine tumours. Lancet Oncol. 2008;9(1):61–72.

[16] Broder MS, Cai B, Chang E, Neary MP. Incidence and prevalence of neuroendocrine tumors of the lung: analysis of a US commercial insurance claims database. BMC Pulm Med [Internet]. 2018 Dec 13;18(1):135. Available from: https://bmcpulmmed.biomedcentral.com/articles/10.1186/s12890-018-0678-5

[17] Klimstra DS, Modlin IR, Coppola D, Lloyd R V., Suster S. The Pathologic Classification of Neuroendocrine Tumors. Pancreas [Internet]. 2010;39(6):707–12. Available from: http://insights.ovid.com/crossref?an=00006676-201008000-00002

[18] Basuroy R, Bouvier C, Ramage JK, Sissons M, Kent A, Srirajaskanthan R. Presenting Symptoms and Delay in Diagnosis of Gastrointestinal and Pancreatic Neuroendocrine Tumours. Neuroendocrinology [Internet]. 2018;107(1):42–9. Available from: https://www.karger.com/Article/FullText/488510

[19] Modlin IM, Kidd M, Latich I, Zikusoka MN, Shapiro MD. Current status of gastrointestinal carcinoids. Gastroenterology. 2005;128(6):1717–51.

[20] Karppinen N, Lindén R, Sintonen H, Tarkkanen M, Roine R, Heiskanen I, et al. Health-Related Quality of Life in Patients with Small Intestine Neuroendocrine Tumours. Neuroendocrinology [Internet]. 2018 Oct 5; Available from: https://www.karger.com/Article/FullText/494293

[21] Singh S, Asa SL, Dey C, Kennecke H, Laidley D, Law C, et al. Diagnosis and management of gastrointestinal neuroendocrine tumors: An evidence-based Canadian consensus. Cancer Treat Rev [Internet]. 2016;47:32–45. Available from: http://dx.doi.org/10.1016/j.ctrv.2016.05.003

[22] Singh S, Dey C, Kennecke H, Kocha W, Maroun J, Metrakos P, et al. Consensus Recommendations for the Diagnosis and Management of Pancreatic Neuroendocrine Tumors: Guidelines from a Canadian National Expert Group. Ann Surg Oncol [Internet]. 2015 Aug 4;22(8):2685–99. Available from: http://link.springer.com/10.1245/s10434-014-4145-0

[23] Basuroy R, Srirajaskanthan R, Ramage JK. Neuroendocrine Tumors. Neuroendocr Tumors [Internet]. 2016;45(3):487–507. Available from: http://dx.doi.org/10.1016/j.gtc.2016.04.007

[24] Delle Fave G, Kwekkeboom DJ, Van Cutsem E, Rindi G, Kos-Kudla B, Knigge U, et al. ENETS Consensus Guidelines for the Management of Patients with Gastroduodenal Neoplasms. Neuroendocrinology [Internet]. 2012;95(2):74–87. Available from: https://www.karger.com/Article/FullText/335595

[25] Basuroy R, Sarker D, Quaglia A, Srirajaskanthan R, Ramage J. Personalized medicine for

gastroenteropancreatic neuroendocrine tumors: a distant dream? Int J Endocr Oncol [Internet]. 2015 Aug;2(3):201–15. Available from: https://www.futuremedicine.com/doi/10.2217/ije.15.9

[26] Kaltsas GA, Besser GM, Grossman AB. The Diagnosis and Medical Management of Advanced Neuroendocrine Tumors. Endocr Rev [Internet]. 2004 Jun;25(3):458–511. Available from: https://academic.oup.com/edrv/article-lookup/doi/10.1210/er.2003-0014

[27] Eriksson B, Öberg K, Stridsberg M. Tumor Markers in Neuroendocrine Tumors. Digestion [Internet]. 2000;62(1):33–8. Available from: https://www.karger.com/Article/FullText/51853

[28] Yang X, Yang Y, Li Z, Cheng C, Yang T, Wang C, et al. Diagnostic value of circulating chromogranin a for neuroendocrine tumors: a systematic review and meta-analysis. Green J, editor. PLoS One [Internet]. 2015 Apr 20;10(4):e0124884. Available from: https://dx.plos.org/10.1371/journal.pone.0124884

[29] Lawrence B, Gustafsson BI, Kidd M, Pavel M, Svejda B, Modlin IM. The Clinical Relevance of Chromogranin A as a Biomarker for Gastroenteropancreatic Neuroendocrine Tumors. Endocrinol Metab Clin North Am [Internet]. 2011 Mar;40(1):111–34. Available from: http://linkinghub.elsevier.com/retrieve/pii/S0889852910000952

[30] Arnold R, Wilke A, Rinke A, Mayer C, Kann PH, Klose KJ, et al. Plasma Chromogranin A as Marker for Survival in Patients With Metastatic Endocrine Gastroenteropancreatic Tumors. Clin Gastroenterol Hepatol. 2008 Jul;6(7):820–7.

[31] Ćwikła JB, Bodei L, Kolasinska-Ćwikła A, Sankowski A, Modlin IM, Kidd M. Circulating transcript analysis (NETest) in GEP-NETs treated with somatostatin analogs defines therapy. J Clin Endocrinol Metab. 2015 Nov;100(11):E1437–45.

[32] Bodei L, Kidd M, Modlin IM, Severi S, Drozdov I, Nicolini S, et al. Measurement of circulating transcripts and gene cluster analysis predicts and defines therapeutic efficacy of peptide receptor radionuclide therapy (PRRT) in neuroendocrine tumors. Eur J Nucl Med Mol Imaging [Internet]. 2016 May 23;43(5):839–51. Available from: http://link.springer.com/10.1007/s00259-015-3250-z

[33] Modlin IM, Frilling A, Salem RR, Alaimo D, Drymousis P, Wasan HS, et al. Blood measurement of neuroendocrine gene transcripts defines the effectiveness of operative resection and ablation strategies. Surgery [Internet]. 2016 Jan;159(1):336–47. Available from: https://linkinghub.elsevier.com/retrieve/pii/S0039606015007035

[34] Maxwell JE, Howe JR. Imaging in neuroendocrine tumors: an update for the clinician. Int J Endocr Oncol [Internet]. 2015 May;2(2):159–68. Available from: https://www.futuremedicine.com/doi/10.2217/ije.14.40

[35] Joseph S, Wang Y-Z, Boudreaux JP, Anthony LB, Campeau R, Raines D, et al. Neuroendocrine Tumors: Current Recommendations for Diagnosis and Surgical Management. Endocrinol Metab Clin North Am [Internet]. 2011 Mar;40(1):205–31. Available from: http://linkinghub.elsevier.com/retrieve/pii/S0889852910000642

[36] Sivero L, Telesca DA, Ruggiero S, Russo T, Amato M, Bianco T, et al. Endoscopic diagnosis and treatment of neuroendocrine tumors of the digestive system. Open Med [Internet]. 2016 Jan 1;11(1). Available from: https://www.degruyter.com/view/j/med.2016.11.issue-1/med-2016-0067/med-2016-0067.xml

[37] Baumann T, Rottenburger C, Nicolas G, Wild D. Gastroenteropancreatic neuroendocrine tumours (GEP-NET) – Imaging and staging. Best Pract Res Clin Endocrinol Metab

[Internet]. 2016 Jan;30(1):45–57. Available from: http://dx.doi.org/10.1016/j.beem.2016.01.003

[38] Farchione A, Rufini V, Brizi MG, Iacovazzo D, Larghi A, Massara RM, et al. Evaluation of the Added Value of Diffusion-Weighted Imaging to Conventional Magnetic Resonance Imaging in Pancreatic Neuroendocrine Tumors and Comparison With 68Ga-DOTANOC Positron Emission Tomography/Computed Tomography. Pancreas [Internet]. 2016 Mar;45(3):345–54. Available from: http://insights.ovid.com/crossref?an=00006676-201603000-00006

[39] Ruf J, Schiefer J, Furth C, Kosiek O, Kropf S, Heuck F, et al. 68Ga-DOTATOC PET/CT of Neuroendocrine Tumors: Spotlight on the CT Phases of a Triple-Phase Protocol. J Nucl Med [Internet]. 2011 May 1;52(5):697–704. Available from: http://jnm.snmjournals.org/cgi/doi/10.2967/jnumed.110.083741

[40] Bushnell DL, Baum RP. Standard Imaging Techniques for Neuroendocrine Tumors. Endocrinol Metab Clin North Am [Internet]. 2011 Mar;40(1):153–62. Available from: http://linkinghub.elsevier.com/retrieve/pii/S0889852910000964

[41] Jacobs MA, Weinstein S, Hope TA, Aslam R, Yee J, Coakley F. Neuroendocrine Tumors. J Comput Assist Tomogr [Internet]. 2014;38(6):898–914. Available from: http://content.wkhealth.com/linkback/openurl?sid=WKPTLP:landingpage&an=00004728-201411000-00015

[42] Theodoropoulou M, Stalla GK. Somatostatin receptors: from signaling to clinical practice. Front Neuroendocrinol [Internet]. 2013 Aug;34(3):228–52. Available from: http://www.ncbi.nlm.nih.gov/pubmed/23872332

[43] Reubi JC, Waser B. Concomitant expression of several peptide receptors in

neuroendocrine tumours: molecular basis for in vivo multireceptor tumour targeting. Eur J Nucl Med Mol Imaging. 2003;30(5):781–93.

[44] Reubi JC, Waser B. Triple-Peptide Receptor Targeting In Vitro Allows Detection of All Tested Gut and Bronchial NETs. J Nucl Med [Internet]. 2015;56(4):613–5. Available from: http://jnm.snmjournals.org/cgi/doi/10.2967/jnumed.114.153189

[45] Kaemmerer D, Peter L, Lupp A, Schulz S, Sänger J, Baum RP, et al. Comparing of IRS and Her2 as immunohistochemical scoring schemes in gastroenteropancreatic neuroendocrine tumors. Int J Clin Exp Pathol. 2012;5(3):187–94.

[46] Wild D, Fani M, Behe M, Brink I, Rivier JEF, Reubi JC, et al. First Clinical Evidence That Imaging with Somatostatin Receptor Antagonists Is Feasible. J Nucl Med [Internet]. 2011;52(9):1412–7. Available from: http://jnm.snmjournals.org/cgi/doi/10.2967/jnumed.111.088922

[47] Koopmans KP, Neels ON, Kema IP, Elsinga PH, Links TP, de Vries EGE, et al. Molecular imaging in neuroendocrine tumors: Molecular uptake mechanisms and clinical results. Crit Rev Oncol Hematol [Internet]. 2009 Sep;71(3):199–213. Available from: http://linkinghub.elsevier.com/retrieve/pii/S1040842809000493

[48] Sanli Y, Garg I, Kandathil A, Kendi T, Zanetti MJB, Kuyumcu S, et al. Neuroendocrine Tumor Diagnosis and Management: 68 Ga-DOTATATE PET/CT. Am J Roentgenol [Internet]. 2018 Aug;211(2):267–77. Available from: https://www.ajronline.org/doi/10.2214/AJR.18.19881

[49] Ambrosini V, Campana D, Tomassetti P, Fanti S. 68Ga-labelled peptides for diagnosis of gastroenteropancreatic NET. Eur J Nucl Med Mol Imaging [Internet]. 2012 Feb 3;39(S1):52–60. Available from: http://link.springer.com/10.1007/s00259-011-1989-4

[50] Menda Y, O'Dorisio TM, Howe JR, Schultz M, Dillon JS, Dick D, et al. Localization of Unknown Primary Site with 68 Ga-DOTATOC PET/CT in Patients with Metastatic Neuroendocrine Tumor. J Nucl Med [Internet]. 2017 Jul;58(7):1054–7. Available from: http://jnm.snmjournals.org/lookup/doi/10.2967/jnumed.116.180984

[51] Gabriel M, Decristoforo C, Kendler D, Dobrozemsky G, Heute D, Uprimny C, et al. 68Ga-DOTA-Tyr3-Octreotide PET in Neuroendocrine Tumors: Comparison with Somatostatin Receptor Scintigraphy and CT. J Nucl Med [Internet]. 2007 Apr 1;48(4):508–18. Available from: http://jnm.snmjournals.org/cgi/doi/10.2967/jnumed.106.035667

[52] Pettinato C, Sarnelli A, Di Donna M, Civollani S, Nanni C, Montini G, et al. 68Ga-DOTANOC: Biodistribution and dosimetry in patients affected by neuroendocrine tumors. Eur J Nucl Med Mol Imaging. 2008;35(1):72–9.

[53] Delle Fave G, O''Toole D, Sundin A, Taal B, Ferolla P, Ramage JK, et al. ENETS Consensus Guidelines Update for Gastroduodenal Neuroendocrine Neoplasms. Neuroendocrinology [Internet]. 2016;103(2):119–24. Available from: https://www.karger.com/Article/FullText/443168

[54] Plöckinger U, Rindi G, Arnold R, Eriksson B, Krenning EP, de Herder WW, et al. Guidelines for the Diagnosis and Treatment of Neuroendocrine Gastrointestinal Tumours. Neuroendocrinology [Internet]. 2004;80(6):394–424. Available from: http://www.karger.com/doi/10.1159/000085237

[55] NORTON J. Surgery for Primary Pancreatic Neuroendocrine Tumors. J Gastrointest Surg [Internet]. 2006 Mar;10(3):327–31. Available from: http://linkinghub.elsevier.com/retrieve/pii/S1091255X05006554

[56] Zerbi A, Capitanio V, Boninsegna L, Pasquali C, Rindi G, Delle Fave G, et al. Surgical treatment of pancreatic endocrine tumours in Italy: results of a prospective multicentre study of 262 cases. Langenbeck's Arch Surg [Internet]. 2011 Mar 21;396(3):313–21. Available from: http://link.springer.com/10.1007/s00423-010-0712-4

[57] Modlin IM, Latich I, Kidd M, Zikusoka M, Eick G. Therapeutic Options for Gastrointestinal Carcinoids. Clin Gastroenterol Hepatol. 2006;4(5):526–47.

[58] Keutgen XM, Nilubol N, Glanville J, Sadowski SM, Liewehr DJ, Venzon DJ, et al. Resection of primary tumor site is associated with prolonged survival in metastatic nonfunctioning pancreatic neuroendocrine tumors. Surgery [Internet]. 2016 Jan;159(1):311–9. Available from: https://linkinghub.elsevier.com/retrieve/pii/S0039606015007023

[59] Sarmiento JM, Heywood G, Rubin J, Ilstrup DM, Nagorney DM, Que FG. Surgical treatment of neuroendocrine metastases to the liver. J Am Coll Surg [Internet]. 2003 Jul;197(1):29–37. Available from: http://linkinghub.elsevier.com/retrieve/pii/S1072751503002308

[60] Birnbaum DJ, Turrini O, Vigano L, Russolillo N, Autret A, Moutardier V, et al. Surgical Management of Advanced Pancreatic Neuroendocrine Tumors: Short-Term and Long-Term Results from an International Multi-institutional Study. Ann Surg Oncol [Internet]. 2015 Mar 5;22(3):1000–7. Available from: http://link.springer.com/10.1245/s10434-014-4016-8

[61] Chen H, Hardacre JM, Uzar A, Cameron JL, Choti MA. Isolated liver metastases from neuroendocrine tumors: does resection prolong survival? J Am Coll Surg [Internet]. 1998 Jul;187(1):88–92. Available from:

http://linkinghub.elsevier.com/retrieve/pii/S1072751598000994

[62] Capurso G, Bettini R, Rinzivillo M, Boninsegna L, Delle Fave G, Falconi M. Role of Resection of the Primary Pancreatic Neuroendocrine Tumour Only in Patients with Unresectable Metastatic Liver Disease: A Systematic Review. Neuroendocrinology [Internet]. 2011;93(4):223–9. Available from: https://www.karger.com/Article/FullText/324770

[63] Riihimäki M, Hemminki A, Sundquist K, Sundquist J, Hemminki K. The epidemiology of metastases in neuroendocrine tumors. Int J Cancer [Internet]. 2016 Dec 15;139(12):2679–86. Available from: http://doi.wiley.com/10.1002/ijc.30400

[64] Del Prete M, Fiore F, Modica R, Marotta V, Marciello F, Ramundo V, et al. Hepatic arterial embolization in patients with neuroendocrine tumors. J Exp Clin Cancer Res [Internet]. 2014;33(1):43. Available from: http://jeccr.biomedcentral.com/articles/10.1186/1756-9966-33-43

[65] Peker A, Cicek O, Soydal C, Kucuk NO, Bilgic S. Radioembolization with yttrium-90 resin microspheres for neuroendocrine tumor liver metastases. Diagnostic Interv Radiol [Internet]. 2015 Jan 6;21(1):54–9. Available from: http://www.dirjournal.org/sayilar/73/buyuk/54-59.pdf

[66] Lee E, Leon Pachter H, Sarpel U. Hepatic Arterial Embolization for the Treatment of Metastatic Neuroendocrine Tumors. Int J Hepatol [Internet]. 2012;2012:1–8. Available from: http://www.hindawi.com/journals/ijh/2012/471203/

[67] Fan KY, Wild AT, Halappa VG, Kumar R, Ellsworth S, Ziegler M, et al. Neuroendocrine tumor liver metastases treated with yttrium-90 radioembolization. Contemp Clin Trials [Internet]. 2016 Sep;50:143–9. Available from:

https://linkinghub.elsevier.com/retrieve/pii/S1551714416301987

[68] Strosberg JR, Cheema A, Kvols LK. A Review of systemic and liver-directed therapies for metastatic neuroendocrine tumors of the gastroenteropancreatic tract. Cancer Control. 2011 Apr;18(2):127–37.

[69] Wolin EM. The expanding role of somatostatin analogs in the management of neuroendocrine tumors. Gastrointest Cancer Res [Internet]. 2012 Sep;5(5):161–8. Available from: http://www.ncbi.nlm.nih.gov/pubmed/23112884

[70] Caplin ME, Pavel M, Ćwikła JB, Phan AT, Raderer M, Sedláčková E, et al. Lanreotide in Metastatic Enteropancreatic Neuroendocrine Tumors. N Engl J Med [Internet]. 2014 Jul 17;371(3):224–33. Available from: http://www.nejm.org/doi/10.1056/NEJMoa1316158

[71] Öberg K, Eriksson B. Endocrine tumours of the pancreas. Best Pract Res Clin Gastreoenterology. 2005;19(5):753–81.

[72] Valkema R, De Jong M, Bakker WH, Breeman WAP, Kooij PPM, Lugtenburg PJ, et al. Phase I Study of Peptide Receptor Radionuclide Therapy With [lllIn-DTPA~ The Rotterdam Experience. Semin Nucl Med. 2002;32(2):110–22.

[73] Anthony LB, Woltering EA, Espenan GD, Cronin MD, Maloney TJ, McCarthy KE. Indium-111-pentetreotide prolongs survival in gastroenteropancreatic malignancies. Semin Nucl Med [Internet]. 2002;32(2):123–32. Available from: http://www.sciencedirect.com/science/article/pii/S0001299802800307

[74] Kwekkeboom DJ, de Herder WW, Krenning EP. Somatostatin Receptor-Targeted Radionuclide Therapy in Patients with Gastroenteropancreatic Neuroendocrine Tumors. Endocrinol Metab Clin North Am [Internet]. 2011;40(1):173–85. Available from: http://dx.doi.org/10.1016/j.ecl.2010.12.003

[75] Nicolas G, Giovacchini G, Müller-Brand J, Forrer F. Targeted Radiotherapy with Radiolabeled Somatostatin Analogs. Endocrinol Metab Clin North Am [Internet]. 2011;40(1):187–204. Available from: http://dx.doi.org/10.1016/j.ecl.2010.12.006

[76] Sabet A, Dautzenberg K, Haslerud T, Aouf A, Sabet A, Simon B, et al. Specific efficacy of peptide receptor radionuclide therapy with 177Lu-octreotate in advanced neuroendocrine tumours of the small intestine. Eur J Nucl Med Mol Imaging [Internet]. 2015 Jul 26;42(8):1238–46. Available from: http://link.springer.com/10.1007/s00259-015-3041-6

[77] Imhof A, Brunner P, Marincek N, Briel M, Schindler C, Rasch H, et al. Response, Survival, and Long-Term Toxicity After Therapy With the Radiolabeled Somatostatin Analogue [90 Y-DOTA]-TOC in Metastasized Neuroendocrine Cancers. J Clin Oncol [Internet]. 2011 Jun 10;29(17):2416–23. Available from: http://ascopubs.org/doi/10.1200/JCO.2010.33.7873

[78] Kong G, Grozinsky-Glasberg S, Hofman MS, Akhurst T, Meirovitz A, Maimon O, et al. Highly favourable outcomes with peptide receptor radionuclide therapy (PRRT) for metastatic rectal neuroendocrine neoplasia (NEN). Eur J Nucl Med Mol Imaging [Internet]. 2018 Oct 20; Available from: http://link.springer.com/10.1007/s00259-018-4196-8

[79] Hörsch D, Ezziddin S, Haug A, Gratz KF, Dunkelmann S, Miederer M, et al. Effectiveness and side-effects of peptide receptor radionuclide therapy for neuroendocrine neoplasms in Germany: A multi-institutional registry study with prospective follow-up. Eur J Cancer [Internet]. 2016 May;58:41–51. Available from: https://linkinghub.elsevier.com/retrieve/pii/S0959804916000472

[80] Bodei L, Cremonesi M, Grana CM, Fazio N, Iodice S, Baio SM, et al. Peptide receptor radionuclide therapy with 177Lu-DOTATATE: The IEO phase I-II study. Eur J Nucl Med Mol Imaging. 2011;38(12):2125–35.

[81] Bodei L, Kwekkeboom DJ, Kidd M, Modlin IM, Krenning EP. Radiolabeled Somatostatin Analogue Therapy Of Gastroenteropancreatic Cancer. Semin Nucl Med [Internet]. 2016;46(3):225–38. Available from: http://www.sciencedirect.com/science/article/pii/S000129981500152X

[82] Kesavan M, Turner JH. Myelotoxicity of Peptide Receptor Radionuclide Therapy of Neuroendocrine Tumors: A Decade of Experience. Cancer Biother Radiopharm [Internet]. 2016 Aug;31(6):189–98. Available from: http://www.liebertpub.com/doi/10.1089/cbr.2016.2035

[83] Strosberg J, El-Haddad G, Wolin E, Hendifar A, Yao J, Chasen B, et al. Phase 3 Trial of 177 Lu-Dotatate for Midgut Neuroendocrine Tumors. N Engl J Med [Internet]. 2017 Jan 12;376(2):125–35. Available from: http://www.nejm.org/doi/10.1056/NEJMoa1607427

[84] Kam BLR, Teunissen JJM, Krenning EP, De Herder WW, Khan S, Van Vliet EI, et al. Lutetium-labelled peptides for therapy of neuroendocrine tumours. Eur J Nucl Med Mol Imaging. 2012;39(SUPPL.1).

[85] Yeong C-H, Cheng M, Ng K-H. Therapeutic radionuclides in nuclear medicine: current and future prospects. J Zhejiang Univ Sci B [Internet]. 2014 Oct 16;15(10):845–63. Available from: http://link.springer.com/10.1631/jzus.B1400131

[86] Ersahin D, Doddamane I, Cheng D. Targeted radionuclide therapy. Cancers (Basel). 2011;3(4):3838–55.

[87] Williams LE, DeNardo GL, Meredith RF. Targeted radionuclide therapy. Med Phys

[Internet]. 2008 Jun 12;35(7Part1):3062–8. Available from: http://doi.wiley.com/10.1118/1.2938520

[88] Gudkov S, Shilyagina N, Vodeneev V, Zvyagin A. Targeted Radionuclide Therapy of Human Tumors. Int J Mol Sci [Internet]. 2015 Dec 28;17(1):33. Available from: http://www.mdpi.com/1422-0067/17/1/33

[89] Zukotynski K, Jadvar H, Capala J, Fahey F. Targeted Radionuclide Therapy: Practical Applications and Future Prospects. Biomark Cancer [Internet]. 2016 Jan 18;8s2:BIC.S31804. Available from: http://journals.sagepub.com/doi/10.4137/BIC.S31804

[90] Gagnon K, Bénard F, Kovacs M, Ruth TJ, Schaffer P, Wilson JS, et al. Cyclotron production of 99mTc: Experimental measurement of the 100Mo(p,x)99Mo, 99mTc and 99gTc excitation functions from 8 to 18 MeV. Nucl Med Biol [Internet]. 2011 Aug;38(6):907–16. Available from: http://linkinghub.elsevier.com/retrieve/pii/S0969805111000473

[91] Alexánderson E, Mannting F, Gómez-Martín D, Fermon S, Meave A. Technetium-99m-Sestamibi SPECT myocardial perfusion imaging in patients with complete left bundle branch block. Arch Med Res [Internet]. 2004 Mar;35(2):150–6. Available from: http://linkinghub.elsevier.com/retrieve/pii/S0188440903001462

[92] Choi CW, Lee DS, Chung JK, Lee MC, Kim NK, Choi KW, et al. Evaluation of bone metastases by Tc-99m MDP imaging in patients with stomach cancer. Clin Nucl Med [Internet]. 1995 Apr;20(4):310–4. Available from: http://www.ncbi.nlm.nih.gov/pubmed/7788986

[93] Ben-Haim S, Ell P. 18F-FDG PET and PET/CT in the Evaluation of Cancer Treatment

Response. J Nucl Med [Internet]. 2008 Dec 17;50(1):88–99. Available from: http://jnm.snmjournals.org/cgi/doi/10.2967/jnumed.108.054205

[94] Almuhaideb A, Papathanasiou N, Bomanji J. 18 F-FDG PET/CT imaging in oncology. Ann Saudi Med [Internet]. 2011;31(1):3. Available from: https://www.ncbi.nlm.nih.gov/pmc/articles/PMC3101722/

[95] Gerard SK, Cavalieri RR. I-123 diagnostic thyroid tumor whole-body scanning with imaging at 6, 24, and 48 hours. Clin Nucl Med [Internet]. 2002 Jan;27(1):1–8. Available from: http://www.ncbi.nlm.nih.gov/pubmed/11805475

[96] Jurić I, Fazlibegović E, Pravdić D, Starčević B, Punda A, Huić D, et al. The Significance of Thallium-201-Chloride SPECT Myocardial Perfusion Imaging in the Management of Patients With Stable Chronic Coronary Artery Disease. Clin Med Insights Cardiol [Internet]. 2018 Jan 23;12:117954681879056. Available from: http://journals.sagepub.com/doi/10.1177/1179546818790562

[97] Lazzeri E, Erba P, Perri M, Tascini C, Doria R, Giorgetti J, et al. Scintigraphic Imaging of Vertebral Osteomyelitis With 111In-Biotin. Spine (Phila Pa 1976) [Internet]. 2008 Apr;33(7):E198–204. Available from: https://insights.ovid.com/crossref?an=00007632-200804010-00028

[98] Even-Sapir E, Israel O. Gallium-67 scintigraphy: a cornerstone in functional imaging of lymphoma. Eur J Nucl Med Mol Imaging [Internet]. 2003 Jun 18;30(S1):S65–81. Available from: http://link.springer.com/10.1007/s00259-003-1164-7

[99] Mojtahedi A, Thamake S, Tworowska I, Ranganathan D, Delpassand ES. The value of (68)Ga-DOTATATE PET/CT in diagnosis and management of neuroendocrine tumors compared to current FDA approved imaging modalities: a review of literature. Am J Nucl

Med Mol Imaging [Internet]. 2014;4(5):426–34. Available from: http://www.ncbi.nlm.nih.gov/pubmed/25143861

[100] Wong JYC. Systemic targeted radionuclide therapy: Potential new areas. Int J Radiat Oncol [Internet]. 2006 Oct;66(2):S74–82. Available from: http://linkinghub.elsevier.com/retrieve/pii/S0360301605009399

[101] DeNardo SJ, DeNardo GL. Targeted radionuclide therapy for solid tumors: An overview. Int J Radiat Oncol [Internet]. 2006 Oct;66(2):S89–95. Available from: http://linkinghub.elsevier.com/retrieve/pii/S0360301606010327

[102] Lewandowski R, Salem R. Yttrium-90 Radioembolization of Hepatocellular Carcinoma and Metastatic Disease to the Liver. Semin Intervent Radiol [Internet]. 2006 Mar;23(1):064–72. Available from: http://www.thieme-connect.de/DOI/DOI?10.1055/s-2006-939842

[103] Hong CM, Kim C-Y, Son SH, Jung J, Lee C-H, Jeong JH, et al. I-131 biokinetics of remnant normal thyroid tissue and residual thyroid cancer in patients with differentiated thyroid cancer: comparison between recombinant human TSH administration and thyroid hormone withdrawal. Ann Nucl Med [Internet]. 2017 Oct 4;31(8):582–9. Available from: http://link.springer.com/10.1007/s12149-017-1188-x

[104] Brabander T, van der Zwan WA, Teunissen JJM, Kam BLR, Feelders RA, de Herder WW, et al. Long-Term Efficacy, Survival, and Safety of [177 Lu-DOTA 0 ,Tyr 3]octreotate in Patients with Gastroenteropancreatic and Bronchial Neuroendocrine Tumors. Clin Cancer Res [Internet]. 2017 Aug 15;23(16):4617–24. Available from: http://clincancerres.aacrjournals.org/lookup/doi/10.1158/1078-0432.CCR-16-2743

[105] Emmett L, Willowson K, Violet J, Shin J, Blanksby A, Lee J. Lutetium 177 PSMA

radionuclide therapy for men with prostate cancer: a review of the current literature and discussion of practical aspects of therapy. J Med Radiat Sci [Internet]. 2017 Mar;64(1):52–60. Available from: http://doi.wiley.com/10.1002/jmrs.227

[106] Parker C, Nilsson S, Heinrich D, Helle SI, O'Sullivan JM, Fosså SD, et al. Alpha Emitter Radium-223 and Survival in Metastatic Prostate Cancer. N Engl J Med [Internet]. 2013 Jul 18;369(3):213–23. Available from: http://www.nejm.org/doi/10.1056/NEJMoa1213755

[107] Jadvar H, Challa S, Quinn DI, Conti PS. One-Year Postapproval Clinical Experience with Radium-223 Dichloride in Patients with Metastatic Castrate-Resistant Prostate Cancer. Cancer Biother Radiopharm [Internet]. 2015 Jun;30(5):195–9. Available from: http://www.liebertpub.com/doi/10.1089/cbr.2014.1802

[108] Jadvar H. Targeted Radionuclide Therapy: An Evolution Toward Precision Cancer Treatment. Am J Roentgenol [Internet]. 2017 Aug;209(2):277–88. Available from: http://www.ajronline.org/doi/10.2214/AJR.17.18264

[109] Lee DY, Li KCP. Molecular Theranostics: A Primer for the Imaging Professional. Am J Roentgenol [Internet]. 2011 Aug;197(2):318–24. Available from: http://www.ajronline.org/doi/10.2214/AJR.11.6797

[110] Yordanova A, Eppard E, Kürpig S, Bundschuh R, Schönberger S, Gonzalez-Carmona M, et al. Theranostics in nuclear medicine practice. Onco Targets Ther [Internet]. 2017 Oct;Volume 10:4821–8. Available from: https://www.dovepress.com/theranostics-in-nuclear-medicine-practice-peer-reviewed-article-OTT

[111] Baum RP, Kulkarni HR. THERANOSTICS: From Molecular Imaging Using Ga-68 Labeled Tracers and PET/CT to Personalized Radionuclide Therapy - The Bad Berka

Experience. Theranostics [Internet]. 2012;2(5):437–47. Available from: http://www.thno.org/v02p0437.htm

[112] Nagarajah J, Janssen M, Hetkamp P, Jentzen W. Iodine Symporter Targeting with 124 I/ 131 I Theranostics. J Nucl Med [Internet]. 2017 Sep 1;58(Supplement 2):34S-38S. Available from: http://jnm.snmjournals.org/lookup/doi/10.2967/jnumed.116.186866

[113] Bailey DL, Willowson KP. An Evidence-Based Review of Quantitative SPECT Imaging and Potential Clinical Applications. J Nucl Med [Internet]. 2013;54(1):83–9. Available from: http://jnm.snmjournals.org/content/54/1/83%5Cnhttp://jnm.snmjournals.org/content/54/1/83.full.pdf%5Cnhttp://jnm.snmjournals.org/content/54/1/83.long%5Cnhttp://www.ncbi.nlm.nih.gov/pubmed/23283563

[114] Basu S, Zaidi H, Alavi A. Clinical and Research Applications of Quantitative PET Imaging. PET Clin [Internet]. 2007 Apr;2(2):161–72. Available from: http://linkinghub.elsevier.com/retrieve/pii/S1556859807000302

[115] Nakamoto R, Nakamoto Y, Ishimori T, Togashi K. Clinical Significance of Quantitative 123I-MIBG SPECT/CT Analysis of Pheochromocytoma and Paraganglioma. Clin Nucl Med [Internet]. 2016 Nov;41(11):e465–72. Available from: https://insights.ovid.com/crossref?an=00003072-201611000-00023

[116] Flux G, Bardies M, Monsieurs M, Savolainen S, Strands S-E, Lassmann M, et al. The impact of PET and SPECT on dosimetry for targeted radionuclide therapy. Z Med Phys [Internet]. 2006;16(1):47–59. Available from: http://www.ncbi.nlm.nih.gov/pubmed/16696370

[117] Li T, Ao ECI, Lambert B, Brans B, Vandenberghe S, Mok GSP. Quantitative Imaging for

Targeted Radionuclide Therapy Dosimetry - Technical Review. Theranostics [Internet]. 2017;7(18):4551–65. Available from: http://www.thno.org/v07p4551.htm

[118] Bailey DL, Willowson KP. Quantitative SPECT/CT: SPECT joins PET as a quantitative imaging modality. Eur J Nucl Med Mol Imaging. 2014;41(SUPPL. 1).

[119] Bruyant PP. Analytic and iterative reconstruction algorithms in SPECT. J Nucl Med [Internet]. 2002 Oct;43(10):1343–58. Available from: http://www.ncbi.nlm.nih.gov/pubmed/12368373

[120] Bruyant PP, Sau J, Mallet JJ. Streak artifact reduction in filtered backprojection using a level line-based interpolation method. J Nucl Med [Internet]. 2000 Nov;41(11):1913–9. Available from: http://www.ncbi.nlm.nih.gov/pubmed/11079504

[121] Vandenberghe S, D'Asseler Y, Van de Walle R, Kauppinen T, Koole M, Bouwens L, et al. Iterative reconstruction algorithms in nuclear medicine. Comput Med Imaging Graph [Internet]. 2001;25(2):105–11. Available from: http://www.ncbi.nlm.nih.gov/pubmed/11137786

[122] Shepp LA, Vardi Y. Maximum likelihood reconstruction for emission tomography. IEEE Trans Med Imaging [Internet]. 1982;1(2):113–22. Available from: http://www.ncbi.nlm.nih.gov/pubmed/18238264

[123] Hudson HM, Larkin RS. Accelerated image reconstruction using ordered subsets of projection data. IEEE Trans Med Imaging [Internet]. 1994;13(4):601–9. Available from: http://www.ncbi.nlm.nih.gov/pubmed/18218538

[124] Knoll P, Kotalova D, Köchle G, Kuzelka I, Minear G, Mirzaei S, et al. Comparison of advanced iterative reconstruction methods for SPECT/CT. Z Med Phys [Internet]. 2012 Feb;22(1):58–69. Available from:

https://linkinghub.elsevier.com/retrieve/pii/S0939388911000419

[125] Madsen MT. Recent Advances in SPECT Imaging. J Nucl Med [Internet]. 2007 Apr 1;48(4):661–73. Available from: http://jnm.snmjournals.org/cgi/doi/10.2967/jnumed.106.032680

[126] Conti M, Casey ME. Estimating the Optimal Iteration Number in Iterative Reconstruction : A Statistical Approach. 2007 IEEE Nucl Sci Symp Conf Rec. 2007;4389–94.

[127] Snyder DL, Miller MI. The Use of Sieves to Stabilize Images Produced with the EM Algorithm for Emission Tomography. IEEE Trans Nucl Sci [Internet]. 1985 Oct;32(5):3864–72. Available from: http://ieeexplore.ieee.org/document/4334521/

[128] Bailey DL. Transmission scanning in emission tomography. Eur J Nucl Med [Internet]. 1998 Jul;25(7):774–87. Available from: http://www.ncbi.nlm.nih.gov/pubmed/9662601

[129] Rowell NP, Glaholm J, Flower MA, Cronin B, McCready VR. Anatomically derived attenuation coefficients for use in quantitative single photon emission tomography studies of the thorax. Eur J Nucl Med [Internet]. 1992;19(1):36–40. Available from: http://www.ncbi.nlm.nih.gov/pubmed/1547806

[130] Hutton BF, Buvat I, Beekman FJ. Review and current status of SPECT scatter correction. Phys Med Biol [Internet]. 2011 Jul 21;56(14):R85–112. Available from: http://stacks.iop.org/0031-9155/56/i=14/a=R01?key=crossref.ec5977f7df97c11b1ab8d20d6ba94db0

[131] Narita Y, Eberl S, Iida H, Hutton BF, Braun M, Nakamura T, et al. Monte Carlo and experimental evaluation of accuracy and noise properties of two scatter correction methods for SPECT. Phys Med Biol [Internet]. 1996 Nov;41(11):2481–96. Available

from: http://www.ncbi.nlm.nih.gov/pubmed/8938040

[132] Asl MN, Sadremomtaz A, Bitarafan-Rajabi A. Evaluation of six scatter correction methods based on spectral analysis in (99m)Tc SPECT imaging using SIMIND Monte Carlo simulation. J Med Phys [Internet]. 2013 Oct;38(4):189–97. Available from: http://www.ncbi.nlm.nih.gov/pubmed/24672154

[133] Ljungberg M, King MA, Hademenos GJ, Strand SE. Comparison of four scatter correction methods using Monte Carlo simulated source distributions. J Nucl Med [Internet]. 1994 Jan;35(1):143–51. Available from: http://www.ncbi.nlm.nih.gov/pubmed/8271036

[134] Larsson A, Ljungberg M, Mo SJ, Riklund K, Johansson L. Correction for scatter and septal penetration using convolution subtraction methods and model-based compensation in 123 I brain SPECT imaging—a Monte Carlo study. Phys Med Biol [Internet]. 2006 Nov 21;51(22):5753–67. Available from: http://stacks.iop.org/0031-9155/51/i=22/a=003?key=crossref.7b006f1e73e0634f73a4b450b754322d

[135] Wells RG, Celler A, Harrop R. Analytical calculation of photon distributions in SPECT projections. IEEE Trans Nucl Sci [Internet]. 1998;45(6):3202–14. Available from: http://ieeexplore.ieee.org/document/736199/

[136] Xiao J, de Wit TC, Staelens SG, Beekman FJ. Evaluation of 3D Monte Carlo-based scatter correction for 99mTc cardiac perfusion SPECT. J Nucl Med [Internet]. 2006 Oct;47(10):1662–9. Available from: http://www.ncbi.nlm.nih.gov/pubmed/17015903

[137] Gaens M, Bert J, Pietrzyk U, Autret A, Shah N, Visvikis D. GPU-accelerated Monte Carlo based scatter correction in brain PET/MR. EJNMMI Phys [Internet]. 2014;1(Suppl 1):A32. Available from: http://ejnmmiphys.springeropen.com/articles/10.1186/2197-7364-1-S1-A32

[138] Cajgfinger T, Rit S, Létang JM, Halty A, Sarrut D. Fixed forced detection for fast SPECT Monte-Carlo simulation. Phys Med Biol [Internet]. 2018 Mar 2;63(5):055011. Available from: http://stacks.iop.org/0031-9155/63/i=5/a=055011?key=crossref.b0e52f3c079b2463ecf702c3c1db348b

[139] Sorenson JA. Deadtime characteristics of Anger cameras. J Nucl Med [Internet]. 1975 Apr;16(4):284–8. Available from: http://www.ncbi.nlm.nih.gov/pubmed/1113185

[140] Lee SH, Gardner RP, Jab M. Determination of dead times in the recently introduced Hybrid G-M Counter dead time model. J Nucl Sci Technol. 2004;41:156–9.

[141] Uribe CF, Esquinas PL, Gonzalez M, Zhao W, Tanguay J, Celler A. Deadtime effects in quantification of 177Lu activity for radionuclide therapy. EJNMMI Phys [Internet]. 2018 Jan 11;5(1):2. Available from: http://www.ncbi.nlm.nih.gov/pubmed/29322344

[142] Beauregard JM, Hofman MS, Pereira JM, Eu P, Hicks RJ. Quantitative 177Lu SPECT (QSPECT) imaging using a commercially available SPECT/CT system. Cancer Imaging. 2011;11(1):56–66.

[143] Celler A, Piwowarska-Bilska H, Shcherbinin S, Uribe C, Mikolajczak R, Birkenfeld B. Evaluation of dead-time corrections for post-radionuclide-therapy 177Lu quantitative imaging with low-energy high-resolution collimators. Nucl Med Commun [Internet]. 2014 Jan;35(1):73–87. Available from: http://content.wkhealth.com/linkback/openurl?sid=WKPTLP:landingpage&an=00006231-201401000-00009

[144] Frey EC, Tsui BMW. Collimator-Detector Response Compensation in SPECT. In: Quantitative Analysis in Nuclear Medicine Imaging [Internet]. Boston: Kluwer Academic Publishers; p. 141–66. Available from: http://link.springer.com/10.1007/0-387-25444-7_5

[145] Chun SY, Fessler JA, Dewaraja YK. Correction for Collimator-Detector Response in SPECT Using Point Spread Function Template. IEEE Trans Med Imaging [Internet]. 2013 Feb;32(2):295–305. Available from: http://ieeexplore.ieee.org/document/6332522/

[146] Gnesin S, Ferreira PL, Malterre J, Laub P, Prior JO, Verdun FR. Phantom Validation of Tc-99m Absolute Quantification in a SPECT / CT Commercial Device. 2016;2016.

[147] Liu H, Chan C, Grobshtein Y, Ma T, Liu Y, Wang S, et al. Anatomical-based partial volume correction for low-dose dedicated cardiac SPECT/CT. Phys Med Biol [Internet]. 2015 Sep 7;60(17):6751–73. Available from: http://stacks.iop.org/0031-9155/60/i=17/a=6751?key=crossref.c2f54f89ff413775c634096bcc5bf98d

[148] Pretorius PH, King MA. Diminishing the impact of the partial volume effect in cardiac SPECT perfusion imaging. Med Phys [Internet]. 2008 Dec 9;36(1):105–15. Available from: http://doi.wiley.com/10.1118/1.3031110

[149] Stabin MG, Tagesson M, Thomas SR, Ljungberg M, Strand SE. Radiation dosimetry in nuclear medicine. Appl Radiat Isot [Internet]. 1999 Jan;50(1):73–87. Available from: http://linkinghub.elsevier.com/retrieve/pii/S0969804398000232

[150] Howell RW, Wessels BW, Loevinger R, Watson EE, Bolch WE, Brill AB, et al. The MIRD perspective 1999. Medical Internal Radiation Dose Committee. J Nucl Med [Internet]. 1999 Jan;40(1):3S-10S. Available from: http://www.ncbi.nlm.nih.gov/pubmed/9935082

[151] Bolch WE, Eckerman KF, Sgouros G, Thomas SR. MIRD pamphlet No. 21: a generalized schema for radiopharmaceutical dosimetry--standardization of nomenclature. J Nucl Med. 2009;50(21):477–84.

[152] Dewaraja YK, Ljungberg M, Green AJ, Zanzonico PB, Frey EC, Bolch WE, et al. MIRD

pamphlet no. 24: Guidelines for quantitative 131I SPECT in dosimetry applications. J Nucl Med [Internet]. 2013;54(12):2182–8. Available from: http://www.pubmedcentral.nih.gov/articlerender.fcgi?artid=3970715&tool=pmcentrez&rendertype=abstract

[153] Siegel J a, Thomas SR, Stubbs JB, Stabin MG, Hays MT, Koral KF, et al. MIRD pamphlet no. 16: Techniques for quantitative radiopharmaceutical biodistribution data acquisition and analysis for use in human radiation dose estimates. J Nucl Med. 1999;40(2):37S-61S.

[154] Garkavij M, Nickel M, Sjögreen-Gleisner K, Ljungberg M, Ohlsson T, Wingårdh K, et al. 177Lu-[DOTA0,Tyr3] octreotate therapy in patients with disseminated neuroendocrine tumors: Analysis of dosimetry with impact on future therapeutic strategy. Cancer [Internet]. 2010 Feb 15 [cited 2016 Nov 5];116(SUPPL. 4):1084–92. Available from: http://doi.wiley.com/10.1002/cncr.24796

[155] Ljungberg M, Sjögreen Gleisner K. Personalized Dosimetry for Radionuclide Therapy Using Molecular Imaging Tools. Biomedicines [Internet]. 2016 Nov 15;4(4):25. Available from: http://www.mdpi.com/2227-9059/4/4/25

[156] Bin He, Wahl RL, Yong Du, Sgouros G, Jacene H, Flinn I, et al. Comparison of Residence Time Estimation Methods for Radioimmunotherapy Dosimetry and Treatment Planning—Monte Carlo Simulation Studies. IEEE Trans Med Imaging [Internet]. 2008 Apr;27(4):521–30. Available from: http://ieeexplore.ieee.org/document/4359074/

[157] Cheng L, Hobbs RF, Segars PW, Sgouros G, Frey EC. Improved dose–volume histogram estimates for radiopharmaceutical therapy by optimizing quantitative SPECT reconstruction parameters. Phys Med Biol [Internet]. 2013 Jun 7;58(11):3631–47.

Available from: http://stacks.iop.org/0031-9155/58/i=11/a=3631?key=crossref.5cf8f8566429a1855e4bad8d3874b9e3

[158] Stabin MG, Sparks RB, Crowe E. OLINDA/EXM: the second-generation personal computer software for internal dose assessment in nuclear medicine. J Nucl Med [Internet]. 2005 Jun;46(6):1023–7. Available from: http://www.ncbi.nlm.nih.gov/pubmed/15937315

[159] Andersson M, Johansson L, Minarik D, Mattsson S, Leide-Svegborn S. An internal radiation dosimetry computer program, IDAC 2.0, for estimation of patient doses from radiopharmaceuticals. Radiat Prot Dosimetry [Internet]. 2014 Dec 1;162(3):299–305. Available from: https://academic.oup.com/rpd/article-lookup/doi/10.1093/rpd/nct337

[160] Andersson M, Johansson L, Eckerman K, Mattsson S. IDAC-Dose 2.1, an internal dosimetry program for diagnostic nuclear medicine based on the ICRP adult reference voxel phantoms. EJNMMI Res [Internet]. 2017 Dec 3;7(1):88. Available from: http://ejnmmires.springeropen.com/articles/10.1186/s13550-017-0339-3

[161] Bolch WE, Bouchet LG, Robertson JS, Wessels BW, Siegel J a, Howell RW, et al. MIRD pamphlet No. 17: the dosimetry of nonuniform activity distributions--radionuclide S values at the voxel level. Medical Internal Radiation Dose Committee. J Nucl Med [Internet]. 1999 Jan;40(1):11S-36S. Available from: http://www.ncbi.nlm.nih.gov/pubmed/9935083

[162] Kwok CS, Irfan M, Woo MK, Prestwich W V. Effect of tissue inhomogeneity on beta dose distribution of 3 2 P. Med Phys [Internet]. 1987 Jan;14(1):98–104. Available from: http://doi.wiley.com/10.1118/1.596112

[163] Goorley T, James M, Booth T, Brown F, Bull J, Cox LJ, et al. Initial MCNP6 Release

Overview. Nucl Technol [Internet]. 2012 Dec 10;180(3):298–315. Available from: https://www.tandfonline.com/doi/full/10.13182/NT11-135

[164] Jan S, Santin G, Strul D, Staelens S, Assié K, Autret D, et al. GATE: a simulation toolkit for PET and SPECT. Phys Med Biol [Internet]. 2004 Oct 7;49(19):4543. Available from: http://stacks.iop.org/0031-9155/49/i=19/a=007%5Cnhttp://iopscience.iop.org/article/10.1088/0031-9155/49/19/007/meta;jsessionid=135175900B482C9162F569FC7E53B5A1.c3.iopscience.cld.iop.org/pdf

[165] Shcherbinin S, Piwowarska-Bilska H, Celler A, Birkenfeld B. Quantitative SPECT/CT reconstruction for 177 Lu and 177 Lu/ 90 Y targeted radionuclide therapies. Phys Med Biol [Internet]. 2012 Sep 21;57(18):5733–47. Available from: http://stacks.iop.org/0031-9155/57/i=18/a=5733?key=crossref.99b3f9bfb9b6a23841bdfde2578069f8

[166] Mezzenga E, D'Errico V, D'Arienzo M, Strigari L, Panagiota K, Matteucci F, et al. Quantitative accuracy of 177Lu SPECT imaging for molecular radiotherapy. Chen C-T, editor. PLoS One [Internet]. 2017 Aug 14;12(8):e0182888. Available from: https://dx.plos.org/10.1371/journal.pone.0182888

[167] Kondev FG. Nuclear Data Sheets for A = 177. Nucl Data Sheets [Internet]. 2003;98(03):801–1095. Available from: http://linkinghub.elsevier.com/retrieve/pii/S0090375203900068

[168] Zhernosekov KP, Perego RC, Dvorakova Z, Henkelmann R, Türler A. Target burn-up corrected specific activity of 177Lu produced via 176Lu(n, γ) 177Lu nuclear reactions. Appl Radiat Isot [Internet]. 2008 Sep;66(9):1218–20. Available from: https://linkinghub.elsevier.com/retrieve/pii/S0969804308001280

[169] Chakraborty S, Vimalnath K V., Lohar SP, Shetty P, Dash A. On the practical aspects of large-scale production of 177Lu for peptide receptor radionuclide therapy using direct neutron activation of 176Lu in a medium flux research reactor: the Indian experience. J Radioanal Nucl Chem [Internet]. 2014 Oct 29;302(1):233–43. Available from: http://link.springer.com/10.1007/s10967-014-3169-z

[170] Pillai MRA, Chakraborty S, Das T, Venkatesh M, Ramamoorthy N. Production logistics of 177Lu for radionuclide therapy. Appl Radiat Isot [Internet]. 2003 Aug;59(2–3):109–18. Available from: http://linkinghub.elsevier.com/retrieve/pii/S0969804303001581

[171] Dash A, Pillai MRA, Knapp FF. Production of 177Lu for Targeted Radionuclide Therapy: Available Options. Nucl Med Mol Imaging (2010) [Internet]. 2015 Jun 17;49(2):85–107. Available from: http://link.springer.com/10.1007/s13139-014-0315-z

[172] Dash A, Chakravarty R, Knapp FFR, Pillai AMR. Indirect Production of No Carrier Added (NCA) (177)Lu from Irradiation of Enriched (176)Yb: Options for Ytterbium/Lutetium Separation. Curr Radiopharm [Internet]. 2015;8(2):107–18. Available from: http://www.ncbi.nlm.nih.gov/pubmed/25771377

[173] Mikolajczak R, Parus JL, Pawlak D, Zakrzewska E, Michalak W, Sasinowska I. Reactor produced 177Lu of specific activity and purity suitable for medical applications. J Radioanal Nucl Chem. 2003;257(1):53–7.

[174] Manenti S, Groppi F, Gandini A, Gini L, Abbas K, Holzwarth U, et al. Excitation function for deuteron induced nuclear reactions on natural ytterbium for production of high specific activity 177gLu in no-carrier-added form for metabolic radiotherapy. Appl Radiat Isot [Internet]. 2011 Jan;69(1):37–45. Available from: https://linkinghub.elsevier.com/retrieve/pii/S0969804310003283

[175] Manenti S, Bonardi ML, Gini L, Groppi F. Physical optimization of production by deuteron irradiation of high specific activity 177gLu suitable for radioimmunotherapy. Nucl Med Biol [Internet]. 2014 May;41(5):407–9. Available from: https://linkinghub.elsevier.com/retrieve/pii/S0969805114000481

[176] Tárkányi F, Ditrói F, Takács S, Hermanne A, Yamazaki H, Baba M, et al. Activation cross-sections of longer lived products of deuteron induced nuclear reactions on ytterbium up to 40MeV. Nucl Instruments Methods Phys Res Sect B Beam Interact with Mater Atoms [Internet]. 2013 Jun;304:36–48. Available from: https://linkinghub.elsevier.com/retrieve/pii/S0168583X13003911

[177] Cremonesi M, Ferrari M, Bodei L, Tosi G, Paganelli G. Dosimetry in Peptide radionuclide receptor therapy: a review. J Nucl Med [Internet]. 2006 Sep;47(9):1467–75. Available from: http://www.ncbi.nlm.nih.gov/pubmed/16954555

[178] Banerjee S, Pillai MRA, Knapp FF (Russ). Lutetium-177 Therapeutic Radiopharmaceuticals: Linking Chemistry, Radiochemistry, and Practical Applications. Chem Rev [Internet]. 2015 Apr 22;115(8):2934–74. Available from: http://pubs.acs.org/doi/10.1021/cr500171e

[179] Bodei L, Cwikla JB, Kidd M, Modlin IM. The role of peptide receptor radionuclide therapy in advanced/metastatic thoracic neuroendocrine tumors. J Thorac Dis. 2017 Nov;9(S15):S1511–23.

[180] Ando A, Ando I, Tonami N, Kinuya S, Kazuma K, Kataiwa A, et al. 177Lu-EDTMP: a potential therapeutic bone agent. Nucl Med Commun [Internet]. 1998 Jun;19(6):587–91. Available from: http://www.ncbi.nlm.nih.gov/pubmed/10234664

[181] Thapa P, Nikam D, Das T, Sonawane G, Agarwal JP, Basu S. Clinical Efficacy and Safety

Comparison of 177Lu-EDTMP with 153Sm-EDTMP on an Equidose Basis in Patients with Painful Skeletal Metastases. J Nucl Med [Internet]. 2015 Oct 1;56(10):1513–9. Available from: http://jnm.snmjournals.org/cgi/doi/10.2967/jnumed.115.155762

[182] Mazzarri S, Guidoccio F, Mariani G. The emerging potential of 177Lu-EDTMP: an attractive novel option for radiometabolic therapy of skeletal metastases. Clin Transl Imaging [Internet]. 2015 Apr 22;3(2):167–8. Available from: http://link.springer.com/10.1007/s40336-015-0099-x

[183] Alavi M, Omidvari S, Mehdizadeh A, Jalilian A, Bahrami-Samani A. Metastatic Bone Pain Palliation using 177 Lu-Ethylenediaminetetramethylene Phosphonic Acid. World J Nucl Med [Internet]. 2015;14(2):109. Available from: http://www.wjnm.org/text.asp?2015/14/2/109/157124

[184] Yuan J, Liu C, Liu X, Wang Y, Kuai D, Zhang G, et al. Efficacy and Safety of 177Lu-EDTMP in Bone Metastatic Pain Palliation in Breast Cancer and Hormone Refractory Prostate Cancer. Clin Nucl Med [Internet]. 2013 Feb;38(2):88–92. Available from: http://content.wkhealth.com/linkback/openurl?sid=WKPTLP:landingpage&an=00003072-201302000-00002

[185] Ehlerding EB, Lacognata S, Jiang D, Ferreira CA, Goel S, Hernandez R, et al. Targeting angiogenesis for radioimmunotherapy with a 177Lu-labeled antibody. Eur J Nucl Med Mol Imaging [Internet]. 2018 Jan 18;45(1):123–31. Available from: http://link.springer.com/10.1007/s00259-017-3793-2

[186] Bhusari P, Vatsa R, Singh G, Parmar M, Bal A, Dhawan DK, et al. Development of Lu-177-trastuzumab for radioimmunotherapy of HER2 expressing breast cancer and its feasibility assessment in breast cancer patients. Int J Cancer [Internet]. 2017 Feb

15;140(4):938–47. Available from: http://doi.wiley.com/10.1002/ijc.30500

[187] Stillebroer AB, Boerman OC, Desar IME, Boers-Sonderen MJ, van Herpen CML, Langenhuijsen JF, et al. Phase 1 Radioimmunotherapy Study with Lutetium 177–labeled Anti-Carbonic Anhydrase IX Monoclonal Antibody Girentuximab in Patients with Advanced Renal Cell Carcinoma. Eur Urol [Internet]. 2013 Sep;64(3):478–85. Available from: https://linkinghub.elsevier.com/retrieve/pii/S0302283812009591

[188] Cheal SM, Xu H, Guo H, Lee S, Punzalan B, Chalasani S, et al. Theranostic pretargeted radioimmunotherapy of colorectal cancer xenografts in mice using picomolar affinity 86Y- or 177Lu-DOTA-Bn binding scFv C825/GPA33 IgG bispecific immunoconjugates. Eur J Nucl Med Mol Imaging [Internet]. 2016 May 24;43(5):925–37. Available from: http://link.springer.com/10.1007/s00259-015-3254-8

[189] Kratochwil C, Giesel FL, Stefanova M, Bene ova M, Bronzel M, Afshar-Oromieh A, et al. PSMA-Targeted Radionuclide Therapy of Metastatic Castration-Resistant Prostate Cancer with 177Lu-Labeled PSMA-617. J Nucl Med [Internet]. 2016 Aug 1;57(8):1170–6. Available from: http://jnm.snmjournals.org/cgi/doi/10.2967/jnumed.115.171397

[190] Baum RP, Kulkarni HR, Schuchardt C, Singh A, Wirtz M, Wiessalla S, et al. 177Lu-Labeled Prostate-Specific Membrane Antigen Radioligand Therapy of Metastatic Castration-Resistant Prostate Cancer: Safety and Efficacy. J Nucl Med [Internet]. 2016 Jul 1;57(7):1006–13. Available from: http://jnm.snmjournals.org/cgi/doi/10.2967/jnumed.115.168443

[191] Rahbar K, Ahmadzadehfar H, Kratochwil C, Haberkorn U, Schäfers M, Essler M, et al. German Multicenter Study Investigating 177 Lu-PSMA-617 Radioligand Therapy in Advanced Prostate Cancer Patients. J Nucl Med [Internet]. 2017 Jan;58(1):85–90.

Available from: http://jnm.snmjournals.org/lookup/doi/10.2967/jnumed.116.183194

[192] Hofman MS, Violet J, Hicks RJ, Ferdinandus J, Ping Thang S, Akhurst T, et al. [177Lu]-PSMA-617 radionuclide treatment in patients with metastatic castration-resistant prostate cancer (LuPSMA trial): a single-centre, single-arm, phase 2 study. Lancet Oncol. 2018 Jun;19(6):825–33.

[193] Zang J, Fan X, Wang H, Liu Q, Wang J, Li H, et al. First-in-human study of 177Lu-EB-PSMA-617 in patients with metastatic castration-resistant prostate cancer. European Journal of Nuclear Medicine and Molecular Imaging. 2018 Jan;148–58.

[194] Frey EC, Humm JL, Ljungberg M. Accuracy and precision of radioactivity quantification in nuclear medicine images. Semin Nucl Med [Internet]. 2012;42(3):208–18. Available from: http://dx.doi.org/10.1053/j.semnuclmed.2011.11.003

[195] Da Silva a J, Tang HR, Wong KH, Wu MC, Dae MW, Hasegawa BH. Absolute quantification of regional myocardial uptake of 99mTc-sestamibi with SPECT: experimental validation in a porcine model. J Nucl Med. 2001;42(5):772–9.

[196] Ohno Y, Koyama H, Nogami M, Takenaka D, Matsumoto S, Yoshimura M, et al. Postoperative lung function in lung cancer patients: comparative analysis of predictive capability of MRI, CT, and SPECT. AJR Am J Roentgenol [Internet]. 2007;189(2):400–8. Available from: http://www.ncbi.nlm.nih.gov/pubmed/17646467

[197] Dewaraja YK, Frey EC, Sgouros G, Brill a B, Roberson P, Zanzonico PB, et al. MIRD pamphlet No. 23: quantitative SPECT for patient-specific 3-dimensional dosimetry in internal radionuclide therapy. J Nucl Med [Internet]. 2012;53(8):1310–25. Available from: http://www.pubmedcentral.nih.gov/articlerender.fcgi?artid=3465844&tool=pmcentrez&rendertype=abstract

[198] Strigari L, Konijnenberg M, Chiesa C, Bardies M, Du Y, Gleisner KS, et al. The evidence base for the use of internal dosimetry in the clinical practice of molecular radiotherapy. Eur J Nucl Med Mol Imaging [Internet]. 2014 Oct 11;41(10):1976–88. Available from: http://link.springer.com/10.1007/s00259-014-2824-5

[199] Ritt P, Vija H, Hornegger J, Kuwert T. Absolute quantification in SPECT. Eur J Nucl Med Mol Imaging. 2011;38(SUPPL. 1).

[200] Seret A, Nguyen D, Bernard C. Quantitative capabilities of four state-of-the-art SPECT-CT cameras. EJNMMI Res [Internet]. 2012;2(1):45. Available from: http://ejnmmires.springeropen.com/articles/10.1186/2191-219X-2-45

[201] Erlandsson K, Buvat I, Pretorius PH, Thomas BA, Hutton BF. A review of partial volume correction techniques for emission tomography and their applications in neurology, cardiology and oncology. Phys Med Biol [Internet]. 2012;57(21):R119–59. Available from: http://stacks.iop.org/0031-9155/57/i=21/a=R119?key=crossref.4613f99a63010e4337b3a316357415db

[202] Sanders JC, Kuwert T, Hornegger J, Ritt P. Quantitative SPECT/CT Imaging of 177Lu with In Vivo Validation in Patients Undergoing Peptide Receptor Radionuclide Therapy. Mol Imaging Biol. 2015;17(4):585–93.

[203] Hippeläinen E, Tenhunen M, Mäenpää H, Sohlberg A. Quantitative accuracy of (177)Lu SPECT reconstruction using different compensation methods: phantom and patient studies. EJNMMI Res [Internet]. 2016;6(1):16. Available from: http://www.pubmedcentral.nih.gov/articlerender.fcgi?artid=4759452&tool=pmcentrez&rendertype=abstract

[204] Willowson K, Bailey DL, Baldock C. Quantitative SPECT reconstruction using CT-

derived corrections. Phys Med Biol [Internet]. 2008;53(12):3099–112. Available from: http://www.ncbi.nlm.nih.gov/pubmed/18495976

[205] He B, Du Y, Song X, Segars WP, Frey EC. A Monte Carlo and physical phantom evaluation of quantitative In-111 SPECT. Phys Med Biol. 2005;50(17):4169–85.

[206] Wit TC de, Xiao J, Nijsen JFW, Schip FD van het, Staelens SG, Rijk PP van, et al. Hybrid scatter correction applied to quantitative holmium-166 SPECT. Phys Med Biol [Internet]. 2006 Oct 7;51(19):4773–87. Available from: http://stacks.iop.org/0031-9155/51/i=19/a=004?key=crossref.228d52ea80a4056b0cbda9790645d13a

[207] Shcherbinin S, Grimes J, Bator a, Cwikla JB, Celler A. Three-dimensional personalized dosimetry for (188)Re liver selective internal radiation therapy based on quantitative post-treatment SPECT studies. Phys Med Biol [Internet]. 2013 Jan 6;59(1):119–34. Available from: http://www.ncbi.nlm.nih.gov/pubmed/24334821

[208] Anizan N, Wang H, Zhou XC, Hobbs RF, Wahl RL, Frey EC. Factors affecting the stability and repeatability of gamma camera calibration for quantitative imaging applications based on a retrospective review of clinical data. EJNMMI Res [Internet]. 2014;4(1):1–11. Available from: http://www.ejnmmires.com/content/4/1/67

[209] Pacilio M, Cassano B, Pellegrini R, Di Castro E, Zorz A, De Vincentis G, et al. Gamma camera calibrations for the Italian multicentre study for lesion dosimetry in 223Ra therapy of bone metastases. Phys Medica [Internet]. 2017;41:117–23. Available from: http://dx.doi.org/10.1016/j.ejmp.2017.04.019

[210] Zeintl J, Vija AH, Yahil A, Hornegger J, Kuwert T. Quantitative accuracy of clinical 99mTc SPECT/CT using ordered-subset expectation maximization with 3-dimensional resolution recovery, attenuation, and scatter correction. J Nucl Med [Internet].

2010;51(6):921–8. Available from: http://www.ncbi.nlm.nih.gov/pubmed/20484423

[211] Koral KF, Yendiki A, Lin Q, Dewaraja YK. Comparison of 3D OSEM vs 1D SAGE for focal total-activity quantification in I-131 SPECT with HE and UHE collimation. IEEE Trans Nuc Sci. 2005;52(1):154–8.

[212] McDougald WA, Miyaoka RS, Alessio AM, Harrison RL, Lewellen TK. A study of SPECT/CT camera stability for quantitative imaging. EJNMMI Phys [Internet]. 2016;3(1):14. Available from: http://ejnmmiphys.springeropen.com/articles/10.1186/s40658-016-0150-7

[213] Sandström M, Ilan E, Karlberg A, Johansson S, Freedman N, Garske-Román U. Method dependence, observer variability and kidney volumes in radiation dosimetry of (177)Lu-DOTATATE therapy in patients with neuroendocrine tumours. EJNMMI Phys [Internet]. 2015;2(1):24. Available from: http://www.ncbi.nlm.nih.gov/pubmed/26501825

[214] D'Arienzo M, Cozzella ML, Fazio A, De Felice P, Iaccarino G, D'Andrea M, et al. Quantitative 177Lu SPECT imaging using advanced correction algorithms in non-reference geometry. Phys Medica [Internet]. 2016;32(12):1745–52. Available from: http://dx.doi.org/10.1016/j.ejmp.2016.09.014

[215] Jan S, Benoit D, Becheva E, Carlier T, Cassol F, Descourt P, et al. GATE V6: a major enhancement of the GATE simulation platform enabling modelling of CT and radiotherapy. Phys Med Biol. 2011;56:881–901.

[216] Khazov Y, Mitropolsky I, Rodionov A. Nuclear Data Sheets for A = 131. Nucl Data Sheets. 2006;107(11):2715–930.

[217] Singh B. Nuclear Data Sheets for A = 188 *. Nucl Data Sheets [Internet]. 2002 Feb;387(2):387–541. Available from:

http://linkinghub.elsevier.com/retrieve/pii/S0090375211000445

[218] Uribe CF, Esquinas PL, Tanguay J, Gonzalez M, Gaudin E, Beauregard J-M, et al. Accuracy of 177Lu activity quantification in SPECT imaging: a phantom study. EJNMMI Phys [Internet]. 2017;4(1):2. Available from: http://ejnmmiphys.springeropen.com/articles/10.1186/s40658-016-0170-3

[219] Esquinas PL, Rodríguez-Rodríguez C, Carlos De La Vega J, Bokharaei M, Saatchi K, Shirmohammad M, et al. 188Re image performance assessment using small animal multi-pinhole SPECT/PET/CT system. Phys Medica [Internet]. 2016;33:26–37. Available from: http://dx.doi.org/10.1016/j.ejmp.2016.11.105

[220] Uribe CF, Esquinas PL, Gonzalez M, Celler A. Characteristics of Bremsstrahlung emissions of 177Lu, 188Re, and 90Y for SPECT/CT quantification in radionuclide therapy. Phys Medica [Internet]. 2016;32(5):691–700. Available from: http://dx.doi.org/10.1016/j.ejmp.2016.04.014

[221] Dewaraja YK, Wilderman SJ, Ljungberg M, Koral KF, Zasadny K, Kaminiski MS. Accurate dosimetry in 131I radionuclide therapy using patient-specific, 3-dimensional methods for SPECT reconstruction and absorbed dose calculation. J Nucl Med [Internet]. 2005;46(5):840–9. Available from: http://www.pubmedcentral.nih.gov/articlerender.fcgi?artid=2804106&tool=pmcentrez&rendertype=abstract

[222] Ogawa K, Harata Y, Ichihara T, Kubo A, Hashimoto S. A Practical Method for Position-Dependent Compton-Scatter Correction in Single Photon Emission CT. IEEE Trans Med Imaging. 1991;10(3):408–12.

[223] de Nijs R, Lagerburg V, Klausen TL, Holm S. Improving quantitative dosimetry in

177Lu-DOTATATE SPECT by energy window-based scatter corrections. Nucl Med Commun [Internet]. 2014;35(5):522–33. Available from: http://content.wkhealth.com/linkback/openurl?sid=WKPTLP:landingpage&an=00006231-201405000-00012

[224] Wevrett J, Fenwick A, Scuffham J, Nisbet A. Development of a calibration protocol for quantitative imaging for molecular radiotherapy dosimetry. Radiat Phys Chem [Internet]. 2017 Nov;140(November 2016):355–60. Available from: http://linkinghub.elsevier.com/retrieve/pii/S0969806X17302517

[225] Vija AH, Hawman EG, Engdahl JC. Analysis of a SPECT OSEM reconstruction method with 3D beam modeling and optional attenuation correction: phantom studies. In: 2003 IEEE Nuclear Science Symposium Conference Record (IEEE Cat No03CH37515) [Internet]. IEEE; 2003. p. 2662–6. Available from: http://ieeexplore.ieee.org/document/1352436/

[226] Marin G, Vanderlinden B, Karfis I, Guiot T, Wimana Z, Flamen P, et al. Accuracy and precision assessment for activity quantification in individualized dosimetry of 177Lu-DOTATATE therapy. EJNMMI Phys [Internet]. 2017 Dec;4(1):7. Available from: http://www.ncbi.nlm.nih.gov/pubmed/28127694

[227] Slomka PJ, Patton JA, Berman DS, Germano G. Advances in technical aspects of myocardial perfusion SPECT imaging. J Nucl Cardiol. 2009;16(2):255–76.

[228] Erdi YE, Wessels BW, Loew MH, Erdi AK. Threshold estimation in single photon emission computed tomography and planar imaging for clinical radioimmunotherapy. Cancer Res [Internet]. 1995 Dec 1;55(23 Suppl):5823s-5826s. Available from: http://www.ncbi.nlm.nih.gov/pubmed/7493353

[229] Grimes J, Celler A, Shcherbinin S, Piwowarska-Bilska H, Birkenfeld B. The accuracy and reproducibility of SPECT target volumes and activities estimated using an iterative adaptive thresholding technique. Nucl Med Commun [Internet]. 2012 Dec;33(12):1254–66. Available from: http://content.wkhealth.com/linkback/openurl?sid=WKPTLP:landingpage&an=00006231-201212000-00005

[230] Marks LB, Yorke ED, Jackson A, Ten Haken RK, Constine LS, Eisbruch A, et al. Use of Normal Tissue Complication Probability Models in the Clinic. Int J Radiat Oncol [Internet]. 2010 Mar;76(3):S10–9. Available from: https://linkinghub.elsevier.com/retrieve/pii/S036030160903288X

[231] Smith BD, Bellon JR, Blitzblau R, Freedman G, Haffty B, Hahn C, et al. Radiation therapy for the whole breast: Executive summary of an American Society for Radiation Oncology (ASTRO) evidence-based guideline. Pract Radiat Oncol [Internet]. 2018 May;8(3):145–52. Available from: https://linkinghub.elsevier.com/retrieve/pii/S1879850018300511

[232] Zaorsky NG, Palmer JD, Hurwitz MD, Keith SW, Dicker AP, Den RB. What is the ideal radiotherapy dose to treat prostate cancer? A meta-analysis of biologically equivalent dose escalation. Radiother Oncol [Internet]. 2015 Jun;115(3):295–300. Available from: https://linkinghub.elsevier.com/retrieve/pii/S0167814015002467

[233] Pajonk F, Vlashi E, McBride WH. Radiation Resistance of Cancer Stem Cells: The 4 R's of Radiobiology Revisited. Stem Cells [Internet]. 2010 Feb 4;28(4):639–48. Available from: http://doi.wiley.com/10.1002/stem.318

[234] Barendsen GW. Dose fractionation, dose rate and iso-effect relationships for normal tissue

responses. Int J Radiat Oncol Biol Phys. 1982 Nov;8(11):1981–97.

[235] Brenner DJ, Hall EJ. Fractionation and protraction for radiotherapy of prostate carcinoma. Int J Radiat Oncol. 1999 Mar;43(5):1095–101.

[236] Brenner DJ. The linear-quadratic model is an appropriate methodology for determining isoeffective doses at large doses per fraction. Semin Radiat Oncol. 2008 Oct;18(4):234–9.

[237] Jones L, Hoban P, Metcalfe P. The use of the linear quadratic model in radiotherapy: a review. Australas Phys Eng Sci Med. 2001 Sep;24(3):132–46.

[238] Brenner DJ, Hlatky LR, Hahnfeldt PJ, Huang Y, Sachs RK. The Linear-Quadratic Model and Most Other Common Radiobiological Models Result in Similar Predictions of Time-Dose Relationships. Radiat Res. 1998 Jul;150(1):83.

[239] Pouget J-P, Lozza C, Deshayes E, Boudousq V, Navarro-Teulon I. Introduction to Radiobiology of Targeted Radionuclide Therapy. Front Med. 2015 Mar;2.

[240] Melis M, Krenning EP, Bernard BF, Barone R, Visser TJ, de Jong M. Localisation and mechanism of renal retention of radiolabelled somatostatin analogues. Eur J Nucl Med Mol Imaging [Internet]. 2005 Oct;32(10):1136–43. Available from: http://www.ncbi.nlm.nih.gov/pubmed/15912401

[241] Del Prete M, Arsenault F, Saighi N, Zhao W, Buteau F, Celler A, et al. Accuracy and reproducibility of simplified QSPECT dosimetry for personalized 177Lu-octreotate PRRT. EJNMMI Phys [Internet]. 2018 Dec 15;5(1):25. Available from: https://ejnmmiphys.springeropen.com/articles/10.1186/s40658-018-0224-9

[242] Del Prete M, Buteau F-A, Beauregard J-M. Personalized 177Lu-octreotate peptide receptor radionuclide therapy of neuroendocrine tumours: a simulation study. Eur J Nucl Med Mol Imaging [Internet]. 2017;44(9):1490–500. Available from:

http://link.springer.com/10.1007/s00259-017-3688-2

[243] Zhao W, Esquinas PL, Hou X, Uribe CF, Gonzalez M, Beauregard J-M, et al. Determination of gamma camera calibration factors for quantitation of therapeutic radioisotopes. EJNMMI Phys [Internet]. 2018 Dec 2;5(1):8. Available from: https://ejnmmiphys.springeropen.com/articles/10.1186/s40658-018-0208-9

[244] Vegt E, Melis M, Eek A, de Visser M, Brom M, Oyen WJG, et al. Renal uptake of different radiolabelled peptides is mediated by megalin: SPECT and biodistribution studies in megalin-deficient mice. Eur J Nucl Med Mol Imaging [Internet]. 2011 Apr;38(4):623–32. Available from: http://www.ncbi.nlm.nih.gov/pubmed/21170526

[245] Guerriero F, Ferrari ME, Botta F, Fioroni F, Grassi E, Versari A, et al. Kidney Dosimetry in 177 Lu and 90 Y Peptide Receptor Radionuclide Therapy: Influence of Image Timing, Time-Activity Integration Method, and Risk Factors. Biomed Res Int [Internet]. 2013;2013:1–12. Available from: http://www.hindawi.com/journals/bmri/2013/935351/

[246] Garske-Román U, Sandström M, Fröss Baron K, Lundin L, Hellman P, Welin S, et al. Prospective observational study of 177Lu-DOTA-octreotate therapy in 200 patients with advanced metastasized neuroendocrine tumours (NETs): feasibility and impact of a dosimetry-guided study protocol on outcome and toxicity. Eur J Nucl Med Mol Imaging [Internet]. 2018 Jun 1;45(6):970–88. Available from: http://link.springer.com/10.1007/s00259-018-3945-z

[247] Seregni E, Maccauro M, Chiesa C, Mariani L, Pascali C, Mazzaferro V, et al. Treatment with tandem [90Y]DOTA-TATE and [177Lu] DOTA-TATE of neuroendocrine tumours refractory to conventional therapy. Eur J Nucl Med Mol Imaging. 2014;41(2):223–30.

[248] Baechler S, Hobbs RF, Boubaker A, Buchegger F, He B, Frey EC, et al. Three-

dimensional radiobiological dosimetry of kidneys for treatment planning in peptide receptor radionuclide therapy. Med Phys. 2012;39(10):6118–28.

[249] Hänscheid H, Lapa C, Buck AK, Lassmann M, Werner RA. Dose Mapping After Endoradiotherapy with 177 Lu-DOTATATE/DOTATOC by a Single Measurement After 4 Days. J Nucl Med [Internet]. 2018 Jan;59(1):75–81. Available from: http://jnm.snmjournals.org/lookup/doi/10.2967/jnumed.117.193706

[250] Lassmann M, Chiesa C, Flux G, Bardiès M. EANM Dosimetry Committee guidance document: good practice of clinical dosimetry reporting. Eur J Nucl Med Mol Imaging [Internet]. 2011 Jan 27;38(1):192–200. Available from: http://link.springer.com/10.1007/s00259-010-1549-3

[251] Esser JP, Krenning EP, Teunissen JJM, Kooij PPM, van Gameren ALH, Bakker WH, et al. Comparison of [177Lu-DOTA0,Tyr3]octreotate and [177Lu-DOTA0,Tyr3]octreotide: which peptide is preferable for PRRT? Eur J Nucl Med Mol Imaging [Internet]. 2006 Nov 18;33(11):1346–51. Available from: http://link.springer.com/10.1007/s00259-006-0172-9

[252] Garske U, Sandström M, Johansson S, Sundin A, Granberg D, Eriksson B, et al. Minor changes in effective half-life during fractionated 177 Lu-Octreotate therapy. Acta Oncol (Madr) [Internet]. 2012 Jan 3;51(1):86–96. Available from: http://www.tandfonline.com/doi/full/10.3109/0284186X.2011.618511

[253] Heikkonen J, Mäenpää H, Hippeläinen E, Reijonen V, Tenhunen M. Effect of calculation method on kidney dosimetry in 177 Lu-octreotate treatment. Acta Oncol (Madr) [Internet]. 2016 Oct 2;55(9–10):1069–76. Available from: https://www.tandfonline.com/doi/full/10.1080/0284186X.2016.1182642

[254] Cremonesi M, Ferrari ME, Bodei L, Chiesa C, Sarnelli A, Garibaldi C, et al. Correlation

of dose with toxicity and tumour response to 90Y- and 177Lu-PRRT provides the basis for optimization through individualized treatment planning. Eur J Nucl Med Mol Imaging [Internet]. 2018 Dec 21;45(13):2426–41. Available from: http://link.springer.com/10.1007/s00259-018-4044-x

[255] Grimes J, Celler A. Comparison of internal dose estimates obtained using organ-level, voxel S value, and Monte Carlo techniques. Med Phys [Internet]. 2014 Aug 14;41(9):092501. Available from: http://doi.wiley.com/10.1118/1.4892606

[256] Emami B, Lyman J, Brown A, Cola L, Goitein M, Munzenrider JE, et al. Tolerance of normal tissue to therapeutic irradiation. Int J Radiat Oncol [Internet]. 1991 May;21(1):109–22. Available from: https://linkinghub.elsevier.com/retrieve/pii/036030169190171Y

[257] Svensson J, Berg G, Wängberg B, Larsson M, Forssell-Aronsson E, Bernhardt P. Renal function affects absorbed dose to the kidneys and haematological toxicity during 177Lu-DOTATATE treatment. Eur J Nucl Med Mol Imaging [Internet]. 2015 May 6;42(6):947–55. Available from: http://link.springer.com/10.1007/s00259-015-3001-1

[258] Garske U, Sandström M, Johansson S, Granberg D, Lundqvist H, Lubberink M, et al. Lessons on Tumour Response: Imaging during Therapy with (177)Lu-DOTA-octreotate. A Case Report on a Patient with a Large Volume of Poorly Differentiated Neuroendocrine Carcinoma. Theranostics [Internet]. 2012;2(5):459–71. Available from: http://www.ncbi.nlm.nih.gov/pubmed/22768026

[259] Thakral P, Sen I, Pant V, Gupta SK, Dureja S, Kumari J, et al. Dosimetric analysis of patients with gastro entero pancreatic neuroendocrine tumors (NETs) treated with PRCRT (peptide receptor chemo radionuclide therapy) using Lu-177 DOTATATE and

capecitabine/temozolomide (CAP/TEM). Br J Radiol [Internet]. 2018 Nov;91(1091):20170172. Available from: http://www.ncbi.nlm.nih.gov/pubmed/30028180

[260] Del Prete M, Buteau F-A, Arsenault F, Saighi N, Bouchard L-O, Beaulieu A, et al. Personalized 177Lu-octreotate peptide receptor radionuclide therapy of neuroendocrine tumours: initial results from the P-PRRT trial. Eur J Nucl Med Mol Imaging [Internet]. 2019;46(3):728–42. Available from: http://www.ncbi.nlm.nih.gov/pubmed/30506283

[261] Garin E, Rolland Y, Pracht M, Le Sourd S, Laffont S, Mesbah H, et al. High impact of macroaggregated albumin-based tumour dose on response and overall survival in hepatocellular carcinoma patients treated with 90 Y-loaded glass microsphere radioembolization. Liver Int [Internet]. 2017 Jan;37(1):101–10. Available from: http://doi.wiley.com/10.1111/liv.13220

[262] Sundlöv A, Sjögreen-Gleisner K, Svensson J, Ljungberg M, Olsson T, Bernhardt P, et al. Individualised 177Lu-DOTATATE treatment of neuroendocrine tumours based on kidney dosimetry. Eur J Nucl Med Mol Imaging [Internet]. 2017 Aug 22;44(9):1480–9. Available from: http://www.ncbi.nlm.nih.gov/pubmed/28331954

[263] Bergsma H, Konijnenberg MW, van der Zwan WA, Kam BLR, Teunissen JJM, Kooij PP, et al. Nephrotoxicity after PRRT with 177Lu-DOTA-octreotate. Eur J Nucl Med Mol Imaging [Internet]. 2016 Sep 10;43(10):1802–11. Available from: http://dx.doi.org/10.1007/s00259-016-3382-9

[264] Kabasakal L, AbuQbeitah M, Aygün A, Yeyin N, Ocak M, Demirci E, et al. Pre-therapeutic dosimetry of normal organs and tissues of 177Lu-PSMA-617 prostate-specific membrane antigen (PSMA) inhibitor in patients with castration-resistant prostate cancer.

Eur J Nucl Med Mol Imaging [Internet]. 2015 Dec 31;42(13):1976–83. Available from: http://link.springer.com/10.1007/s00259-015-3125-3

[265] Becker S, Laffont S, Vitry F, Rolland Y, Lecloirec J, Boucher E, et al. Dosimetric evaluation and therapeutic response to internal radiation therapy of hepatocarcinomas using iodine-131-labelled lipiodol. Nucl Med Commun [Internet]. 2008 Sep;29(9):815–25. Available from: https://insights.ovid.com/crossref?an=00006231-200809000-00011

[266] Sandstrom M, Garske-Roman U, Granberg D, Johansson S, Widstrom C, Eriksson B, et al. Individualized Dosimetry of Kidney and Bone Marrow in Patients Undergoing 177Lu-DOTA-Octreotate Treatment. J Nucl Med [Internet]. 2013 Jan 1;54(1):33–41. Available from: http://www.ncbi.nlm.nih.gov/pubmed/23223392

[267] Madsen MT, Menda Y, O'Dorisio TM, O'Dorisio MS. Technical Note: Single time point dose estimate for exponential clearance. Med Phys [Internet]. 2018 May 26;45(5):2318–24. Available from: http://doi.wiley.com/10.1002/mp.12886

[268] Long DT, King MA, Gennert MA. Development of a 3D gradient-based method for volume quantitation in SPECT. IEEE Trans Nucl Sci [Internet]. 1991 Apr;38(2):748–54. Available from: http://ieeexplore.ieee.org/document/289384/

[269] Chuang K-S, Tzeng H-L, Chen S, Wu J, Chen T-J. Fuzzy c-means clustering with spatial information for image segmentation. Comput Med Imaging Graph [Internet]. 2006 Jan;30(1):9–15. Available from: https://linkinghub.elsevier.com/retrieve/pii/S0895611105000923

[270] Gillies RJ, Kinahan PE, Hricak H. Radiomics: Images Are More than Pictures, They Are Data. Radiology [Internet]. 2016 Feb;278(2):563–77. Available from: http://pubs.rsna.org/doi/10.1148/radiol.2015151169